FORCE AND MIXED CONVECTIVE ELECTROKINETIC FLOWS OF NON-NEWTONIAN FLUIDS IN A MICROCHANNEL

Thesis submitted by

Tripti Namdeo Kumbalpuri

Doctor of Philosophy

(Engineering)

DEPARTMENT OF MECHANICAL ENGINEERING

FACULTY COUNCIL OF ENGINEERING & TECHNOLOGY

JADAVPUR UNIVERSITY

KOLKATA, INDIA

2025

INDEX NO.: 003/22/E

REGISTRATION NO: 1022211004

1. **Title of the thesis:**

Force and mixed convective electrokinetic flows of non-Newtonian fluids in a microchannel. .

2. **Name, Designation & Institution of the Supervisors:**

i. Dr. Sandip Sarkar
Professor
Department of Mechanical Engineering
Jadavpur University, Kolkata-700032

3. **List of Publications (Referred Journals)**

i. **Tripti Namdeo Kumbalpuri** and Sandip Sarkar. " Thermally developing streaming potential-mediated pressure-driven flow of Phan–Thien–Tanner fluid in a microchannel." **Physics of Fluids** 36, 072019 (2024).

ii. **Tripti Namdeo Kumbalpuri** and Sandip Sarkar. " Thermally developing combined electroosmotic and pressure-driven flow of Phan–Thien–Tanner fluids in a microchannel." **Physics of Fluids** 35, 082015 (2023).

4. **List of Patents:**

Nil

5. **List of Presentations in National/International Conferences**

i. 10^{th} International and 50^{th} National Conference on Fluid Mechanics and Fluid Power (FMFP), December 20-22, 2023**, IIT Jodhpur**, India

ii. 9^{th} International and 49^{th} National Conference on Fluid Mechanics and Fluid Power (FMFP) December 14-16, 2022, **IIT Roorkee**, India.

STATEMENT OF ORIGINALITY

I, **TRIPTI NAMDEO KUMBALPURI** registered on 27.01.2022, do hereby declare that this thesis entitled "**Force and mixed convective electrokinetic flows of non-Newtonian fluids in a microchannel**" contains literature survey and original research work done by the undersigned candidate as part of Doctoral studies.

All information in this thesis have been obtained and presented in accordance with existing academic rules and ethical conduct. I declare that, as required by these rules and conduct, I have fully cited and referred all materials and results that are not original to this work.

I also declare that I have checked this thesis as per the "Policy on Anti Plagiarism, Jadavpur University , 2019", and the level of similarity as checked by iThenticate software is **5%**.

Signature of Candidate:

(TRIPTI NAMDEO KUMBALPURI)

Date: 27/11/2025

Certified by Supervisor(s):

(Signature with date, seal)

27/11/25

(Dr. Sandip Sarkar)

Dr. Sandip Sarkar
Professor
Department of Mechanical Engineering
Jadavpur University, Kolkata-32

MECHANICAL ENGG. DEPARTMENT
☎2414 6890
KOLKATA-32
JADAVPUR UNIVERSITY

CERTIFICATE FROM THE SUPERVISORS

This is to certify that the thesis entitled "**Force and mixed convective electrokinetic flows of non-Newtonian fluids in a microchannel**" submitted by Ms. Tripti Namdeo Kumbalpuri, who got her name registered on 27.01.2022 for the award of Ph.D. (Engineering) degree of Jadavpur University is absolutely based upon her own work under our supervision and that neither her thesis nor any part of the thesis has been submitted for any degree/diploma or any other academic award anywhere before.

Sandip Sarkar

27/11/2025

(Dr. Sandip Sarkar)

Signature of the Supervisor
and date with Office Seal

Dr. Sandip Sarkar
Professor
Department of Mechanical Engineering
Jadavpur University, Kolkata-32

MECHANICAL ENGG. DEPARTMENT
2414 6890
KOLKATA-32
JADAVPUR UNIVERSITY

ACKNOWLEDGEMENT

"*Somewhere, something incredible is waiting to be known*." – Carl Sagan

As I reach the final steps of my doctoral journey at Jadavpur University, I pause with a heart full of gratitude. This thesis, though bearing my name, stands on the shoulders of the many people whose support, inspiration, and faith in me shaped every step of the way.

My deepest and most sincere gratitude goes to my supervisor, Professor Dr. Sandip Sarkar. His profound insight, patient mentorship, and unwavering belief in my potential made this journey possible. His academic rigor was always matched with personal kindness, allowing me to explore freely while guiding me with gentle firmness. His impact on my work and growth is immeasurable.

I am also deeply grateful to the Directorate of Technical Education (Mumbai), Government College of Engineering, Nagpur, and AICTE for availing me the QIP Scholarship and granting me deputation for the QIP PhD course. Their generous support and trust in my potential have been pivotal in enabling me to pursue this doctoral research at Jadavpur University.

I would also like to express my heartfelt gratitude to Dr. Gautam Majumdar, whose guidance not only shaped my academic outlook but also played a foundational role in this journey. It was through his kind initiative and support that I was introduced to Professor Dr. Sandip Sarkar, a connection that has defined my doctoral path. I remain deeply indebted to him for that invaluable gesture.

I would like to extend my heartfelt thanks to my beloved student Mr. Venkatesh Kolawar Senior Manager, Tata Steel, for his assistance in arranging accommodation and helping me settle into a new environment was invaluable and greatly eased my transition. His kindness and readiness to help made a significant difference, and I remain deeply grateful for his thoughtfulness and support.

I would like to extend my heartfelt appreciation to the Head of the Mechanical Engineering Department, the esteemed Professors, and all the staff of Jadavpur University. For their guidance, and support as and when needed.

I would like to thank the students I had the privilege to teach, whose curiosity and engagement enriched my academic experience during this research journey.

My successful stay at Jadavpur would not have been possible without the support of my lab-mates, especially Joy, Chandrashekhar, and Satya. Joy, your calm presence and sincerity lightened the toughest days. Chandrashekhar, your energy and optimism turned routine lab work into collaborative growth. Satya, your positive attitude and enthusiasm made every challenge easier and every moment enjoyable. I am deeply grateful for your friendship and support.

I wish to warmly acknowledge the support and companionship of Soumendra, Sudipta, Satyajit, Monali, Anukampa, Dinesh, Vikash, Binod, Hasan, Rupam, and Ashish.

A special note of appreciation to Pramanik da, Pintu da, Shyamol da and Shyamali of hydraulic lab for their dependable support and ever-helpful nature.

"*Family is not an important thing. It's everything*." – Michael J. Fox

No words can truly capture my gratitude to my mother, Smt. Kunda Kumbalpuri, and father, Shri N. P. Kumbalpuri, who have been the foundation of my life. Their values, sacrifices, and unconditional love have shaped who I am. To my brother Sachin and sister-in-law Akanksha, thank you for being my constant well of strength and quiet encouragement. Your faith in me was the silent force that carried me through even when I couldn't find the words to ask for help. My sisters Varsha and Shweta, and brother-in-law's Shri. Mohan and Shri. Arvind—your love and faith in me were deeply reassuring. The cheer and love of my niece Srushti and nephews Shlok, Swaransh, Arjun and Prathamesh brought light and balance during the hardest phases.

And to my dearest son Adi —you are my light, my peace, and my purpose. Your innocent smile reminded me, even on the hardest days, why I began this journey. This work is, in so many ways, for you.

To all those whose names I may not have mentioned explicitly but whose influence is woven into the fabric of this work—thank you. This thesis is a testament to your presence in my life.

_____

(Tripti Namdeo Kumbalpuri)

Contents

LIST OF FIGURES

LIST OF TABLES

NOMENCLATURE

H	half height of the confinement
n_k	activity of the kth ionic species
Be	Bejan number
Br	Brinkman number
e	protonic charge
E_X	induced streaming potential field electric field vector
$\vec{E}$	electric field vector
$\overrightarrow{F_B}$	body force per unit volume
g	acceleration due to gravity
k_B	Boltzmann constant
L	length of the microchannel
W	width of the microchannel
m	non-Newtonian behavioural index
n_+	ionic number density
n_o	reference ionic number density
Nu	Nusselt number
Nu_{FD}	fully developed Nusselt number
P	hydrostatic pressure
Pe	thermal Peclet number
S_P	Joule heating parameter
S_F	local entropy generation due to fluid friction
S_H	local entropy generation due to heat transfer
S_T	total entropy generation
T	dimensional temperature
T_W	wall temperature
T_i	liquid inlet temperature
$\vec{u}$	Dimensionless velocity vector
u, v	non-dimensional velocity components in x and y
U_{HS}	Helmholtz-Smoluchowski velocity
X, Y	non-dimensional coordinates

Greek Symbols

λ	dimensionless Debye length
λ_1	coefficients of compositional expansion
θ	dimensionless temperature
θ_m	bulk mean temperature
μ	shear viscosity
σ_e	electrical conductivity
ζ	zeta potential
$\tilde{\varepsilon}\widetilde{W}\iota_{\mathrm{k}}^2$	Wessienberg Number
ρ	density of fluid
ρ_e	net charge density
ε	dielectric constant of the liquid
ε_o	permittivity of the free space
Λ	relative strengths of the pressure driven and electroosmotic flow actuations
κ	thermal diffusivity
Ψ	dimensionless EDL potential
HS	Helmholtz-Smoluchowski
τ_{xx}	Normal Stress
τ_{xy}	Shear Stress
i	Inlet
l	local
ref	reference
net	Net
stern	stren layer
stream	Streaming
T	Total

Abbreviations

c.c.	complex conjugate
EDL	electrical double layer
EOF	electroosmotic force

ABSTRACT

Microfluidics has revolutionized a wide range of applications, from biomedical diagnostics to chemical processing, due to its ability to manipulate and analyze small volumes of fluids with high precision. Among various microscale transport mechanisms, electrokinetic flow is particularly important because strong surface charge and electrostatic effects dominate at small scales. However, many real fluids exhibit non-Newtonian characteristics such as elasticity and shear thinning, which conventional Newtonian models fail to capture. This motivates a detailed study of the coupled electrokinetic, thermal, and rheological effects in confined geometries.

The methodology involves modeling thermally developing, combined electroosmotic and pressure-driven flow, as well as streaming-potential-mediated pressure-driven flow, of Phan–Thien–Tanner (PTT) viscoelastic fluids in a microchannel. The full nonlinear Poisson–Boltzmann equation is solved to represent the electrical double layer accurately, while the simplified PTT (sPTT) model describes viscoelastic behavior, accounting for both elastic and shear-thinning effects. Semi-analytical expressions are derived for the velocity field, and the energy equation is solved with viscous dissipation, Joule heating, and axial conduction to capture thermal development.

The novelty of this work lies in a unified multiphysics framework that integrates nonlinear electrokinetics, viscoelastic rheology, and thermal transport without invoking the Debye–Hückel approximation. The results show that the velocity and temperature fields are strongly influenced by surface charge density, Weissenberg number, and channel aspect ratio. The thermally developing region increases sensitivity to electrokinetic and rheological parameters, thereby altering Nusselt numbers and overall heat transfer. Entropy-generation analysis indicates that electroosmotic flows are dominated by thermal irreversibility, whereas streaming-potential-induced flows show greater frictional losses.

This methodology provides fundamental understanding and predictive capability for designing efficient lab-on-a-chip devices, bioanalytical systems, and microscale thermal-management applications where accurate control of electrokinetic and thermal transport is essential.

Chapter 1. Introduction

Microfluidics enables precise control of fluids at the micrometer scale and supports the development of integrated platforms such as lab-on-a-chip (LOC) and micro total analysis systems (μTAS). These systems provide several advantages over conventional macroscale setups, including lower reagent and sample consumption, faster reaction times, enhanced sensitivity, and the integration of multiple functions onto a single chip. This level of miniaturization allows complex processes such as mixing, separation, reaction, and detection to be carried out efficiently within compact devices.

1.1 Overview of Microfluidics

Among the most significant applications of microfluidics is biomedical diagnostics. LOC platforms automate and miniaturize assays such as nucleic acid amplification, immunodetection, and cell sorting, enabling rapid and low-cost point of care (POC) testing. [1].Organ on a chip (OoC) systems extend microfluidics into tissue engineering by providing physiologically relevant models for studying disease mechanisms, drug responses, and toxicity .[2]

In pharmaceutical research, microfluidic platforms support high throughput drug screening by allowing precise dosing and combinatorial testing in picolitre scale droplets. Droplet based systems can isolate single cells or reagents, minimize cross contamination, and improve reproducibility [3]. These capabilities accelerate lead compound discovery while reducing material costs. Microfluidic analytical tools, such as microchip electrophoresis and digital microfluidics, also provide rapid, high resolution DNA sequencing, protein analysis, and enzymatic assays with minimal sample preparation[4].

Environmental monitoring has benefited greatly from microfluidic systems designed for on-site detection of contaminants in water, air, and soil. Paper based microfluidics, which rely on capillary flow in porous materials, offer ultra low cost, disposable platforms ideal for real time, instrument free testing. [5] In chemical engineering, microreactors exploit high surface-area-to-volume ratios and laminar flow to improve heat and mass transfer.

Despite these advantages, microfluidics still faces challenges in maintaining consistent flow control at small scales. Overall, microfluidics positioned at the intersection of fluid dynamics, materials science, chemistry, and biology continues to advance a wide range

of fields. Progress in fabrication methods, novel materials such as hydrogels and elastomers, 3D printing, and computational modeling is accelerating development. As microfluidics becomes integrated with artificial intelligence, , and personalized medicine, it is expected to play a transformative role in future scientific and healthcare innovations.

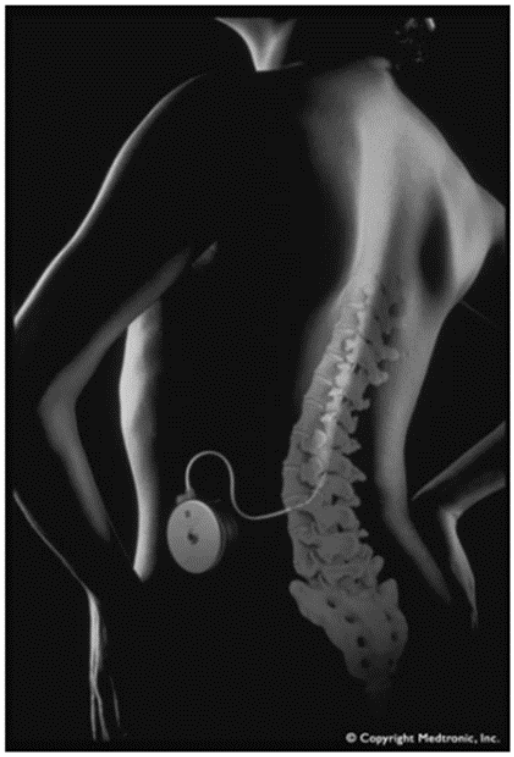

Fig. 1.1. Improve direct injection of cerebrospinal fluid for treating spinal cord.[2]

1.2 Microflow: Scaling Effects

Microfluidics, operating at micrometer to sub-millimeter scales, exhibits behavior that differs significantly from macroscale fluid mechanics. Scaling laws change the balance among inertial, viscous, surface, electrokinetic, and interfacial forces. Miniaturization also affects how electric, thermal, and pressure fields interact with fluid motion. These effects, characterized by nondimensional numbers such as Reynolds, Peclet, Capillary, and Debye, must be considered when designing microfluidic systems.

1.2.1 Viscous Dominance and Reynolds Number Scaling

In microfluidic channels, the Reynolds number ($Re=\rho UL/\mu$)—the ratio of inertial to viscous forces is typically less than unity due to small characteristic lengths ($L\sim10^{-6}–10^{-3}$ m) and modest velocities ($U\sim10^{-4}–10^{-2}$m/s). Consequently, microflows

are almost exclusively laminar and stable, exhibiting highly deterministic streamlines. This contrasts with the turbulence-dominated regimes found in macrofluidics.

1.2.2 Surface Forces and Capillarity

At microscale dimensions, the surface-to-volume ratio increases dramatically (A/V∼1/L), amplifying the influence of surface forces such as surface tension and wettability. Capillary pressure, given by ($\Delta P=2\gamma\cos\theta/R$), becomes a dominant driving mechanism, enabling passive flow in microchannels and paper-based devices. This scaling is exploited in open-channel capillary pumps and droplet-based microfluidics.

1.2.3 Fluid Dynamics and Flow Regimes

In microfluidic systems, the Reynolds number (Re) is typically much less than 1, meaning that the flow is laminar. Laminar flow is characterized by smooth, non-turbulent movement of fluid, where each fluid layer moves parallel to adjacent layers. This is distinct from conventional fluid systems where turbulent flow can occur, particularly at higher Reynolds numbers.

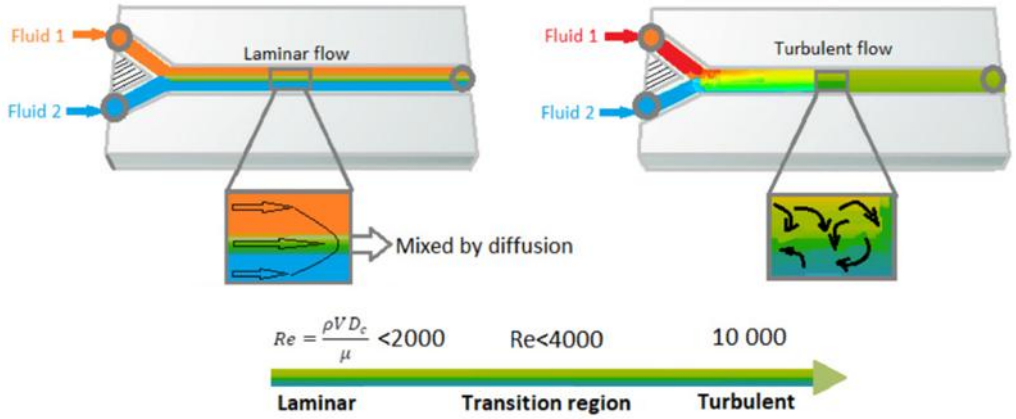

Fig. 1.2. Flow Regimes in Microfluidics [6]

Fig. 1.2 highlights the transition between laminar and turbulent flow regimes, with microfluidic devices operating in the laminar zone. It. would typically show how Reynolds number changes with channel size and flow velocity, illustrating the difference between microfluidic and conventional systems.[7]

1.3 Physical Transport Phenomena in Microfluidic Systems

1.3.1 Microfluidic Dominant Forces

Microfluidic systems operate at scales where surface forces such as surface tension and electrokinetic effects dominate. When the channel size decreases, these forces become

stronger than inertial effects. As a result, phenomena like capillary action and electrophoresis appear clearly. These mechanisms enable precise flow control without mechanical pumps. A Fig. 1.3 would illustrate how capillary forces move fluids in microchannels and how electroosmotic flow (EOF) drives fluid motion under an applied electric field.

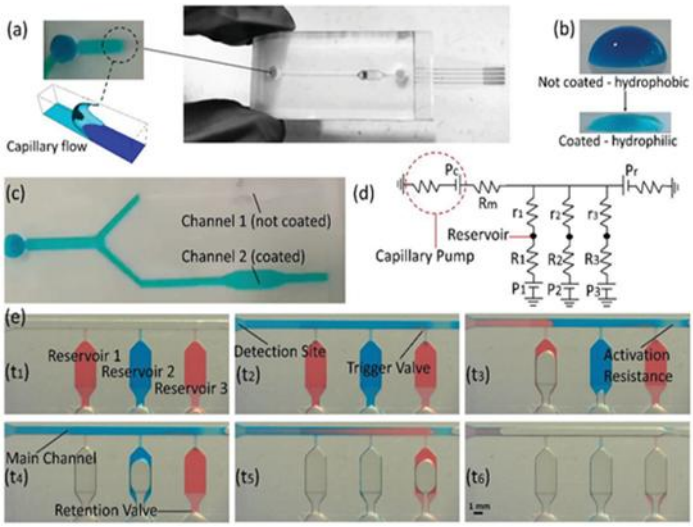

Fig. 1.3. Capillary and Electrokinetic Forces in Microfluidics [8]

1.3.2 Electrokinetics in Microfluidics

Electrokinetic transport in microfluidics occurs due to the interaction between an applied electric field and the electrical double layer (EDL) at solid–liquid interfaces. Electroosmotic flow (EOF) is the most common form of this transport. It is generated by the motion of counterions in the EDL, which drives the bulk fluid at low Reynolds numbers. The flow velocity depends on the zeta potential and the applied electric field. It is commonly described using the Smoluchowski equation. Many microfluidic systems, however, need advanced models that account for surface charge variation, nonlinear electrostatics, and coupled ion transport. Electrokinetic phenomena also include electrophoresis and electrothermal flows. These effects enable precise and valve-less flow control in lab-on-a-chip devices.[9], [10]

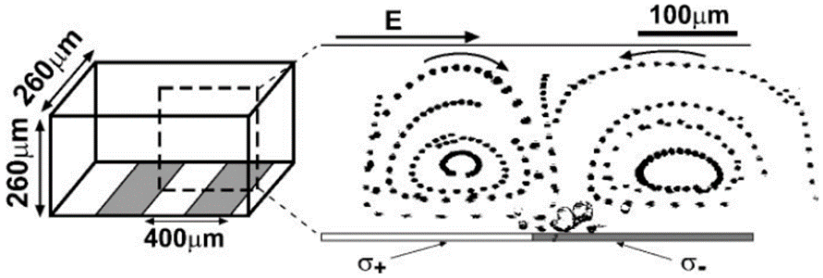

Fig. 1.4. Electroosmotic flow in a microchannel under an applied electric field.[11]

1.3.3 Heat Transfer, and Control

Heat transfer in microchannels is central to thermal management in lab-on-a-chip devices, microreactors, and electronic cooling systems. The high surface-to-volume ratio improves heat exchange. It also increases viscous dissipation, axial conduction, and rarefaction effects.[12], [13] Thermal behaviour can be controlled through several factors. These include channel geometry, surface characteristics, fluid type, and thermal boundary conditions. Active mechanisms such as electroosmotic forces, Joule heating, thermocapillarity, and external fields also influence heat transport. [14], [15]Accurate modeling of these combined effects is essential for designing efficient and adaptive microthermal systems.[16], [17]

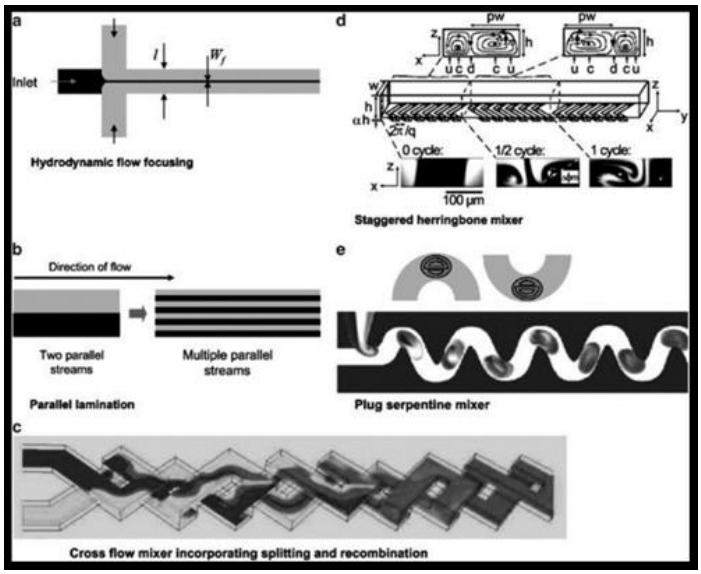

Fig. 1.5. Mixing Strategies in Microfluidics[7]

1.3.4 Mixing in Microfluidics

In microfluidics, mixing is typically diffusive, occurring at much slower rates compared to conventional fluid systems. However, due to the small scale, diffusion can be enhanced by chaotic advection or electrokinetic instabilities that stir fluids within the confined spaces of microchannels. Fig. (1.5) show how serpentine or zigzag channels can induce chaotic mixing through secondary flow and how such patterns break up fluid layers to enhance mixing.

1.3.5 Microflow Modeling: Scope and Challenges

Modeling fluid flow in microfluidic systems presents unique theoretical and computational challenges. These difficulties arise because many physical effects become dominant at small length scales. Unlike macroscale flows, where inertia and turbulence

play major roles, microflows usually operate at very low Reynolds numbers (Re ≪ 1).[18] The flow is steady and laminar, but it is highly sensitive to boundary conditions and interfacial effects. Surface-related forces also play a major role.

Electroosmotic flow (EOF) is one key example. It results from the interaction between an applied electric field and the electric double layer (EDL) near charged surfaces. The classical Helmholtz–Smoluchowski theory works when the EDL is thin and the fluid is Newtonian.[10] When the Debye length becomes comparable to the channel size, this simplification fails, and the Poisson–Boltzmann equation must be solved together with the Navier–Stokes equations.

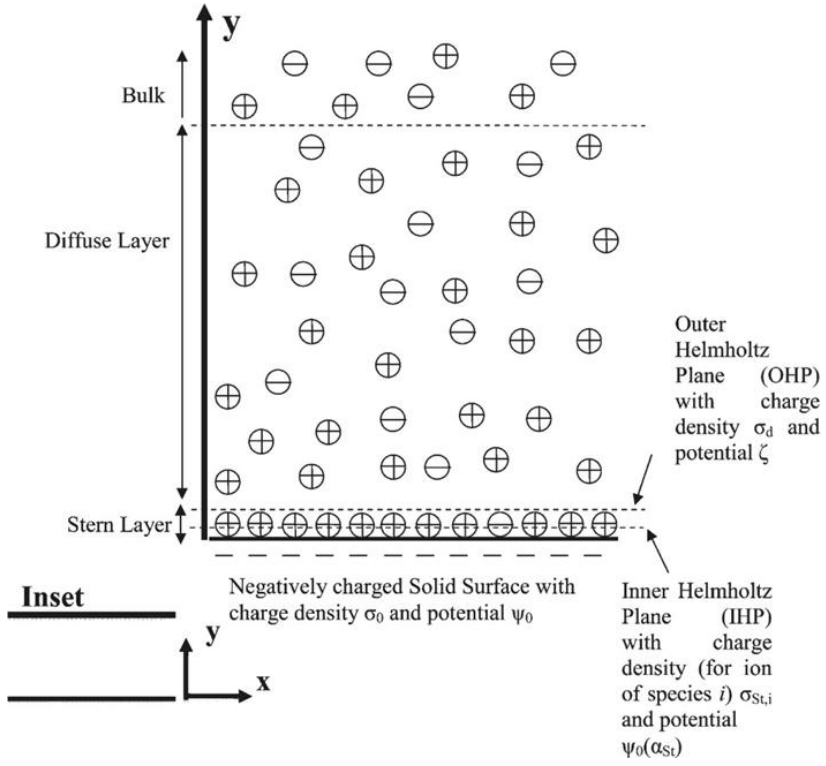

Fig. 1.6. The Gouy-Chapman-Grahame model near a charged surface is shown, with the flow geometry and coordinate axes provided in the inset [19]

Rheology adds another layer of complexity. Many biological and polymeric fluids behave as non-Newtonian materials. They may exhibit shear-thinning, viscoelasticity, or time-dependent viscosity. Generalized Newtonian models such as the power-law and Carreau–Yasuda models help capture shear-dependent viscosity[20] To represent elasticity and memory effects, viscoelastic models like Oldroyd-B, Giesekus, and Phan-Thien–Tanner (PTT) are used.[4]

Microfluidic devices often use combined pressure-driven and electroosmotic forcing. This coupling leads to nonlinear interactions between hydrodynamics, electric fields, and

ion transport[21] Streaming potential effects can also appear, creating a counter electric field that feeds back into the flow and alters charge distribution and flow rate.

These interactions become more complex for viscoelastic fluids, especially under thermally developing conditions.[22], [23] Many devices display incomplete thermal development because of localized heating, short channel lengths, or strong temperature gradients. Temperature affects viscosity, electrostatics, and flow patterns. Viscous dissipation and Joule heating further intensify these effects.

The combined thermal, hydrodynamic, and electrokinetic interactions remain challenging to model, particularly under realistic no-slip boundaries and when EDL potentials cannot be linearized.[24], [25]

1.4 Electrokinetic Phenomena

1.4.1 Formation and role of the Electrical double layer (EDL)

A fundamental aspect of microchannel transport is the electrostatic interaction between dissolved ions and charged channel walls. When a solid surface contacts an aqueous electrolyte, it usually acquires a net surface charge through ionizable surface group dissociation or preferential ion adsorption. The surrounding ionic solution then rearranges to maintain electroneutrality, forming the electrical double layer (EDL). The EDL consists of two regions. The first is the Stern layer, an immobile zone adjacent to the wall that contains tightly bound counterions. The second is the Gouy–Chapman diffuse layer, where counterions and co-ions are thermally distributed and extend into the bulk fluid. Together, these layers screen the wall charge and confine its electrostatic influence.

When the EDL is thin relative to the channel size (the thin-EDL limit), the ion distribution in the diffuse layer can be described by the nonlinear Poisson–Boltzmann equation. The resulting electric potential field is governed by two key parameters: the Debye length and the zeta potential

The Debye length, typically 1–100 nm depending on ionic strength, represents the characteristic EDL thickness and decreases with increasing ion concentration. The zeta potential, defined at the hydrodynamic slip plane, provides a practical measure of surface potential and plays a central role in electrokinetic transport.[26], [27]

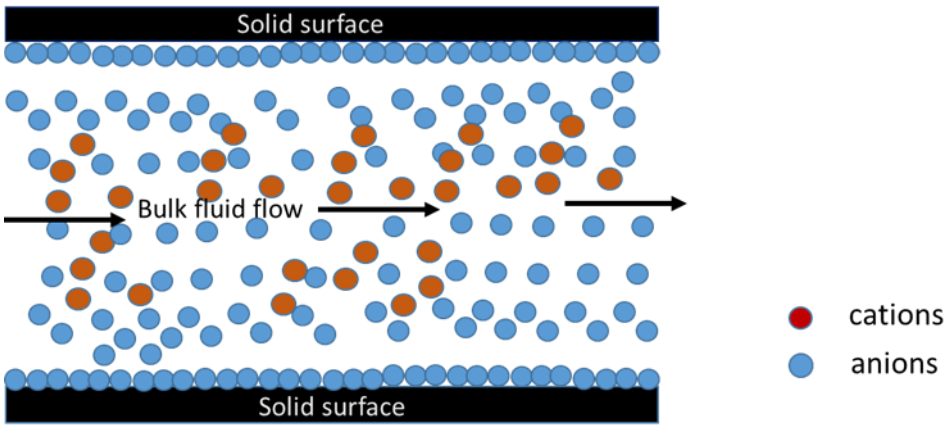

Fig. 1.1.7. A schematic of electrokinetic fluidic transport in a confinement

1.4.2 Types of Electrokinetic flow

Electrokinetic flows refer to transport phenomena that arise when electric fields act on electrolyte solutions. These flows originate from the interaction between an externally applied electric field and the net charge within the electrical double layer (EDL) formed at solid–liquid interfaces. Electrokinetic effects are especially important in microscale systems, where the surface-area-to-volume ratio is high and surface and viscous forces dominate over inertia. The primary types of electrokinetic flows include electroosmotic flow (EOF), electrophoresis, streaming potential, and sedimentation potential. Each mechanism is governed by different physical principles—from charge motion inside the EDL (as in EOF), to the motion of charged particles, to polarization in non-uniform electric fields and thermally induced conductivity gradients. Understanding these effects is essential for designing microfluidic devices used in pumping, sample manipulation, separation, and mixing

Electroosmosis occurs when an applied electric field drives counterions inside the EDL along the solid–liquid interface. These ions drag the surrounding solvent, producing a net fluid motion. When the EDL is much thinner than the channel dimension, the resulting flow is nearly plug-like. If the EDL thickness is comparable to the channel size, the velocity becomes non-uniform and follows the local potential distribution inside the EDL. The electroosmotic flow rate scales with the applied electric field and the zeta potential, which represents the potential at the slip plane.

Electrophoresis describes the motion of charged particles suspended in a fluid under an applied electric field. The particle velocity results from the balance between the electrostatic force and viscous drag. The electrophoretic mobility—velocity per unit

electric field—depends on the particle size, shape, medium viscosity, and surface charge. The EDL surrounding the particle modifies the effective charge and influences the electrophoretic response.

Streaming potential arises when pressure-driven flow displaces ions in the EDL, generating a streaming current along the flow direction. Ion displacement creates an opposing electric field, which induces a conduction current that balances the streaming current at steady state. This process produces a potential difference between the inlet and outlet of the channel. The resulting electric field drives an electroosmotic flow that opposes the pressure-driven flow, reducing the net flow rate and increasing the apparent hydraulic resistance.

Sedimentation potential is the voltage generated when charged colloidal particles settle or rise due to gravity or centrifugal forces. As the particles move, they disturb the surrounding charge distribution, producing a potential difference across the fluid. Although sedimentation potential is relevant in larger-scale colloidal systems, it is generally weak in microfluidics because electrostatic and viscous forces dominate over inertial forces at small scales. [18], [28]

1.4.3 Electrokinetic Potential Distribution in Electrokinetic Transport

Full and Linearized Models

Electrokinetic transport mechanisms, such as electroosmotic flow (EOF), streaming potential, and electroviscous effects, fundamentally originate from the interaction between electric fields and net ionic charge distributions in the Electric Double Layer (EDL). Electrokinetic potential distribution in an electrolyte near a charged surface plays a foundational role in predicting electroosmotic flow (EOF), streaming potential, and related microfluidic phenomena. The development of this theory involves coupling electrostatics with ionic charge distribution under thermal equilibrium. The fundamental starting point is Poisson's equation, which relates electric potential to local charge density.

i. Poisson Equation

The electrostatic potential $\psi(r)$ in a dielectric medium is governed by:

$\nabla^2\psi = -\rho_e / \varepsilon$, where $\nabla^2\psi$: Laplacian of the electric potential ρ_e: Net local charge density (C/m^3), ε: Permittivity of the fluid medium (F/m), ψ: Electrostatic potential (V).This

equation states that the curvature of the potential field arises due to the spatial distribution of charge density.

ii. Charge Density from Boltzmann Distribution (Ionic Equilibrium)

For a dilute, symmetric z:z electrolyte (e.g., NaCl or KCl), under thermal equilibrium (no external current), the number density of cations and anions follows the Boltzmann distribution:$n_+(y) = n_0 \exp(-ze\psi(y) / kBT)$ and $n_-(y) = n_0 \exp(+ze\psi(y) / kBT)$where: n_0: Bulk ion concentration (mol/m³), z: Valence of ions (e.g., z = 1 for Na^+), e: Elementary charge (1.602×10^{-19} C), kB: Boltzmann constant, T: Absolute temperature (K)- $\psi(y)$: Electric potential at distance y from the charged surface. Hence, the net charge density becomes: $\rho_e(y) = ze[n_+(y) - n_-(y)] = -2zen_0 \sinh (ze\psi / kBT)$.

iii. Full Poisson–Boltzmann (PB) Equation

Substituting the above $\rho_e(y)$ into the Poisson equation yields: $d^2\psi / dy^2 = (2zen_0 / \varepsilon) \sinh(ze\psi / kBT)$. This is the nonlinear Poisson–Boltzmann equation, describing the variation of potential within the electric double layer (EDL). For general cases with moderate to high potentials (e.g., $\zeta > 25$ mV), this equation must be solved numerically.

Limitations of the Debye–Hückel Approximation in Electrokinetic Transport

The Debye–Hückel (DH) approximation simplifies the nonlinear Poisson–Boltzmann equation by assuming a small electrostatic potential, i.e.$|ze\psi / kBT| << 1$. While useful for analytical solutions, it has several key limitations:

Low Surface Potential Requirement: Valid only for zeta potentials $\zeta < 25$ mV. At higher potentials (common in microfluidics), it underestimates charge density and flow velocity.

Neglects Ion Size and Correlations: Assumes point ions and dilute solutions. Inaccurate for multivalent ions or high ionic strength due to steric and electrostatic correlations.

Fails for Overlapping EDLs: In microchannels, overlapping electric double layers (EDLs) lead to strong interactions that the linear model cannot capture.

Ignores Surface Charge Regulation: Assumes constant surface potential, neglecting effects of pH, ionic strength, and dynamic surface reactions.

Neglects Thermal and Electrochemical Effects: Assumes isothermal equilibrium, ignoring Joule heating, temperature-dependent properties, and Faradaic reactions.[10]

1.4.4 Thermal Effects in Electroviscoelastic Microflows

Thermal behavior in electrokinetic microflows is a key factor in designing efficient microfluidic systems. When electric fields are applied to electrolytes in confined geometries, Joule heating becomes significant due to resistive dissipation, especially in high-field or high-conductivity scenarios. In microchannels, limited cross-sectional area restricts heat dissipation, leading to the development of strong axial and transverse temperature gradients [29], [30], [31].These gradients influence fluid properties such as viscosity, permittivity, and conductivity affecting both the electroosmotic flow (EOF) and the pressure-driven components of transport. As a result, the flow becomes thermally developing, especially near the channel entrance, where the thermal boundary layer thickens progressively downstream [32], [33]. This development alters the axial temperature profile and, in turn, modifies the velocity field due to the strong coupling between the thermal and electrokinetic phenomena[34], [35]. The inclusion of viscoelastic fluids further complicates thermal transport. Viscoelastic stresses resist flow deformation, which alters the convective component of heat transfer and leads to delayed thermal development or broader thermal boundary layers. These effects are particularly important in systems designed for precise temperature control or thermal management, such as lab-on-a-chip diagnostics or electrokinetic pumping. Additionally, in such viscoelastic electrokinetic systems, surface characteristics like zeta potential or wall charge density can significantly impact thermal performance by altering the electrokinetic flow behavior thereby modulating advective heat transfer near the walls.[36], [37] Therefore, a comprehensive understanding of thermo-electro-viscoelastic coupling is essential for accurately predicting the flow and thermal profiles in confined microfluidic geometries, especially under high-field conditions where Joule heating dominates.[14], [38]

Limitations of Newtonian Fluid Models in Electrokinetic Flow

Electrokinetically actuated microfluidic systems play a vital role in lab-on-a-chip platforms, biomedical diagnostics, and microscale energy conversion. However, the traditional assumption of Newtonian behavior, where viscosity is constant and independent of shear rate often breaks down in realistic applications involving polymeric

or biological fluids. The limitations of such assumptions have been critically examined below,

i. Shear-Dependent Viscosity

In microchannels, polymeric fluids often display shear-thinning or shear-thickening behavior under strong electric fields and confined geometries. Newtonian models fail to capture these variations, leading to significant errors in flow rate and solute dispersion predictions.

ii. Viscoelastic and Normal Stress Effects

Viscoelastic fluids exhibit both viscous and elastic characteristics, producing normal stress differences, memory effects, and flow instabilities. Newtonian models cannot account for such effects, which are crucial for understanding complex behaviors like asymmetric velocity profiles and micro-mixing efficiency.

iii. Joule Heating and Viscosity Modulation

Strong electric fields can induce Joule heating, which alters the local temperature and reduces viscosity. This affects flow velocity and electroosmotic mobility—nonlinear effects that Newtonian models with constant viscosity fail to capture.

iv. Interfacial Slip at Microscale Boundaries

At microscale dimensions, slip at hydrophobic or electrostatically active surfaces becomes non-negligible. The classical no-slip boundary condition used in Newtonian frameworks can lead to incorrect flow field predictions if interfacial slip is ignored[39].

v. Energy Conversion Limitations

Electrokinetic energy conversion is often overestimated by Newtonian models, which ignore the impact of shear-thinning, viscoelastic stresses, and wall slip. A more accurate prediction requires non-Newtonian constitutive models that incorporate these complexities.[32], [40] The limitations of Newtonian assumptions such as neglecting shear-thinning behavior, viscoelastic stresses, Joule heating effects, and interfacial slip can lead to significant inaccuracies in predicting flow characteristics and device performance. Hence, incorporating non-Newtonian fluid models and electrothermal coupling is essential for capturing the true physics of electrokinetically driven microfluidic systems.[41], [42], [43]

1.5 Introduction to Viscoelastic Fluids

Viscoelastic fluids are materials that simultaneously exhibit the irreversible flow behavior characteristic of viscous fluids and the recoverable deformation behavior typical of elastic solids. Examples include polymer solutions, molten plastics, surfactant solutions, gels, and many biological fluids such as mucus or cytosol. The central challenge in modeling viscoelastic fluids lies in capturing their time-dependent response to deformation, which is briefly in preceding section.

1.5.1 Rheological Behavior of Viscoelastic Fluids

Viscoelastic fluids exhibit a complex interplay between viscous dissipation and elastic energy storage, arising from the deformation and relaxation of embedded microstructures such as long-chain polymers. This leads to a suite of nonlinear behaviors that are central to the accurate modeling of complex flow phenomena—particularly in microscale electrokinetic systems. The key rheological features are outlined below:

i. Stress Relaxation and Creep

Under constant strain, viscoelastic fluids exhibit stress relaxation, where the internal stress decays over time due to molecular relaxation mechanisms. Conversely, under constant stress, they show creep, characterized by time-dependent strain growth. This behavior is modeled using the relaxation modulus G(t) and creep compliance J(t). Stress Relaxation Equation

$\sigma(t) = G(t) \cdot \gamma_0$ where, $\sigma(t)$ is the time-dependent stress and γ_0 is the imposed constant strain. The characteristic time scale of this decay is the relaxation time λ, a fundamental quantity in linear and nonlinear viscoelastic models [44].

ii. Shear Thinning

Viscoelastic fluids often exhibit shear thinning, wherein the apparent viscosity ηapp decreases with increasing shear rate $\dot{\gamma}$. This is caused by flow-induced polymer alignment and disentanglement, which reduce resistance to flow. Apparent Viscosity app = $\tau xy / \dot{\gamma}$ where τxy is the shear stress and $\dot{\gamma}$ is the shear rate. Nonlinear constitutive models such as the Phan-Thien–Tanner (PTT) and Giesekus models incorporate this behavior inherently.[4], [45]

iii. Normal Stress Differences

Under shear, viscoelastic fluids generate normal stress differences—a signature of elastic tension along flow streamlines. The first normal stress difference, $N1$, is defined as : $N_1 = \tau xx - \tau yy$. This stress differential leads to phenomena like rod climbing (Weissenberg effect) and secondary flow in curved geometries. For Newtonian fluids, $N1 = 0$. The second normal stress difference, $N2 = \tau yy - \tau z$, though smaller, becomes relevant in elongational and extensional flows .[20], [46]

iv. Elastic Recoil and Flow Instabilities

Upon cessation of an imposed deformation, viscoelastic fluids may exhibit elastic recoil, due to the rapid release of stored elastic energy. More importantly, even at low Reynolds number, these fluids can undergo purely elastic instabilities—instabilities triggered by elastic rather than inertial effects. These are characterized by: Critical onset at moderate Weissenberg number: $Wi = \lambda.\dot{\gamma}$. Time-periodic or chaotic velocity fluctuations, Flow asymmetry and secondary vortex formation in otherwise symmetric geometries. These phenomena are prevalent in microfluidic electrokinetic flows, where high electric fields cause sharp shear rates and stress gradients near walls and channel corners [15], [47], [48].

Therefore, such nonlinear rheological behavior of viscoelastic fluids—including stress relaxation, shear thinning, normal stress differences, and elastic instabilities—demands advanced constitutive modeling for accurately predicting electrokinetic flows in microfluidic environments.

1.5.2 Constitutive Modeling of Viscoelastic Fluids for Electrokinetic Transport in Microchannels

Evolution of Viscoelastic Constitutive Models: Foundations and Principles

The development of viscoelastic constitutive models arose from the need to reconcile empirical rheological behaviour with the principles of continuum mechanics and thermodynamics. Three foundational criteria have guided this progression:

i. Objectivity (Frame Invariance)

Constitutive equations must remain valid under arbitrary rigid-body motions—ensuring that predictions are independent of the observer's frame. To this end, objective time derivatives like the upper-convected derivative were introduced[44]: $\mathcal{D}A/\mathcal{D}t = \partial A/\partial t +$

v·∇A− (∇v)^T·A− A·∇vSuch derivatives are essential in models like Oldroyd-B and Giesekus, maintaining the mathematical integrity of stress evolution [20]

ii. Thermodynamic Consistency

To comply with the second law of thermodynamics, constitutive models must guarantee non-negative entropy production, often enforced via:$\nabla \mathbf{v} \geq 0$. Models like Phan-Thien–Tanner (PTT) and Giesekus incorporate nonlinear damping terms and anisotropic drag, respectively, ensuring that energy dissipation is correctly captured. [4], [49]

iii. Material Realism

Viscoelastic fluids exhibit shear thinning, normal stress effects, stress relaxation, and recoil phenomena not captured by Newtonian or linear viscoelastic models. Constitutive frameworks such as PTT, Giesekus, and FENE-P were developed to replicate these features. The PTT model, in particular, effectively predicts strong nonlinearity under high strain typical of microfluidic electrokinetic flows .[50]

These models form the foundation for modern computational and experimental studies in confined viscoelastic flows, where elasticity-driven instabilities and complex rheology dominate system dynamics.

Constitutive Frameworks for Viscoelastic Fluids in Microfluidics

Viscoelastic fluids are typically modeled using differential constitutive equations that relate stress evolution to deformation history via objective derivatives. Below is an overview of the most commonly used models, with emphasis on their applicability to microfluidic and electrokinetic flows.

i. Oldroyd-B Model

Oldroyd[44] proposed this model to describe dilute polymer solutions by combining solvent and polymeric contributions with the upper-convected derivative: $\tau + \lambda_1 \hat{D}\tau = \mu(\dot{\gamma} + \lambda_2 \hat{D}\dot{\gamma})$, where τ: extra stress tensor, $\dot{\gamma}$: rate-of-strain tensor,, λ_1, λ_2: relaxation and retardation times. μ: viscosity, $\hat{D}$: upper-convected derivative and Upper-convected derivative: $\hat{D}\tau = \partial\tau/\partial t + v\nabla\tau - (\nabla v)^T \tau - \tau \nabla v$

Although analytically tractable and widely used in theoretical studies[20], the Oldroyd-B model fails to capture shear thinning and predicts unbounded extensional viscosity under elongational flow—limitations critical in confined microchannel applications.

In microfluidics, it has been applied for basic studies of electroosmotic instabilities [51], [52] and benchmark validation in low-De regimes. However, its oversimplified rheology limits use under strong electric fields and high strain-rate gradients near walls.

ii. Giesekus Model

To account for shear-thinning behavior, Giesekus (1982)[49] introduced a model incorporating anisotropic molecular drag, resulting in $\tau + \lambda \hat{D}\tau = \mu [\dot{\gamma} + \alpha \lambda \tau \cdot \dot{\gamma}]$, where α is dimensionless mobility parameter ($0 \leq \alpha \leq 1$). This model captures both first and second normal stress differences and strain-rate-dependent viscosity, making it more representative of real polymer solutions[20]. In microfluidics, it has shown excellent performance in simulating cross-slot viscoelastic flows, pressure-driven channel flows, and electrokinetic instabilities. Its ability to model nonlinearities makes it suitable for electroosmotic flows with surface charge modulation or complex geometries[49].

iii. FENE-P Model

The FENE-P (Finite Extensibility Nonlinear Elastic Peterlin) model accounts for the limited extensibility of polymer chains. The constitutive relation is: $\tau + \lambda \hat{D}\tau = (\mu / \xi) \dot{\gamma}$, where $\xi = 1 - tr(\tau) / (b \mu)$ b: finite extensibility parameter tr(τ): trace of the stress tensor. The nonlinear spring force prevents unphysical divergence in extensional viscosity. It provides a good description of extensional flows, such as those in cross-slot devices or T-junctions in microfluidics[53]. In electrokinetic flows, the FENE-P model has been used to study instability thresholds and polymer stretching near but is less robust under highly shear-thinning or concentrated solution regimes.

iv. Phan-Thien–Tanner (PTT) Model

The PTT model, introduced by Thien and Tanner[4], is designed for concentrated polymer solutions.. It incorporates a damping function f(tr(τ)) to capture nonlinear rheology: $f(tr(\tau))\ \tau + \lambda \hat{D}\tau = \mu \dot{\gamma}$ with: Linear damping: $f(tr(\tau))=1+\varepsilon\lambda tr(\tau)$ Exponential damping: $f(tr(\tau))=\exp(\varepsilon\lambda tr(\tau))$ where, ε: nonlinear damping parameter The upper-convected derivative $\hat{D}\tau$ remains as in the Oldroyd-B model. Phan-Thien–Tanner (PTT) Models predicts finite extensional viscosity, unlike Oldroyd-B, captures shear thinning, normal stress differences, stress relaxation. They are thermodynamically consistent, numerically stable and more accurate under complex boundary conditions such as high electric fields, or thermal gradients. [54]

In electrokinetic microfluidics, the PTT model is especially effective due to its balance of nonlinearity and computational tractability. It has been applied in studies of electrothermal viscoelastic flows[15] and streaming potential-based devices. Its ability to adapt to wall-slip and high viscoelasticty makes it well-suited for real-world applications in lab-on-chip systems, micromixers, and biosensors.

1.5.3 Relevance of the sPTT Model in Electrokinetic Flows

Electroosmotic flows (EOF) of viscoelastic fluids exhibit complex behavior even at low Reynolds numbers, including elastic instabilities, asymmetric streamlines, and enhanced mixing—features absent in Newtonian systems [46], [55]. These arise from strong normal stress gradients near the electric double layer (EDL), especially when the EDL is thin relative to the channel height and electric fields are strong. Under such conditions, elastic stresses localize near surfaces and destabilize the flow, leading to symmetry breaking and oscillations. Linear models like Oldroyd-B[20], [44] fail to capture these effects, necessitating models that include finite extensibility and shear-thinning.

To overcome these limitations, more advanced constitutive models are required—particularly those that incorporate nonlinear elastic behavior and rate-dependent viscosity. In this regard, the Simplified Phan-Thien–Tanner (sPTT) model is particularly suitable. .The sPTT model, introduced by Phan-Thien and Tanner[4] (1977) and extended by many authors [50], is particularly well-suited for viscoelastic electrokinetic flows for the following reasons:

i. Finite Extensional Viscosity and Shear Thinning

Unlike the Oldroyd-B model, which assumes infinitely extensible dumbbells and diverges under strong elongational flow, the sPTT model incorporates a nonlinear damping function to regularize stress growth. The constitutive equation is given as: $f(tr(\tau))\cdot\tau + \lambda\cdot(\partial\tau/\partial t + u\cdot\nabla\tau - \tau\cdot\nabla u - (\nabla u)^T\cdot\tau) = 2\mu\cdot D$ where, τ is the extra stress tensor, λ is the relaxation time and μ is the viscosity, $D = (1/2)\cdot(\nabla u + (\nabla u)^T)$ is the rate-of-strain tensor, $f(tr(\tau))$ is the damping function, and u is the velocity vector. The upper-convected derivative of τ is: $\partial\tau/\partial t + u\cdot\nabla\tau - \tau\cdot\nabla u - (\nabla u)^T\cdot\tau$ The stress tensor function $f(tr(\tau))$ takes one of the following forms: Linear form: $f(tr(\tau)) = 1 + \varepsilon\cdot\lambda\cdot tr(\tau)$, Exponential form: $f(tr(\tau)) = \exp(\varepsilon\cdot\lambda\cdot tr(\tau))$. Here, ε is the extensibility parameter, and $tr(\tau)$ is the trace of the stress tensor.[4], [48]

These nonlinear corrections enable the sPTT model to correctly capture shear-thinning behavior observed in EDL-driven flows and provide bounded extensional viscosities under strong field-driven stretching[4].

ii. Captures Wall-localized Stress Gradients and Electrokinetic Effects

In electrokinetic flows, sharp shear layers develop within or near the EDL, particularly at high zeta potentials or large electric fields. These gradients trigger the development of elastic normal stresses that feed back into the velocity field. Sarkar et al. [55] used the sPTT model to simulate such phenomena in electrothermal flows and showed that the model robustly captured both shear-thinning and elastic recoil effects with high spatial resolution.

iii. Numerical Stability and Physical Realism

Compared to other nonlinear models like Giesekus or FENE-P, the sPTT model offers superior numerical stability and is thermodynamically consistent. FENE-P, although also finite extensible, tends to become unstable at high Wi due to its closure approximations. The sPTT, on the other hand, smoothly interpolates between linear viscoelastic behavior at low stresses and bounded nonlinear stress at high deformations [53].

iv. Compatibility with Electrokinetic Governing Systems

The sPTT model integrates seamlessly into the coupled Poisson–Nernst–Planck–Stokes (PNPS) framework used for modeling electrokinetic transport. Its stress-based formulation simplifies coupling with the electric body force term in the momentum equation: $\rho_e E = -(\nabla\varphi) \cdot (\sum z_i \cdot c_i)$ where ρ_e is the net charge density, E is the electric field, φ is the electric potential, and z_i, c_i are the valence and concentration of ionic species [55].The sPTT model, owing to its computational simplicity and ability to capture shear-thinning and elastic effects, serves as a powerful tool in understanding electrokinetic transport of viscoelastic fluids.

Many studies exemplify its potential in predicting complex flow, which are critical in designing efficient electrokinetically-driven microfluidic systems.

1.6 Dimensionless Parameters and Their Physical Significance

Table 1.1. Dimensionless Parameters and Their Physical Significance.

Parameter	**Definition**	**Physical Significance**
λ_D (Dimensionless Debye length)	$\lambda_D = \kappa^{-1} / H$	Thickness of EDL relative to channel height.
Ψ (Dimensionless potential)	$\overline{\Psi} = ze\psi / (k_B T)$	Scaling of electrostatic potential inside the EDL.
Λ (Pressure–EOF interaction)	$\Lambda = (dp/dx) / [\varepsilon \zeta E_0 / H^2]$	Interplay between pressure-driven and electroosmotic flow.
E* (Dimensionless streaming field)	$E^* = E_{stream} / E_0$	Magnitude of induced streaming potential relative to applied field.
Wi (Weissenberg number)	$Wi = \lambda U / H$	Represents fluid elasticity relative to viscous effects.
Pe (Péclet number)	$Pe = U H / \alpha$	Measures the relative strength of advective to diffusive heat transport.
Be (Bejan number)	$Be = S_T / (S_T + S_f)$	Indicates dominance of thermal vs. frictional irreversibility.
θ (Dimensionless temperature)	θ=Tw−Ti/T−Ti	Normalized thermal field representing heating due to Joule and viscous effects.
Br (Brinkman number)	$Br = \mu U^2 / [k (Tw - Ti)]$	Quantifies viscous dissipation relative to imposed thermal gradient.
β (Electrokinetic coupling)	$\beta = \varepsilon \zeta E_0 / (\mu U)$	Strength of electroosmotic forcing relative to viscous resistance.
Nu (Nusselt number)	$Nu = h H / k$	Measures convective heat transfer relative to conduction.
Nu (Dimensionless temperature/Nusselt distribution)	Depends on θ, $\partial\theta/\partial y$ at wall	Represents spatial evolution of thermal boundary layer and local heat-transfer rate.

1.7 Specific Objectives of the Present Study

The present study aims to:

(i) Develop a semi-analytical model for thermally developing viscoelastic flow in microchannel using the sPTT constitutive equation under combined pressure, electroosmotic, and self-induced streaming potential effects.

(ii) Solve the coupled Poisson–Boltzmann, momentum, and energy equations to capture nonlinear electrostatics, viscoelastic stresses, and thermal development.

(iii) Examine the influence of key dimensionless parameters (Weissenberg, Brinkman, Peclet, and electrokinetic coupling numbers) on flow, potential, and temperature fields.

(iv) Quantify entropy generation and Bejan number distributions to assess thermal and hydrodynamic irreversibilities.

(v) Establish correlations for pressure drop, heat transfer, and entropy generation to guide microchannel design and performance optimization.

The analytical outcomes are intended to furnish a predictive toolset for characterizing coupled electro-thermo-rheological transport in microfluidic systems, enabling detailed insights into flow resistance, heat transfer efficiency, and thermodynamic losses. The proposed framework thereby provides a physically consistent basis for optimizing microchannel-based energy transport devices, particularly in applications involving viscoelastic biofluids, ionic polymer solutions, and functional thermal interfaces.

1.8 Practical Significance and Engineering Relevance of Study

The findings of the present study have direct implications across several microfluidic and energy transport applications, where the interplay of electrokinetic, thermal, and viscoelastic effects governs performance:

- *Electrokinetic flow characterization and control*: The detailed formulation and analysis of combined pressure-driven and electroosmotic viscoelastic flow provide useful insights for microfluidic bioassays and lab-on-chip diagnostic devices, where controlling flow rate and sample transport under simultaneous electric field and pressure gradients is crucial. This is particularly relevant to microfluidic system design in organ-on-chip devices and bioassay platforms [1], [3], [11], , foundational electrokinetic theory, and viscoelastic electroosmotic modeling developments [31], [54], [58]..

- *Thermal field and Joule heating analysis:* The modelling of thermally developing conditions and localized heat sources (Joule heating and viscous dissipation) directly supports the design of on-chip thermal management systems, temperature-regulated biochemical reactors, and microfluidic heat exchangers. Classical and recent studies on microscale thermal transport [12], [14], [36], Joule heating effects [35], [38], and microchannel thermal engineering [13], [16]underline the importance of accurate prediction of temperature fields and thermal gradients in electrokinetic environments.
- *Entropy generation and second-law evaluation:* The quantification of entropy generation and Bejan number distribution forms a basis for optimizing energy-efficient microchannel heat exchangers, ionic polymer actuators, and microscale cooling systems. Prior works on microscale irreversibility and entropy minimization in electrokinetic and non-Newtonian systems [15], [32], [59] highlight how transport irreversibilities can be used as a design metric to identify thermal- or hydrodynamic-dominated regimes.
- *Parametric correlations for design optimization:* The correlations established for Nusselt number, pressure drop, and entropy generation enable predictive design of electro-thermo-rheological transport systems involving polymeric electrolytes, viscoelastic biofluids, and non-Newtonian coolant mixtures. Foundational contributions on electroosmotic heat transfer [29], [34], [38], non-Newtonian and viscoelastic electrokinetic transport [39], [53], [55], and microchannel energy transfer provide the underlying basis for developing such engineering correlations. [60], [61]Overall, the proposed framework provides a unified theoretical and computational foundation for optimizing microchannel-

based electrokinetic transport devices, enhancing thermal control precision, and reducing energy losses in practical microfluidic and microscale energy systems.

1.9 Thesis layout

The remaining part of this thesis is organized as follows.

In **Chapter 2**, an overview of the literature pertinent to the present research has been given.

In **Chapter 3**, illustrates hydrodynamic performance combined electroosmotic and pressure-driven sPTT flow.

In **Chapter 4**, analyzed the hydrodynamic performance streaming potential mediated sPTT flow

In **Chapter 5**, analyzed the combined electroosmotic and pressure driven heat transfer, for viscoelastic sPTT model in thermally developing regime

In **Chapter 6**, presents the streaming potential mediated sPTT flow heat transfer, for viscoelastic sPTT model in thermally developing regime.

Finally, in **Chapter 7**, some important conclusions are enumerated from the studies executed as a part of the present thesis, and possible avenues for future research are also discussed.

Chapter 2. Literature Review

This chapter presents a systematically organized review of the prior research on electrokinetically modulated flow of viscoelastic fluids in parallel-plate microchannels, with a focus on key developments, modeling approaches, and coupled physical phenomena. The literature is broadly categorized as follows:

2.1 Electrokinetic Perspective in Microfluidic Systems

Outlines the general framework of electrokinetic transport phenomena relevant to confined fluidic domains at microscales.

2.2 Heat Transfer Perspective in Microfluidic Systems

Outlines the general framework of electrokinetic transport phenomena relevant to electrokinetically mediated to a thermally developed and thermally developing domain in microchannel

2.1 Electrokinetics Perspective in Microfluidic Systems

From an electrokinetic perspective, microfluidic transport processes are primarily influenced by interactions at the solid-liquid interface, where electrostatic forces dictate fluid movement. Electrokinetic effects like electroosmosis and streaming potential are central to the operation of microfluidic systems, offering precise control over fluid flow, particle movement, and separation. These processes are governed by factors like surface charge, ionic strength, and pH, which can be tuned to optimize the performance of microfluidic devices. The ability to manipulate fluids at this small scale with electric fields is the foundation for numerous applications in chemical analysis, diagnostics, and biomedical research.

Ramos [62] comprehensive volume delves into the theoretical and applied aspects of electrical manipulation of colloidal particles and fluids in microsystems. Dongqing Li [63] systematically reviews electrokinetic microfluidics processes for lab-on-a-chip applications, covering modeling, numerical simulation, and experimental studies essential for those new to the field. . Masliyah [64] text serves as a definitive resource for understanding the complex interplay between electrokinetic effects and colloidal

transport, particularly in fields such as chemical engineering, environmental science, and microfluidics.

Further the seminal review by Stone et al.[11] provided an engineering perspective on fluid manipulation within microdevices, highlighting the interplay between surface forces and hydrodynamic behavior in confined geometries Whitesides[65] later elaborated on the broader potential of microfluidics, emphasizing it's revolutionary implications across disciplines. The theoretical underpinnings of microfluidic flow, including electrokinetic transport, are extensively detailed by Bruus[18] , who addressed the governing equations and boundary conditions relevant to EOF, while Hunter [10] laid the groundwork for understanding zeta potential and electrokinetic mobility in colloidal systems.

Further, Karniadakis et al.[66] provided an in-depth account of fluid behavior in micro- and nanoscales, encompassing both Newtonian and non-Newtonian regimes, and incorporating simulation-based approaches. Oliveira and Pinho [67] developed closed-form solutions for velocity and stress fields in pressure-driven flow of sPTT fluids, offering key insights into the elastic Deborah number dependence of stress relaxation. While their work did not include electrokinetic effects, it laid the foundation for subsequent electrohydrodynamic studies.

Bazant [68]unifies electrokinetics and electrohydrodynamics to model complex electro-driven flows in microfluidic and porous systems, emphasizing nonlinear, coupled transport under strong fields and charge heterogeneity. Therefore, we conclude that, from an electrokinetic perspective, microfluidic transport is driven by solid-liquid interface interactions where electrostatic forces govern fluid motion. Thus, electrokinetic transport enables precise microfluidic control via electric fields at charged interfaces. These phenomena underpin LOC applications in diagnostics and chemical analysis electrostatic forces govern fluid motion.

2.1.1 Historical Development of Electrokinetic Flow

Electrokinetic phenomena refer to fluid and ion transport processes that occur at charged solid–liquid interfaces under the influence of electric fields. These include electrophoresis, electroosmosis, sedimentation potential, and streaming potential, all governed by the structure and dynamics of the electric double layer (EDL). Our study

specifically investigates electroosmotic flow and streaming potential, which are central to the performance and control of microfluidic systems.

The phenomenon of electroosmotic flow (EOF) represents a fundamental mechanism of fluid transport in charged capillary systems and has become increasingly important with the rise of microfluidic technologies. The history of electroosmotic flow is a blend of empirical observations, theoretical developments, and experimental validations, which have propelled its wide array of applications. This mechanism plays a vital role in a wide range of modern applications, including lab-on-a-chip systems, electrophoretic separations, drug delivery, and biosensing devices.

The first recorded observation of electroosmotic flow (EOF) was made by Franz Ernst Reuss[69] in 1809, a Russian-German botanist and physiologist. In his experiments, Reuss applied an electric potential across natural clay-filled glass capillary tubes and observed the movement of water through the clay. He correctly inferred that the flow was caused by electrical forces, marking one of the earliest empirical insights into electrokinetic phenomena. Although the concept of the electric double layer (EDL) had not yet been developed,

Reuss's findings laid the foundation for the modern understanding of EOF.The term "electroosmosis" and its theoretical foundation remained underdeveloped until the 19th century. In the 1830s, Michael Faraday advanced the understanding of ionic conduction through his work on electrolysis and the formulation of the Faraday constant. Although he did not directly study electroosmotic flow, his insights into ion transport under electric fields laid the groundwork for later developments in electrokinetics.

Helmholtz[70] (1879) introduced the electric double layer (EDL) model, identifying a compact Stern layer and a mobile diffuse layer of counterions at charged interfaces. He showed that an applied electric field mobilizes ions in the diffuse layer, inducing electroosmotic flow (EOF). This model established the theoretical foundation for electrokinetic transport.

Smoluchowski[9] (1903) refined Helmholtz's model by introducing the zeta potential (ζ), which measures the potential difference between fixed and mobile ions. He developed the Helmholtz-Smoluchowski equation, linking EOF velocity. In the 1940s and 1950s, the theoretical work by Helmholtz and Smoluchowski was experimentally

validated and expanded upon. One of the key contributions came from L.G. Overbeek and B.V. Derjaguin [71]They work on the electric double layer and zeta potential in colloidal systems. They clarified the relationship between surface charge, zeta potential, and electrokinetic behavior, confirming the principles of electroosmotic flow. Modeling electroosmotic flow (EOF) in micro- and nanofluidic systems requires solving the coupled Poisson–Boltzmann and Navier–Stokes equations to account for electrostatic potential and fluid motion, respectively.

Levine et al. (1975)[72] extended this work to narrow parallel-plate channels, incorporating EDL overlap, surface charge, and fluid viscosity , laying the theoretical groundwork for EOF in confined microchannel environments.

Studies by Squires and Bazant [73] have shown that EOF is indeed proportional to the zeta potential and the applied electric field. Their experimental data aligned with theoretical predictions based on the Poisson-Boltzmann equation and Smoluchowski's theory.Thus we conclude, historical and theoretical advancements in electroosmotic flow (EOF) provide the foundational framework for innovations in microfluidic device engineering.

2.1.2 Electrokinetic effects in Newtonian fluid flow

Electrokinetic phenomena in Newtonian fluids have been extensively studied, providing a foundational understanding crucial for advancements in microfluidic technologies. Smoluchowski[9] developed the Helmholtz–Smoluchowski equation, which gives key relationship between the electroosmotic velocity to zeta potential and applied electric field in the thin electric double layer (EDL) limit forming the foundation for EOF predictions in Newtonian fluids.

Building on Smoluchowski's work, Rice and Whitehead[65] developed an analytical solution for electroosmotic flow (EOF) in cylindrical capillaries, solving the Poisson–Boltzmann and Navier–Stokes equations, which became a benchmark for EOF studies in Newtonian fluids. Hunter[10] expanded on electrokinetic phenomena, focusing on surface charge and zeta potential effects in his monograph.

Levich [74]integrated electrostatic field theory with viscous hydrodynamics, emphasizing ionic distributions and channel geometry in electrokinetic flows. These classical models collectively form the theoretical foundation for electroosmotic and

streaming flows in Newtonian fluid have direct applications in microfluidic design. While early works established foundational principles, recent research has focused on complex geometries, time-varying electric fields, surface charge modulation, and multi-physics coupling.

Comprehensive reviews by Squires and Quake [73] and Schoch et al[75]emphasized the dominance of surface forces over volumetric forces at microscale dimensions, highlighting the importance of wall properties such as surface potential and channel geometry.

Dutta and Beskok[76] developed one of the earliest analytical frameworks for electroosmotic flow (EOF) in rectangular microchannels, incorporating effects of finite EDL and surface conduction, which become significant under low ionic strength conditions or high surface potentials.Their theoretical treatment, although developed for Newtonian fluids, noted that deviations from classical predictions can still arise under extreme confinement or high field strengths.

Tang et al[77]investigated electroosmotic flow (EOF) of Newtonian fluids in microchannels with complex boundary conditions, emphasizing the influence of wall potential and electric double layer (EDL) overlap on flow profiles. Their numerical approach accurately captured EOF behavior under moderate to high surface potentials, extending beyond the limitations of the Debye–Hückel approximation and offering deeper insights into Newtonian electrokinetic transport in confined geometries.

Zhao and Yang et al.[30] analyzed unsteady electroosmotic flow (EOF) of Newtonian fluids under time-varying electric fields, demonstrating that specific field frequencies and amplitudes can induce flow reversal. Their work highlights the potential of dynamic electric control for enhanced mixing and bidirectional pumping in microfluidic systems.

Chakraborty et al. [78]explored the use of streaming potential in Newtonian fluids as a diagnostic signal in miniaturized biosensors. Their study highlighted how pressure-driven flow through charged microchannels can produce measurable streaming voltages sensitive to ionic and surface property variations, offering a label-free sensing approach grounded in electrokinetic transport principles.

Bhattacharjee et al. [79] provided an analytical solution for electroosmotic flow in a microchannel with porous walls, focusing on Newtonian fluids. Their study examined

the effects of wall suction velocity, electrolyte concentration, and channel dimensions on velocity and pressure fields, contributing to the design of efficient microfluidic devices. Mahapatra and Bandopadhyay [80] analyzed alterations in electroosmotic slip velocity considering the combined effect of viscoelasticity and surface potential undulation. While focusing on viscoelastic fluids, their findings also provide insights into how surface potential variations can influence slip velocity in Newtonian fluids.

Bandopadhyay and Chakraborty [81] studied the influence of steric effects arising from the finite size of ions on streaming potential and electrokinetic energy conversion in Newtonian fluid flows through microchannels by incorporating modified Poisson–Boltzmann equations. Chakraborty et al. [82] explored the use of streaming potential in Newtonian fluids as a diagnostic signal in miniaturized biosensors. Their study highlighted how pressure-driven flow through charged microchannels can produce measurable streaming voltages sensitive to ionic and surface property variations, offering a label-free sensing approach grounded in electrokinetic transport principles.

Azari et al.[83] developed a theoretical model capturing the entrance effects and electric double layer (EDL) relaxation in transient electroosmotic flow (EOF) of Newtonian fluids, emphasizing the dynamic coupling between EOF and streaming potential during the start-up of electrokinetic pumps.

Despite the simplifications inherent in the Newtonian fluid assumption, these models remain invaluable for analyzing microscale electrokinetics. The linear rheology allows for closed-form solutions under certain conditions and provides a baseline for assessing deviations in non-Newtonian systems. Therefore, electrokinetic flow of Newtonian fluids continues to be a cornerstone of microfluidic transport analysis.

2.1.3 Electrokinetic effects in non-Newtonian and viscoelastic fluid flow

The study of electrokinetic transport in microchannels has expanded significantly with the consideration of non-Newtonian fluid behavior, owing to its relevance in lab-on-a-chip and biomedical applications. Initial investigations into the rheological aspects of electrokinetic flow were conducted by Zimmerman et al.[84], who performed experimental rheometry of non-Newtonian fluids in a microchannel T-junction. Their work highlighted the complex flow field interactions at junctions, which are critical in microfluidic network design. Das and Chakraborty[39]provided analytical solutions for electroosmotic flow of a non-Newtonian bio-fluid. Their approach modeled the fluid as

a power-law type and considered temperature and concentration distributions, offering a comprehensive understanding of coupled transport phenomena in microchannels.

Zhao et al.[85]analyzed electroosmotic flow in slit microchannels for power-law fluids and derived closed-form solutions for velocity profiles. Their study emphasized the influence of the flow behavior index on the electroosmotic flow rate, showing deviations from classical Newtonian behavior. In a subsequent study, Ji et al.[86] investigated the impact of viscoelasticity on electroosmotic flow using numerical simulations based on the Phan-Thien–Tanner model. They reported significant alterations in flow patterns and volumetric throughput, particularly under low zeta potential conditions.

Berli [87]explored the performance of electrokinetic pumps when transporting non-Newtonian fluids. The analysis revealed that pump efficiency and generated pressure are sensitive to fluid rheology, particularly for shear-thinning characteristics, thereby affecting microfluidic device performance.

Berli and Olivares [88]theoretical study examines electrokinetic flows of non-Newtonian fluids, modeled using power-law constitutive equations, in slit and cylindrical microchannels. It highlights that shear-dependent viscosity primarily affects the pressure-driven component of the flow, while electroosmotic flow remains largely unaffected. Vakili et al. [89] developed a numerical framework for electrokinetic flow of power-law fluids in rectangular microchannels, incorporating electric double layer (EDL) effects with varying aspect ratios. Their results underscored the influence of both channel geometry and non-Newtonian properties on the flow field and electrokinetic transport efficiency.

Zhao et al[32]comprehensive review discusses various electrokinetic phenomena involving non-Newtonian fluids, including electroosmosis, electrophoresis, and streaming potentials. It emphasizes how shear-thinning fluids tend to enhance electrokinetic effects, whereas shear-thickening fluids may diminish them. The paper also outlines theoretical challenges and future research directions in the field.

Das and Chakraborty[39] and Chakraborty [90] analytically investigated EOF of typical non-Newtonian biofluids (e.g., blood, mucus, and polymeric drug carriers) in microchannels. Their studies modeled these fluids as power-law fluids, focusing on how viscosity changes with shear rate and how that influences flow velocity, temperature, and

solute concentration under electroosmotic driving forces. The study highlighted how channel geometry and fluid rheology influence the flow rate and electric field distribution. It provided insights into capillary transport of biological fluids, aiding the design of microfluidic devices for biomedical applications.

Tang et al.[77]investigated electroosmotic flow of non-Newtonian fluids in microchannels, focusing on the impact of shear-thinning and shear-thickening behaviors. They found that these rheological properties significantly alter the velocity profiles and flow characteristics compared to Newtonian fluids.

In studies by Deng et al.[91] and Vasu and De[92] , EOF of power-law fluids was analyzed under high zeta potential conditions, where nonlinearities in electrokinetic and flow fields become significant. The non-Newtonian fluids modeled were again characterized by power-law rheology, with parameters aligned with biological fluids such as synovial fluid, blood plasma, and artificial saliva.

Bharti et al[93]explored electroviscous effects in fully developed EOF of power-law liquids in cylindrical channels, noting the increased apparent viscosity at low shear rates—a key consideration when designing EOF systems for polymer-based solutions used in separation sciences or pharmaceutical microdevices.

Zhao and Yang [32], [94]contributed extensively to this area through a series of studies. In their studiesthey presented an analytical solution for electroosmotic flow of power-law fluids in planar microchannels, identifying key scaling behaviors with respect to the power-law index. Their study applicable to high-surface-charge environments encountered with thickened mucosal secretions or polymer-enriched biofluids.

The study highlighted the importance of considering fluid rheology when designing microfluidic systems for applications involving complex fluids. Unlike Newtonian fluids, viscoelastic fluids exhibit memory effects, which complicate the interaction between the applied electric field, the induced electroosmotic flow (EOF) and streaming potential field–flow coupling is significant.

Liu et al.[95] analyzed electroosmotic transport of Jeffreys fluids, a more generalized viscoelastic model incorporating both relaxation and retardation times. Their findings emphasized the importance of the retardation time in controlling the degree of flow retardation near the walls, especially when the EDL is thin relative to channel height.

Escandon et al.[96] performed further numerical analysis of generalized Maxwell fluids in slit channels, accounting for nonlinear coupling between streaming potential and elastic stresses, reinforcing the role of elasticity in suppressing backflow regions under strong pressure gradient. Studies involving more complex models such as Oldroyd-B and PTT fluids are fewer but growing.

Afonso et al[53]. primarily investigated pure electroosmotic flow (EOF) of viscoelastic fluids modeled with the simplified Phan–Thien–Tanner (sPTT) equation, under asymmetric zeta potentials. Their study did not include pressure-driven (PD) flow components, focusing solely on the effects of electrokinetic forces and viscoelasticity.

Sarma et al. [97] developed an exact analytical model for electroosmotic flow of PTT fluids using the full nonlinear Poisson–Boltzmann equation, extending validity beyond the Debye–Hückel limit. Their results showed that viscoelastic effects, including shear thinning and elasticity, significantly modify velocity profiles and enhance EOF compared to Newtonian predictions.

2.1.4 Mixed Electroosmotic and Pressure-Driven Transport in Newtonian and Non-Newtonian Fluids

The combined effects of electroosmotic flow (EOF) and pressure-driven (PD) flow in microfluidic systems have garnered significant attention in recent years due to their potential to enhance fluid control and optimize the performance of lab-on-a-chip devices. The interaction between these two driving forces plays a crucial role in determining the flow dynamics. Early research on the combined electroosmotic flow (EOF) and pressure-driven (PD) flow primarily concentrated on Newtonian fluids. The theoretical groundwork laid by Burgreen and Nakache[98] and Dutta and Beskok[76] provided a solid foundation for understanding EOF in microchannels. However, the inclusion of PD flow into these electroosmotic models became a critical step forward in capturing more realistic fluid behavior in confined geometries. A key advancement was the work of Huang et al[99]., which analyzed the combined EOF and PD flow in Newtonian fluids within microchannels. They showed that the interplay between the electric field and pressure gradient could either augment or oppose fluid motion, depending on their relative strengths, with flow behavior strongly influenced by zeta potential and Reynolds number.

Arulanandam and Li[37] work provides a technically rigorous framework for analyzing electrokinetic transport under mixed EOF–PD driving force in Newtonian fluids. While emphasizing EOF, the study incorporates pressure-driven effects by solving coupled Poisson–Boltzmann and Navier–Stokes equations, with attention to entrance effects and surface conduction under asymmetric inlet/outlet conditions. Mahpatra et al.[80] validated combined EOF and PD flow, showing that pressure-driven forces strongly influenced near-wall velocity profiles, while electroosmotic effects modified bulk flow behavior and overall pressure drop. Kumar et al.[100] numerically modeled combined electroosmotic and pressure-driven flow in microchannels for Newtonian fluids, highlighting how adjusting pressure and electric field strength influences flow characteristics, offering insights for microfluidic device design. There are similar more studies which collectively contribute to a comprehensive understanding of the interplay between electroosmotic and pressure-driven flows in Newtonian fluids, particularly within microchannel environments.

The combined effects of electroosmotic (EOF) and pressure-driven (PD) flow in non-Newtonian fluids have been the subject of extensive research due to their relevance in microfluidic applications. Vasu and De[92] expanded on this by investigating EOF and PD flow in power-law fluids. Their study focused on the high-zeta potential regime, where nonlinear electrokinetic effects become significant. They demonstrated that the non-Newtonian viscosity variation with shear rate alters the axial velocity distribution, influencing both flow resistance and flow profiles in microchannels under combined EOF and PD conditions. Oliveira et al. [58]explored the coupling between electroosmotic and pressure-driven flows in viscoelastic fluids. Their analysis showed that viscoelastic stresses significantly distort the traditional EOF plug flow profile, creating broader shear layers and modifying axial stress distributions.

Yao et al[101] provided early insights into this interaction, examining the influence of non-Newtonian fluid rheology, particularly shear-thinning behavior, on the electrokinetic flow dynamics in microchannels. Their findings highlighted the impact of fluid viscosity variations on both electroosmotic and pressure-driven components, laying the groundwork for further exploration in this area. These results underscore the complexity of electrokinetic transport in viscoelastic fluids, where elastic effects can lead to higher flow resistance and more intricate flow patterns. Mahapatra et al.[31] focused on the combined EOF and PD flow of power-law and Oldroyd-B fluids in microchannels,

offering insights into how shear-thinning behavior influences flow dynamics. Their study revealed that shear-thinning fluids exhibit enhanced electroosmotic mobility in high shear rate regions, contrasting with the behavior of Newtonian fluids. This highlighted the importance of accounting for fluid rheology in systems where both EOF and PD effects are present.

Ferras et al.[54] developed an semianalytical model for non-Newtonian fluid flow in microchannels incorporating both EOF and PD components. Their work emphasized the role of surface conduction and the coupling of electroosmotic forces with pressure gradients, providing a framework for predicting fluid behavior in microfluidic systems with complex fluid properties. Building upon this, Dhinakaran et al.[102] investigated the combined effects of electroosmotic flow (EOF) and pressure-driven (PD) flow in non-Newtonian fluids using the sPTT model. They solved the coupled momentum and Poisson–Boltzmann equations, highlighting how viscoelastic effects induce velocity gradient curvature and flow asymmetry near the electric double layer (EDL).

Babaie et al.[103] studied the combined effects of electroosmotic and pressure-driven flow for power-law non-Newtonian fluids in a slit microchannel. Using analytical methods, they demonstrated how the superposition of electrical and pressure forces influences velocity profiles, flow rate, and shear distribution. Their findings underscore the role of fluid rheology and flow mechanism interaction in optimizing microfluidic transport of non-Newtonian fluids.

However the study by Mondal et al [104] does not specifically mention a particular viscoelastic fluid in their analysis of combined electroosmotic and pressure-driven flow in microchannels under high zeta potential and overlapping EDL conditions. Their work primarily focuses on the general behavior of viscoelastic fluids and how their elastic and shear-thinning properties influence flow profiles and pressure drops.

Afonso et al. [53] utilized both the Finitely Extensible Nonlinear Elastic-Polynomial (FENE-P) model and the Phan-Thien-Tanner (PTT) models to analyze electrokinetic effects in microfluidic systems. The FENE-P model emphasizes the finite extensibility and elastic deformation of polymer chains, while the PTT model accounts for shear-thinning and viscoelastic relaxation. The combined use of these models allowed the authors to examine how elasticity, shear-thinning, and finite extensibility impact electroosmotic and pressure-driven flow interactions. The FENE-P model showed that

elasticity increased flow resistance under high zeta potential, while the PTT model's shear-thinning behavior reduced viscosity in high shear rate regions, leading to distinct flow responses. Additionally, the elastic recovery in the PTT model introduced a time-dependent flow behavior.

On the other hand, Ferrás et al.[54] utilized a Jeffrey model of viscoelasticity, which is commonly used for describing complex fluids, especially in the context of non-Newtonian behavior. The Jeffrey model accounts for both elastic and viscous effects, making it suitable for analyzing electroosmotic and pressure-driven flow of viscoelastic fluids in microchannels. They found that the non-Newtonian behavior could either amplify or dampen the effects of EOF and PD flow depending on the flow conditions and microchannel geometry. Oliviera et al. [58]advanced the understanding of combined EOF flow in shear-thinning fluids, focusing on how viscosity variations with shear rate influence electroosmotic mobility and flow resistance. Their study provided critical insights into the design of microfluidic devices operating with non-Newtonian fluids, emphasizing the need to account for shear rate-dependent viscosity in electrokinetic transport models.

These studies collectively contribute to the understanding of electrokinetic flow in non-Newtonian fluids, highlighting the significant role of fluid rheology in shaping the behavior of EOF and PD flow interactions. The findings emphasize the necessity for accurate modeling approaches to predict flow dynamics in microfluidic systems, where both electrostatic and hydrodynamic forces influence transport phenomena.

2.1.5 Streaming Potentials and Electroviscous Effects

The streaming potential, arising due to the convective transport of excess ionic charge within the electric double layer (EDL) during pressure-driven flow, plays a critical role in regulating electrohydrodynamic transport in confined microfluidic systems. In Newtonian fluids, this phenomenon introduces electroviscous effects via an induced back electric field that opposes the primary flow. However, in the presence of non-Newtonian rheology—including shear-thinning, shear-thickening, and viscoelastic behavior—the streaming potential interacts nonlinearly with the flow field, modifying charge distribution, electroosmotic backflow, and pressure–velocity relations. The following studies illustrate the distinct physical consequences of streaming potential in microflows of complex fluids. Mansouri et al.[105] presented a theoretical analysis of the time-

dependent development of streaming potential in finite-length microchannels under Newtonian pressure-driven flow. Their formulation, based on the coupled Poisson–Nernst–Planck and Navier–Stokes equations, captured the transient evolution of the electric field during flow startup. A key observation was the emergence of oscillatory electric potential profiles characterized by overshoots and phase lag between the pressure-driven flow and induced streaming current. The induced field acts in opposition to the driving pressure gradient, reducing the net flow rate during the transient phase. Importantly, this back electroosmotic field varies dynamically, leading to time-dependent electroviscous retardation. In time-sensitive operations—such as pulsed injection or pressure-driven gating—the evolving streaming potential introduces unsteady flow resistance, necessitating temporal resolution in modeling for accurate prediction of transport rates.

Bandopadhyay et al.[106] examined capillary filling of immiscible electrolytes in microchannels under a two-phase pressure-driven conFiguration. The presence of contrasting ionic conductivities and zeta potentials across the displacing and displaced phases led to significant streaming potential generation at the interface. This induced field exerted an electroosmotic force that opposed the meniscus motion. A dynamically evolving back electric field altered the net pressure head, resulting in a non-monotonic meniscus velocity. The capillary front experienced temporary deceleration due to electroosmotic counterflow initiated by streaming potential buildup. Streaming potential introduces a self-regulating feedback mechanism in multiphase flows, offering passive modulation of capillary filling dynamics. This is particularly relevant to digital microfluidics and microemulsion devices, where phase interfaces are prevalent.

Chakraborty et al.[78] investigated the influence of viscoelasticity on streaming potential generation under mixed electroosmotic and pressure-driven conditions. Their analysis revealed that elastic memory effects significantly affect the distribution of ionic species and the magnitude of the induced electric field. Streaming potential was shown to increase nonlinearly with Deborah number. Viscoelastic relaxation induced a phase delay in charge transport, leading to enhanced backflow and a reduction in apparent mobility. In biofluids with intrinsic elasticity (e.g., DNA solutions), streaming potential amplifies electroviscous effects, modifying volumetric throughput and effective electrokinetic transport parameters. Accurate device performance modeling must incorporate viscoelastic-electrostatic coupling. Vasu and De[107] analytically studied electroviscous

corrections in pressure-driven flows of power-law fluids within microchannels. They considered both symmetric and asymmetric wall zeta potentials and evaluated the streaming potential and corresponding flow alterations.

Shear-thinning fluids exhibited elevated streaming potentials due to enhanced near-wall shear and stronger EDL convection. Conversely, in shear-thickening fluids, the reduced wall shear suppressed streaming current, yielding lower potential values. The streaming potential altered the effective pressure gradient, introducing a non-Newtonian dependence in flow resistance. Streaming potential introduces a tunable electroviscous resistance, dependent on rheological parameters. This enables passive flow regulation strategies in microreactors and flow control networks without external actuation.

Pal et al[108] explored the coupled interaction between viscoelastic Oldroyd-B fluid flows and compliant channel walls under electrokinetic forcing. Wall deformation and fluid elasticity were shown to affect both flow kinematics and induced streaming potential.

Streaming potential was enhanced by normal stress differences and wall compliance, resulting in nonlinear feedback between electric field distribution and structural deformation. This gave rise to unstable flow regimes, where small pressure variations induced abrupt flow changes. The streaming potential acts as an active player in soft microfluidic systems, where electroelastic interactions can be leveraged to design passive bistable valves, memory elements, or tunable resistive components.

Sarkar[48] examined pressure-driven flow of PTT viscoelastic fluids under streaming-potential effects, showing strong electrohydrodynamic coupling in confined microchannels. The work highlighted how viscoelasticity and shear-thinning significantly modify flow rate and electrokinetic response compared to Newtonian behavior.

Berli et al. [109]investigated electroosmotic transport in macromolecular fluids, emphasizing the formation of depletion layers near channel walls. These layers, devoid of large polymeric species, altered the EDL structure and ionic strength distribution.

Depletion-induced modification of the near-wall ion environment reduced the streaming current, thereby suppressing the magnitude of the streaming potential. This led to diminished electroosmotic backflow and reduced flow uniformity. In macromolecule-

rich environments, such as protein or DNA assays, streaming potential suppression must be accounted for to ensure accurate control of electrophoretic and electroosmotic processes.[110]

Thus streaming potential is not merely a secondary phenomenon but a central determinant in the electrohydrodynamics of non-Newtonian and viscoelastic microflows. Its dynamic coupling with flow kinematics, interfacial charge distribution, and viscoelastic stress evolution significantly alters transport characteristics in confined systems. Accurate modeling of such flows especially under thermally developing, transient, or soft-walled conditions requires a fully coupled treatment of electrokinetics and fluid rheology. Therefore, as demonstrated in recent analytical and numerical studies, incorporating streaming potential feedback is essential for predicting flow reversal, pressure anomalies, and energy conversion efficiency in next-generation lab-on-chip and electrokinetic energy harvesting platforms.

2.1.6 Electrokinetically mediated thermofluidic transport in microchannel

Electrokinetically driven flows in microchannels under thermal gradients are crucial for thermal management, energy conversion, and lab-on-a-chip systems. These flows exhibit either thermally developing or thermally developed characteristics depending on thermal entrance length and boundary conditions. The heat transfer performance and entropy generation[111] in these regimes are influenced by the nature of the fluid—Newtonian, non-Newtonian (e.g., power-law), or viscoelasticand the coupling between electrokinetic (EOF), pressure-driven (PD), magnetohydrodynamic (MHD), and streaming potential effects.

Thermally Developing Electrokinetic and Mixed Flows

In microfluidic systems, the thermally developing region plays a pivotal role in determining entrance-length-dependent temperature and velocity fields. Understanding this region is essential for the optimization of microchannel designs where thermal gradients evolve spatially. Iverson et al.[112] investigated thermally developing electroosmotic flow (EOF) convection in rectangular microchannels assuming a vanishing Debye-layer thickness. The working fluid was Newtonian, and the flow was purely EOF. The study revealed that thermal entrance effects are significant under such conditions. Axial conduction dominated the early region of the channel, causing pronounced deviation from fully developed thermal profiles. The temperature and

Nusselt number exhibited strong axial variations, and entropy generation was localized near the walls due to steep thermal gradients.

Broderick et al.[113] extended this analysis by incorporating finite Debye-layer thickness in Newtonian EOF flow. The presence of finite EDL led to more pronounced temperature gradients near the wall and spatial variation in electroosmotic body force, intensifying local thermal irreversibility. A noticeable increase in viscous dissipation and Joule heating magnified total entropy generation in the entrance region.

Ganguly et al.[55] analyzed thermally developing nanofluid flow under combined EOF + PD + MHD transport. Nanoparticles enhanced thermal conductivity, improving axial heat conduction and flattening temperature profiles. However, an applied magnetic field induced Lorentz forces, leading to intensified Joule heating and spatially non-uniform entropy generation, especially near the channel walls.[42]

Thermally Developed Electrokinetic and Mixed Flows

In the thermally developed region, thermal and hydrodynamic fields reach a steady conFiguration that governs long-channel heat transfer performance. From a microfluidic design perspective, this regime provides predictable thermal behavior essential for consistent device performance.

Maynes and Webb[34] presented analytical results for thermally developed EOF in Newtonian fluids. The velocity profile remained nearly flat across the cross section, minimizing wall shear and suppressing viscous dissipation. Consequently, entropy generation was low, and the Nusselt number approached a constant value, confirming a well-developed thermal regime.

Liechty et al.[114] studied fully developed EOF in Newtonian microtubes under high zeta potential. Elevated wall potential induced strong Joule heating, which dominated the energy equation and raised bulk temperatures. The higher temperature gradients increased thermal irreversibility, resulting in greater entropy production, particularly at the wall-fluid interface.

Sarkar et al.[61] explored thermally developed EOF + PD + MHD nanofluid flow. The synergistic impact of nanoparticles and magnetic fields was highlighted. While nanoparticles improved thermal conduction, the magnetic field increased energy dissipation via the Lorentz force. Entropy generation analysis revealed that

thermomagnetic effects significantly altered heat transfer uniformity and second-law efficiency.

Sadeghi et al[115] focused on fully developed EOF of viscoelastic fluid (PTT model) in a slit microchannel with stepwise wall temperature variation. Elastic stress altered thermal diffusion, resulting in localized peaks in temperature and entropy generation. The fluid's memory effect damped the response to thermal discontinuity, indicating a trade-off between thermal responsiveness and entropy minimization.

Goswami et al.[59], [60] investigated EOF of viscoelastic fluids in slit microchannels under fully developed thermal conditions. The analysis demonstrated that the elasticity of the fluid moderated temperature gradients and improved thermal uniformity. As a result, entropy generation decreased compared to Newtonian fluids under similar boundary conditions.

Roychowdhury et al.[116] studied a bi-layer thermally developed flow comprising a Newtonian and a power-law fluid under EOF + PD conditions. The stratification introduced additional complexity due to interfacial shear and mismatched thermal conductivities. Temperature development was asymmetric, and entropy generation concentrated near the interface due to viscous heating and interfacial resistance

2.1.7 Recent Works (post-2021) in Electrokinetic Viscoelastic Microflows

Yang et al.[117] investigated electro-osmotic flow of Maxwell fluids under alternating electric fields, showing strong dependence on elastic relaxation time and AC frequency. The study is isothermal and does not include nonlinear Poisson–Boltzmann formulation, streaming potential, or thermal effects.

Valencia[118] et al. analyzed start-up multilayer EOF of Maxwell fluids in annular microchannels with slip. Their transient formulation captures interfacial velocity mismatch, though nonlinear viscoelasticity (sPTT) and thermal coupling were not considered.

Chang et al.[119] examined AC EOF of Maxwell fluids with sinusoidally rough walls, demonstrating roughness-induced amplification in flow oscillation. The study is limited to AC forcing without electrothermal feedback.

Deng[120] provided analytical solutions for EOF of two immiscible power-law fluids, highlighting shear-thinning-controlled flow characteristics but excluding viscoelastic elasticity and thermal coupling.

Deng et al.[121] investigated unsteady two-layer EOF–pressure-driven flow with slip-dependent zeta potential. Their model does not incorporate viscoelastic stresses, Joule/viscous heating, or nonlinear PB-based EDL.

Bilal et al.[122] studied EO-EMHD hybrid nanofluid flow in cylindrical microchannels with thermal dissipation. The hybrid nanofluid rheology is treated as effective Newtonian, without viscoelastic modeling.

Barnoon et al.[123] explored EOF and heat transfer enhancement in hybrid nanofluids. The work lacks electroviscous feedback and viscoelastic transport physics.

Ren et al.[124] developed analytical solutions for unsteady EOF of Jeffrey fluids in circular microchannels. Although relaxation/retardation effects were captured, nonlinear elastic extensibility present in sPTT was not.

Yang et al.[125] presented exact solutions for EOF of second-grade fluids, which do not capture shear-thinning or strong viscoelastic effects.

Mehta et al.[126] investigated electroosmotic mixing of viscoplastic fluids, showing yield-stress-controlled initiation of motion, though elastic stress evolution was not considered.

Alyousef et al.[127] examined steady EOF of two-fluid viscoelastic Ellis fluids, focusing on shear-dependent viscosity but excluding electrothermal and elastic effects.

Chen and Lin[128] studied particle migration in Newtonian and power-law flows around obstacles. Since the study is not electrokinetic, it cannot predict EDL-dependent transport.

Kananipour[129] performed heat and mass transfer analysis of s-PTT nanofluid under EOF with slip, Brownian motion, and thermophoresis. Streaming potential and mixed EOF-PD conditions were not addressed.

Ahmad et al.[130] analyzed drag reduction and heat transfer in FENE-P fluids, focusing on polymer chain extensibility without electrokinetic effects.

Ponalagusamy et al.[131] studied EOF in two immiscible conducting and non-conducting fluids; the model excludes viscoelasticity and thermal feedback.

Davoodi et al.[132] compared sPTT and FENE-P constitutive models theoretically to identify similarity regimes, without application to electrokinetic microchannel flow.

Trivedi[133] performed numerical simulations of PTT EOF in diverging microchannels, explaining elasticity-controlled deformation but ignoring electrothermal interactions.

Khan et al.[134] demonstrated flow-switching and mixing instabilities of electroosmotic viscoelastic fluids via numerical and experimental analysis, but without sPTT modeling or energetic coupling.

Chen et al.[135]investigated electrokinetic instabilities in Boger fluids with conductivity gradients, showing instability thresholds for constant-viscosity elastic fluids.

Chen et al.[136] studied electrokinetic instability onset reduction in shear-thinning polymer solutions, without nonlinear PB-EDL coupling or thermal dissipation modeling.

2.2 Based on Literature review structured summary

Based on the literature review, a structured summary of contemporary studies is presented in the upcoming tables to identify unresolved research gaps, particularly in the coupled modeling of viscoelastic sPTT fluids, nonlinear PB-EDL interaction, EOF-PD flow superposition, and electro-thermal effects.

2.2.1 Classical / Newtonian electrokinetics

Table 2.1. Classical / Newtonian electrokinetics.

Prior work (as cited in thesis)	Model type / constitutive model	Major assumptions	EDL treatment	Rheology captured	Thermal coupling	Key limitation (critical)
Burgreen & Nakache (1964)	Newtonian analytical EOF	Thin-slit, low ζ often used with linearization	Debye–Hückel / thin-EDL approximations	Newtonian	No	Baseline model; not valid at high ζ or overlapping EDLs.
Dutta & Beskok (2001)	Newtonian analytical EOF+PD	Finite Debye layer effects, rectangular channel	Full finite-EDL effects considered analytically	Newtonian	No	Good finite-EDL detail but Newtonian-only.
Tang et al. (2009)	Newtonian numerical EOF	Complex boundary conditions, moderate–high ζ	Nonlinear PB in numerics	Newtonian	No	Accurate numerics but limited rheology scope.
Maynes & Webb (2003)	Newtonian heat transfer EOF	Fully-developed flow assumption	EDL through PB approximations	Newtonian	Yes	Thermal insight but Newtonian only.
Azari et al. (2020)	Newtonian transient EOF	Entrance + EDL relaxation, transient start-up	PB used to model EDL relaxation	Newtonian	No	Strong transient EDL coupling; lacks non-Newtonian effects.
Kirby (2010) (text)	Review / theory	Broad electrokinetic theory	Discusses PB / EDL models	Newtonian baseline	Yes	Foundational reference; not new modeling.
Bazant/Storey/ Kornyshev (2011)	Ionic liquids / double layer theory	Crowding & overscreening concepts	Beyond classical PB (ionic size effects)	Newtonian fluid background	No	Applicable where ionic specificity matters; complex physics.

2.2.2 Non-Newtonian / Power-law studies

Table 2.2. Non-Newtonian / Power-law studies.

Prior work	Model type	Major assumptions	EDL treatment	Rheology captured	Thermal coupling?	Key limitation
Zhao et al. (2008)	Power-law analytic EOF	Slit geometry, steady	Uses PB approximations; often high ζ considered	Power-law (shear thinning/thickening)	No	Good closed forms; no elasticity.
Vasu & De (2010)	Power-law, high ζ	High zeta potentials, nonlinear electrostatics	Full PB (address high ζ)	Power-law	No	Captures shear-dependence; no elasticity or thermal coupling.
Bharti, Harvie & Davidson (2009)	Power-law electroviscous	Fully-developed cylindrical flow	EDL effects included (approx)	Power-law	No	Electroviscous focus; limited geometry and no thermal coupling.
Babaie, Sadeghi & Saidi (2011)	Power-law EOF+PD analytic	Slit geometry, superposed EOF+PD	Thin or simplified PB for tractability	Power-law	No	Clear analytical results; no elasticity or thermals.
Das & Chakraborty (2006)	Non-Newtonian biofluid (analytical)	Power-law type; includes temp & concentration	EDL modeled; analytic simplifications	Power-law biofluid	Yes temperature considered	Good multiphysics but limited to power-law rheology.

2.2.3 Viscoelastic (Oldroyd-B, Maxwell, Jeffreys, FENE-P, PTT/sPTT)

Table 2.3. Viscoelastic (Oldroyd-B, Maxwell, Jeffreys, FENE-P, PTT/sPTT)

Prior work	Model type	Major assumptions	EDL treatment	Rheology captured	Thermal coupling	Key limitation
Dhinakaran, Afonso, Alves & Pinho (2010)	PTT (steady)	Parallel plates, steady	PB coupled with momentum	sPTT: viscoelastic + shear-thinning	No	Solid sPTT foundation; no thermals or streaming potential coupling.

Sarma et al. (2018)	PTT exact solution	High ζ beyond DH; parallel plate	Full nonlinear PB	PTT viscoelastic (shear-thinning, elasticity)	No	Important high-ζ theory; lacks thermal analysis.
Afonso et al.	FENE-P & PTT comparison	Focus on pure EOF, elasticity	Full PB in viscoelastic contexts	FENE-P (finite extensibility), PTT	Limited / typically no	Good rheology breadth; mostly for pure EOF, not mixed/thermal.
Escandón et al. (2015)	Maxwell transient EOF	Transient, asymmetric ζ	PB used	Maxwell (linear viscoelastic)	No	Transient viscoelastic insights but simplistic rheology.
Liu, Jian & Yang (2011)	Jeffreys (AC EOF)	Alternating current EOF	EDL modeled	Jeffreys (elastic + viscous)	No	AC field effects with simple viscoelastic model; limited thermal study.
Oliveira, Alves & Pinho (1999/2011)	PTT analytical / review	Fully-developed PTT solutions (channel/pipe)	EDL not the focus (rheology paper)	PTT viscoelastic	No	Foundational viscoelastic solutions but not electrokinetic-thermal coupled.
Huang et al. (2016)	Experimental + theoretical	Rectangular microchannel experiments	EDL effects included experimentally	Non-Newtonian / viscoelastic behavior measured	Possibly accounted in experiments	Valuable experimental validation; limited parameter sweep.
Ji (2022)	Numerical PTT	Numerical simulation of viscoelastic EOF.	PB numerically solved	Viscoelastic (PTT)	Not emphasized	Up-to-date numerics; details depend on simulation setup.

2.2.4 Mixed EOF + Pressure-Driven transport (Newtonian & non-Newtonian)

Table 2.4. Mixed EOF + Pressure-Driven transport (Newtonian & non-Newtonian)

Prior work	**Model type**	**Major assumptions**	**EDL treatment**	**Rheology captured**	**Thermal coupling?**	**Key limitation**
Huang et al. (Newtonian)	Newtonian EOF+PD	Coupled EOF & PD in microchannel	PB + Navier–Stokes	Newtonian	No	Demonstrates interplay of EOF/PD, Newtonian-only.
Mahapatra & Bandopadhyay (2021)	Viscoelastic numerical	High ζ, surface modulation	Full PB numerically	Viscoelastic (shear-thinning)	No	Good numerics for modulated surfaces; limited thermal coupling.

Mondal, Misra & De (2014)	High ζ + overlapping EDL	Overlapping EDL regimes	Overlapping EDL solved	Viscoelastic / general (not one model)	No	General results; specific constitutive details limited.
Ferrás et al.	Jeffrey model semianalytical	Non-Newtonian semianalytic EOF+PD	PB approximations	Jeffrey viscoelastic	No	Useful framework; limited to Jeffrey rheology.
Berli & Olivares (2008)	Power-law / non-Newtonian	Slit/cylindrical channels	EDL treated via PB approximations	Power-law / shear-dependent	No	Shows impact on pump efficiency; viscosity-only models.
Vakili et al. (2012)	Power-law numerical	Rectangular microchannels	EDL modelled with aspect ratio effects	Power-law	No	Geometry/rheology study; no thermals.

2.2.5 Streaming potential & electroviscous effects

Table 2.5. Streaming potential & electroviscous effects

Prior work	**Model type**	**Major assumptions**	**EDL treatment**	**Rheology captured**	**Thermal coupling**	**Key limitation**
Mansouri et al. (2005)	Transient EOF + streaming potential	Finite-length transient channel	PNP/streaming current included	Newtonian	No	Good transient streaming treatment; Newtonian-only.
Chakraborty et al. (various)	Streaming potential analyses	Streaming potential as diagnostic/control	PB / modified PB used	Mostly Newtonian; some non-Newtonian work	Some thermo referenced	Strong on streaming potential sensing; viscoelastic coupling limited.
Bandopadhyay & Chakraborty (steric effects)	Modified PB streaming	Steric finite-ion size effects	Modified PB (steric)	Newtonian in main examples	No	Demonstrates steric corrections; rheology scope narrow.
Mahapatra & Bandopadhyay (mixing with viscoelastic)	Numerical	Mixing over discrete electrodes	PB numerically solved	Viscoelastic considered	No	Shows mixing effects; streaming potential-rheology coupling still partial.
Bhattacharjee et al.	Porous-wall EOF analytic	Wall suction, porous wall effects	PB + wall boundary effects	Newtonian	No	Useful porous-wall results; not viscoelastic.

Sarkar	Modified PB streaming	No Slip, No steric effect.	PB semi analytical method	Viscoelastic	No	Thermal analysis not considered.

2.2.6 Thermal / Electrothermal / Entropy analyses (incl. Joule & viscous heating)

Table 2.6. Thermal / Electrothermal / Entropy analyses (incl. Joule & viscous heating)

Prior work	Model type	Major assumptions	EDL treatment	Rheology captured	Thermal coupling?	Key limitation
Horiuchi, Dutta & Hossain (2006)	Joule-heating EOF+PD	Constant wall heat flux studies	PB approximations	Newtonian	Yes — Joule heating included	Important electrothermal effects but Newtonian focused.
Sadeghi & Saidi (2010)	Viscous dissipation on thermal transport	Mixed EOF+PD with viscous dissipation	PB for electrostatics	Newtonian	Yes — viscous dissipation	Good thermal coupling; no viscoelastic rheology.
Yavari et al. (2012)	Variable properties + non-uniform Joule heating	Microtubes with viscous dissipation	EDL approximations	Newtonian	Yes	Complex thermal model but rheology simple.
Iverson / Broderick (electrothermal works)	Electrothermal modeling	Axial conduction + Joule heating	EDL sometimes thin-EDL assumed	Newtonian	Yes	Provides thermal methodology; not applied to viscoelastic fluids in these works.
Das & Chakraborty (2006)	Non-Newtonian + temperature	Analytical velocity + temperature	PB approximations	Power-law	Yes — temperature solved	Good multiphysics but restricted to power-law rheology.

2.2.7 Other relevant / foundational references (reviews, theory, specialized)

Table 2.7. Other relevant / foundational references (reviews, theory, specialized).

Prior work	Type	Notes / role in thesis
Squires & Quake; Schoch et al. (reviews)	Review articles	Provide microfluidics and electrokinetic background; used to motivate importance of surface forces.
Levich; Verwey & Overbeek; Levich (classics)	Foundational theory	Classical colloid & electrokinetics theory references.

Bazant & Squires (induced-charge electrokinetics)	Theory	Induced-charge electrokinetics conceptual extension.
Oliveira, Alves & Pinho (numerical methods review)	Numerical methods	Useful citations for viscoelastic numerical technique.

Table 2.8. Recent (Post-2021) Microchannel Studies & Comparison with Present Work

Title	**Authors**	**Year**	**Fluid / Model**	**Main Focus of Study**	**Gap Relative to Present Work**
Electro-osmotic flow of a Maxwell fluid induced by an alternating electric field	X. Yang et al.	2023	Maxwell viscoelastic	AC EOF in curved/rectangular microchannels	Linear viscoelastic (Maxwell), isothermal, no full PB, no streaming potential, no thermally developing Joule/viscous heating as in present sPTT model.
Start-Up Multilayer Electro-Osmotic Flow of Maxwell Fluids in Annular Microchannel with Slip	C. Valencia et al.	2023	Maxwell multilayer	Transient multilayer EOF with slip	Transient Maxwell only; lacks nonlinear PTT/sPTT elasticity, full PB at high ζ, and thermal development with Joule + viscous heating.
AC Electroosmotic Flow of Maxwell Fluid with Sinusoidal Roughness	L. Chang et al.	2023	Maxwell	AC EOF + geometric roughness	AC isothermal roughness study; no thermal coupling, no pressure-driven contribution, no sPTT or energy equation used in present work.
Analytical Electro-osmotic Flow of Two Immiscible Power-Law Fluids	S. Deng	2022	Power-law (two-layer)	Analytical immiscible layered EOF	Shear-thinning only; no viscoelasticity, no thermally developing flow, no streaming potential as present work includes.
Unsteady Two-layer Electroosmotic + Pressure-driven Flow with Slip-Dependent Zeta	S. Deng et al.	2024	Two-layer / power-law	Unsteady EOF+PD with slip	No sPTT viscoelasticity, no full PB coupling with Joule/viscous heating, no entropy/exergy treatment.
Dissipated electroosmotic EMHD hybrid nanofluid flow in cylindrical microchannel	M. Bilal et al.	2022	Hybrid nanofluid	EMHD + EOF + nanofluid thermals	Nanofluid effective viscosity; lacks viscoelastic PTT behaviour, no strong coupling of PB + Joule heating + streaming potential.
Electroosmotic flow & heat transfer of hybrid nanofluid in microchannel	P. Barnoon et al.	2023	Hybrid nanofluid	EOF heat transfer in nanofluid	Newtonian/effective model, lacks viscoelasticity, no coupled PB–PTT–thermal system.

Unsteady Electroosmotic Flow of Jeffrey Fluid in Circular Microchannel	M. Ren et al.	2022	Jeffreys (linear viscoelastic)	Analytical unsteady EOF solution	Jeffreys model simpler; no thermally developing Joule/viscous heating and no sPTT nonlinearity.
Exact Solutions for Electroosmotic Flow of Second-Grade Fluid	X. Yang et al.	2024	Second-grade	Exact analytical EOS of second-grade fluid	No sPTT elasticity (finite extensibility/shear-thinning), no thermal coupling, no streaming potential.
Electroosmotic mixing of viscoplastic fluids	S. Mehta et al.	2024	Viscoplastic / yield-stress	EOF mixing of yield-stress fluids	Viscoplastic focus; no full PB + sPTT + thermally developing analysis like present work.
Steady EOF two-fluid flow of viscoelastic Ellis fluid	H. Alyousef et al.	2023	Ellis viscoelastic	Two-fluid viscoelastic EOF analysis	Ellis rheology only; no Joule heating, no PB + streaming potential coupling, no mixed EOF–PD PTT modelling.
Particle equilibrium in microchannel Newtonian/power-law flows with an obstacle	D. Chen & J. Lin	2023	Newtonian & power-law	Particle migration in microflows	Not an electrokinetic or viscoelastic study; no coupled PB–PTT–thermal effects.
Heat & mass transfer of s-PTT nanofluid in electroosmotic microchannel	M. Kananipour	2024	sPTT nanofluid	Slip, nanoparticles, heat/mass transfer	sPTT included but no streaming potential, no mixed EOF–PD, no nonlinear PB with Joule/viscous heating and entropy analysis like present thesis.
FENE-P fluid: drag reduction & heat transfer	A. Ahmad et al.	2022	FENE-P viscoelastic	Drag reduction + heat transfer study	Thermal but no electrokinetics; no full PB, no EOF–PD coupling, and lacks sPTT thermoviscoelastic features.
Electroosmotic effect on two immiscible conducting & non-conducting fluids	R. Ponalagusamy et al.	2023	Two-phase miscible/immiscible	Electroosmotic flow in multiphase systems	Two-phase (conducting/non), but no sPTT, no coupled full-PB thermal development, no Joule/viscous dissipation or streaming potential.
On the similarities between the simplified Phan–Thien–Tanner model and the FENE-P model	Davoodi, A. et al.	2022	Rheology comparison study (s-PTT vs FENE-P)	Theoretical comparison of constitutive behavior of viscoelastic models; investigates when s-PTT behaves similarly to FENE-P	No electrokinetic microchannel flow; no EDL/PB physics, no thermal development, no streaming potential or Joule heating coupling; supports model selection but lacks full multiphysics framework developed in the present work

Numerical simulations for electro-osmotic flow of PTT fluids in a diverging microchannel	M. Trivedi	2022	PTT viscoelastic	Numerical EOF flow in diverging geometry; analyses elasticity effects	No thermally developing energy equation, no Joule/viscous heating, no streaming-potential or entropy/exergy coupling, no full nonlinear PB present work provides a combined mixed EOF-PD + thermal + electrokinetic multiphysics model
Flow-switching and mixing phenomena in electroosmotic flows of viscoelastic fluids	M. B. Khan et al.	2023	Viscoelastic (unspecified / generic)	Numerical + experimental study of flow switching and mixing under electro-elastic instabilities in a microchannel	Does not use the PTT or sPTT model; no thermally developing flow, no full PB-based EDL, no mixed EOF + PD + energy / entropy analysis as in your thesis.
Electrokinetic instabilities in Boger-fluid flows with conductivity gradients	T. L. Chen, M. K. Raihan, S. M. Tabarhoseini et al.	2025	Boger fluid (elastic, constant viscosity)	Experimental study of EKI (electrokinetic instability) in microchannel flows with conductivity gradients. (	Boger fluid has constant viscosity and no shear-thinning — different rheology than sPTT; also, this study does not couple with Joule/viscous heating, streaming-potential modeling, or non-linear PB as in your work.
Electrokinetic flow instabilities in shear-thinning fluids with conductivity gradients	T.-L. Chen et al.	2025	Shear-thinning (polymer)	Soft-matter experimental study of non-Newtonian EKI waves in microchannel with conductivity gradient, showing how shear-thinning lowers the threshold for instability. ()	Shear-thinning but not viscoelastic (no memory/elastic stress evolution like sPTT); also does not incorporate full PB at high ζ, nor thermal coupling / energy dissipation modeling of your thesis.

2.3 Short summary of key research gaps based on literature review

- Thermo-electro-osmotic studies are largely Newtonian, with viscoelastic fluids rarely examined under thermally developing conditions with Joule and viscous heating, limiting realistic prediction for high-field microfluidic applications.

- Most non-Newtonian studies use power-law models, which capture shear-dependent viscosity but cannot represent elastic memory or finite-extensibility effects. The s-PTT model is crucial because it accurately captures elastic stress growth and deformation behaviour in polymeric and bio-fluids, which simpler models cannot.

- Streaming-potential effects are well studied for Newtonian and power-law fluids, but seldom coupled with nonlinear viscoelastic evolution and electro-thermal energy equations under mixed EOF–PD flows—critical for flow stability and control.

- EDL modelling often uses simplified Debye–Hückel or thin-EDL assumptions, unsuitable at high ζ-potential or overlapping-EDL regimes; full nonlinear Poisson–Boltzmann solutions remain limited despite being essential for accurate electrokinetic prediction.

Bridging these gaps is vital for designing microfluidic systems such as lab-on-chip devices, biofluid transport channels, point-of-care platforms, micro-mixers, cooling micro channels, and drug-delivery systems where flow control and thermal management are critical. This work therefore develops a unified multiphysics framework combining sPTT viscoelasticity, full Poisson–Boltzmann electrostatics, mixed EOF–pressure-driven flow, streaming-potential effects, and Joule/viscous heating to accurately predict and optimize microfluidic performance.

Chapter 3. Electroosmotically mediated pressure driven flow of sPTT fluids in a microchannel

In this chapter, a comprehensive theoretical framework is developed to analyze the hydrodynamic behavior of viscoelastic fluids, modeled using the simplified Phan-Thien–Tanner (sPTT) constitutive relation, under the combined influence of electroosmotic and pressure-driven transport within microchannel. The formulation incorporates the electric double layer (EDL) potential distribution, electrohydrodynamic body forces, and the nonlinear rheological behavior of the sPTT fluid. A coupled set of governing equations is derived and analyzed to capture the velocity field, stress distribution, and shear-dependent viscosity. The resulting framework enables a detailed assessment of key transport characteristics under varying electrokinetic and rheological conditions.

3.1 Problem Formulation

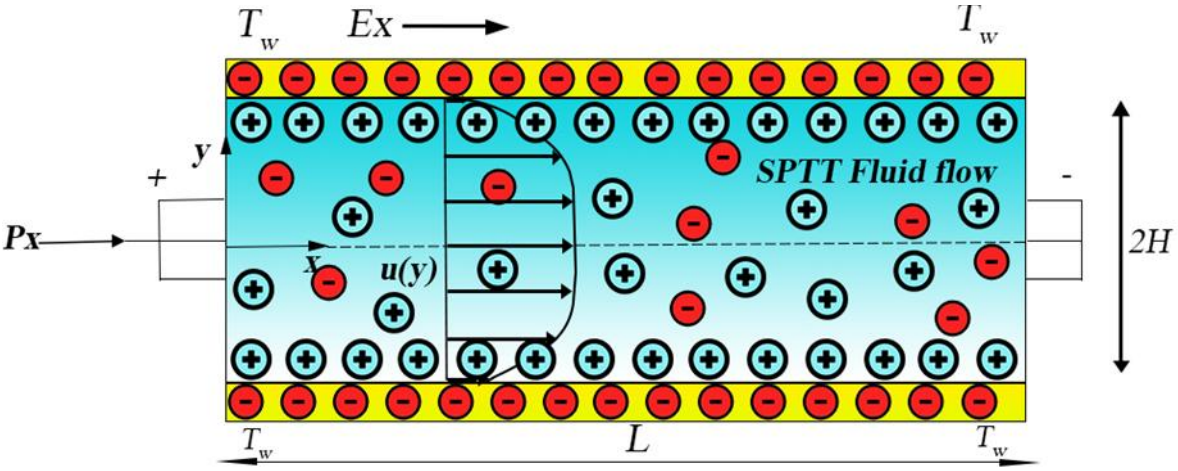

Fig. 3.1. The schematic diagram represents a physical model for the combined electroosmotic and pressure-driven flow of viscoelastic fluid through a constant wall temperature microchannel

We consider the combined electroosmotic and pressure-driven flow of the viscoelastic fluid in a slit-type parallel plate microchannel, as schematically shown in Fig. 3.1. The coordinate axes are so chosen that the origin is placed at the centerline of the channel. In contrast, the x and y coordinates run along the streamwise and transverse directions of the flow, respectively. The length of the microchannel is L, and the thickness is 2H. Note that the width W of the channel is considered to be very large compared to its thickness, 2H, such that any property variations along the width direction are neglected, and flow

is considered two-dimensional. Furthermore, we consider the flow steady, laminar, hydrodynamically fully developed incompressible. The viscoelastic behavior of the fluid is described by the simplified Phan-Than-Tanner (sPTT) model. The ionic equilibrium is assumed to be not affected by the axial velocity of the electrolyte solution, by which the Boltzmann distribution for the ionic concentration in the present flow system becomes valid. Besides, we consider the channel walls to prevail in a uniform temperature.

The thermophysical properties of the fluid are assumed to be temperature independent with a uniform dielectric constant ε. The flow is actuated by the combined effect of constant axial pressure gradient and axial electric field strength. We assume non-overlapping EDL with a constant wall zeta potential distribution at the channel walls.

3.2 EDL potential distribution

The electrostatic potential distribution owing to the development of the EDL closer to the charged surface, obeys the Poisson equation and may be written as[10]

$$\nabla^2\psi = -\frac{\rho_e}{\varepsilon_p} \tag{3.1}$$

For the present situation of fully developed, steady, unidirectional flow with a non-overlapping thin EDL's, Eq. (3.1) may be written in the following form

$$\frac{d^2\psi}{dy^2} = -\frac{\rho_e}{\varepsilon_p} \tag{3.2}$$

Here, the net electric charge density for constant permittivity fluid with additional considerations of point charges of ionic species, can be obtained using the Boltzmann distribution as

$$\rho_e = -2n_0\, eZ sinh\left(\frac{eZ}{k_B T}\psi\right) \tag{3.3}$$

Here, n_0 is bulk ionic concentration ($n_0=C_A N_A$, C_A is the molar concentrations of ions and N_A= 6.023×10^{23} Avogadro number), e is the elementary electric charge (1.602×10^{-19} C), $k_B$is Boltzmann constant (1.381 × 10^{-23} m^{2}kg^{-2}K^{-1}). Z is the valance of ionic species, and T is the absolute temperature. For constant voltage gradient in the x-direction, by combining equations (3.2) and (3.3), we obtain

$$\frac{d^2\psi}{dy^2} = \frac{2n_0\ eZ}{\varepsilon\varepsilon_o}\sinh\left(\frac{eZ}{k_BT}\psi\right) \tag{3.4}$$

Equation (3.4) is non-linear, second order one dimensional Poisson Boltzmann equation and is subjected to the following sets of boundary conditions: $(d\psi/dy)_{y=0} = 0$ and $(d\psi/dy)_{y=H} = \zeta$. On integration of Eq. (3.4), the exact closed-form solution for the EDL potential distribution is obtained as,

$$\psi = \frac{4k_BT}{eZ}\tanh^{-1}\left[\tanh\left(\frac{eZ}{k_BT}\right)\exp(ky - kH)\right] \tag{3.5}$$

where $k = (2n_0e^2z^2/\varepsilon_p k_B T)^{1/2}$ is the inverse of Debye length λ_D, which is known as the characteristics of EDL thickness ($k^{-1} = \lambda_D$). We further make Eq. (3.5) dimensionless with the following dimensionless variables $\tilde{\zeta} = ez\zeta/k_BT$, $\tilde{k} = kH$, $\tilde{y} = y/H$, $\tilde{\Psi} = ez\Psi/k_BT$, to obtain the dimensionless form the EDL potential distribution

$$\tilde{\psi} = 4\tanh^{-1}\left(\tanh\left(\frac{\tilde{\zeta}}{4}\right)\exp\left(\tilde{k}\tilde{y} - \tilde{k}\right)\right) \tag{3.6}$$

Alternatively, one may obtain the dimensionless EDL potential distribution for lower values of zeta potential $\left(|\zeta| < 26\,\text{mV}\right)$ by invoking the Debye-Huckel linearization to obtain,

$$\Psi = \zeta\cosh\left(k\,y\right)\Big/\cosh\left(k\right) \tag{3.7}$$

3.3 Electrohydrodynamic fluidic transport equation

The incompressible continuity and momentum equations constitute the governing equations for fluid flow. For the fully developed flow of viscoelastic fluid, the governing Cauchy's momentum equations with the EOF body force term can be written as,

$$\nabla.u = 0 \tag{3.8a}$$

$$-\nabla P + \nabla.\tau + \rho_e E = 0 \tag{3.8b}$$

Here, $\boldsymbol{u}$ is the velocity vector, p is the pressure,τ is the polymeric extra-stress tensor contribution, and $\rho_e E$ representing the body force per unit volume due to applied electric field.

Coupling of governing equation of velocity with constitutive equation of sPTT

We adopt the rheological behavior of the viscoelastic fluid to follow the PTT model. Therefore, by adopting, sPTT constitutive relationship, the polymeric extra-stress tensor τ can be as expressed as

$$f(\tau_{kk})\tau + \lambda \overset{\nabla\nabla}{\tau} = 2\eta D \tag{3.9}$$

Where $D = (\nabla u + \nabla u^T)/2$the rate of deformation tensors, η is is polymer viscosity coefficient. Here, $\overset{\nabla\nabla}{\tau}$ represent the upper convected derivative of the stress tensor, τ , and λ is the relaxation time of the viscoelastic fluid. The expression for $\overset{\nabla\nabla}{\tau}$ is given by

$$\overset{\nabla\nabla}{\tau} = \frac{D\tau}{Dt} - \nabla u^T - \tau \,.\nabla u \tag{3.10}$$

For the sPTT model, the expression for the stress coefficient function $f(\tau_{kk})$, is defined as

$$f(\tau_{kk}) = 1 + \frac{\epsilon\lambda}{\eta}\tau_{kk} \tag{3.11}$$

Where ϵ is the elongation viscosity and $\tilde{\tau}_{kk}$ is the trace of extra stress tensor, given by, f$\tau_{kk} = \tau_{xx} + \tau_{yy} + \tau_{zz}$. If $f(\tilde{\tau}_{kk})$ =1, when $\epsilon = 0$, for dilute polymeric solutions, will result into Johnson-Segalman constitutive equation.[48] By invoking the assumptions of a fully developed, two dimensional ($\tilde{\tau}_{zz}$= 0), and unidirectional flow $(u(y), 0, 0)$, Eq. (3.9) becomes

$$f\big(\tau_{xx} + \tau_{yy}\big)\tau_{xx} = 2\lambda\left(\frac{du}{dy}\right)\tau_{xy} \tag{3.12a}$$

$$f\big(\tau_{xx} + \tau_{yy}\big)\tau_{yy} = 0 \tag{3.12b}$$

$$f\big(\tau_{xx} + \tau_{yy}\big)\tau_{xy} = \eta\frac{du}{dy} + \lambda\frac{du}{dy}\tau_{yy} \tag{3.12c}$$

We write the nontrivial solution of Eq. (3.12b) asτ_{yy}=0, and therefore $\tau_{kk} = \tau_{xx}$. Now by dividing equation (3.12c) by (3.12a), we obtain. $\tau_{xx} = (2\lambda/\eta)\big(\tau_{xy}\big)^2$ .We carry out few simplification with Eqs. (3.12) to finally obtain following relationship of the shear stress as

$$\tau_{xy} + \frac{2\epsilon\lambda^2}{\eta^2}\big(\tau_{xy}\big)^3 = \eta\frac{du}{dy} \tag{3.13}$$

Hence, under fully developed conditions, the modified Cauchy's momentum equation (Eq. 3.8) takes the following form

$$\frac{d\tau_{xy}}{dy} = p_x - \varepsilon\, E_x \frac{d^2\psi}{dy^2} \tag{3.14}$$

We integrate Eq. (3.14) and apply the boundary condition$\left(\psi,\ \tau_{xy}\right)_{y=0} = 0$, to obtain

$$\tau_{xy} = P_x y + \varepsilon_{\mathrm{p}} E_x \frac{d\psi}{dy} \tag{3.15}$$

On substituting Eq. (3.15) in Eq. (3.13), we obtain an explicit equation for the velocity gradient in the microchannel as

$$\frac{du}{dy} = \frac{1}{\eta}\left(P_x y + \varepsilon_{\mathrm{p}} E_x \frac{d\psi}{dy}\right) + \frac{2 \in \lambda^2}{\eta^2}\left(P_x y + \varepsilon_{\mathrm{p}} E_x \frac{d\psi}{dy}\right)^3 \tag{3.16}$$

Going further, we make Eq. (3.16) dimensionless by substituting the following dimensionless scales: the nondimensional velocity $\tilde{u} = u/\tilde{u}_{HS}$, where $\tilde{u}_{HS}$ is the Helmholtz-Smoluchowski velocity scale, to obtain,

$$\frac{d\tilde{u}}{d\tilde{y}} = \left[\left(\Lambda\tilde{y}\right) - \frac{1}{\tilde{\zeta}} \times \frac{4p\tilde{k}e^{(\tilde{y}-1)\tilde{k}}}{1-p^2e^{2\left(\tilde{k}\tilde{y}-\tilde{k}\right)}}\right] + \frac{2 \cong \tilde{W}i_k^2}{\tilde{k}^2}\left[\left(\Lambda\tilde{y}\right) - \frac{1}{\tilde{\zeta}} \times \frac{4p\tilde{k}e^{(\tilde{y}-1)\tilde{k}}}{1-p^2e^{2\left(\tilde{k}\tilde{y}-\tilde{k}\right)}}\right]^3 \tag{3.17}$$

where $\tilde{W}_{ik} = \tilde{\lambda}\tilde{k}\,\tilde{u}_{hs}$ is the Weissenberg number based on reference velocity scale $\tilde{u}_{HS}$, and $\Lambda = (-H^2/\varepsilon_p\,\tilde{\zeta})(P_x/E_x)$ is the ratio of the pressure to electroosmotic forces. We now integrate Eq. (3.17) with the no-slip boundary conditions at the channel walls $\left((\tilde{u})_{\tilde{y}=\pm1} = 0\right)$ and symmetry boundary conditions ate the centreline of the channel, to obtain the closed form analytical solution for the velocity distribution across the microchannel as

$$\tilde{u}(\tilde{y}) = -\frac{24\,\tilde{\in}\,\mathrm{W}\tilde{\mathrm{i}}_k^2\Lambda^2}{\tilde{\mathrm{k}}^4\tilde{\zeta}}\Big[\,\text{-}\mathrm{Li}_3(p)+\mathrm{Li}_3(\text{-}p)\,\text{-}\mathrm{Li}_3(\text{-}pe^{\tilde{k}(\tilde{y}-1)})+\mathrm{Li}_3(pe^{\tilde{k}(\tilde{y}-1)})\,\Big]$$

$$+\frac{24\,\tilde{\in}\,\mathrm{W}\tilde{\mathrm{i}}_k^2\Lambda^2}{\tilde{\mathrm{k}}^3\tilde{\zeta}}\Big[\,\text{-}\mathrm{Li}_2(p)+\mathrm{Li}_2(\text{-}p)\,\text{-}\mathrm{yLi}_2p(\text{-}e^{\tilde{k}(\tilde{y}-1)})+\tilde{\mathrm{y}}\mathrm{Li}_2p(e^{\tilde{k}(\tilde{y}-1)})\,\Big]$$

$$+\frac{24\,\tilde{\in}\,\tilde{W}i_k^2\Lambda}{\tilde{k}^2\tilde{\zeta}^2}\left[\ln\left(\frac{e^{2\tilde{k}}\,\text{-}\,p^2e^{2\tilde{k}\tilde{y}}}{e^{2\tilde{k}}(1\,\text{-}\,p^2)}\right)+\frac{\tilde{\zeta}\Lambda}{2}\ln\left[\frac{1+p}{1-p}\right]+\frac{\tilde{\zeta}\Lambda\tilde{y}^{\,2}}{2}\ln\left[\frac{1-pe^{\tilde{k}(\tilde{y}-1)}}{1+pe^{\tilde{k}(\tilde{y}-1)}}\right]\right]$$

$$+\frac{16\,\tilde{\in}\,\tilde{W}i_k^2p\Lambda}{\tilde{\zeta}^2}\left[\frac{3}{\tilde{k}p(p^2-1)}+\frac{3ye^{2\tilde{k}}}{\tilde{k}p(e^{2\tilde{k}}\,\text{-}\,p^2e^{2\tilde{k}\tilde{y}})}+\frac{(p^2+1)}{\Lambda\tilde{\zeta}(p^2-1)^2}-\frac{2e^{\tilde{k}(3+y)}}{\Lambda\tilde{\zeta}(e^{2\tilde{k}}\,\text{-}\,p^2e^{2\tilde{k}\tilde{y}})^2}+\frac{e^{(\tilde{k}+\tilde{k}\tilde{y})}}{\Lambda\tilde{\zeta}(e^{2\tilde{k}}\,\text{-}\,p^2e^{2\tilde{k}\tilde{y}})}\right]$$

$$+\frac{16\,\tilde{\in}\,\tilde{W}i_k^2}{\tilde{\zeta}^3}\Big[\tanh^{-1}[pe^{\tilde{k}(\tilde{y}-1)}]-\tanh^{-1}[p]\Big]$$

$$+\frac{48\,\tilde{\in}\,W\tilde{\mathrm{i}}_k^2\Lambda}{\tilde{k}\tilde{\zeta}^2}(1-\tilde{y})+\frac{4}{\tilde{\zeta}}\Big[\tanh^{-1}[p]-\tanh^{-1}[pe^{\tilde{k}(\tilde{y}-1)}]\Big]$$

$$+\frac{\tilde{\in}\,\tilde{W}i_k^2\Lambda^3}{2\tilde{k}^2}\left(\tilde{y}^4-1\right)+\frac{\Lambda}{2}(\tilde{y}^2-1)$$

(3.18)

Where $p=\tanh\left(\tilde{\zeta}/4\right)$, and $Li_n(\alpha)$ is the Jonquiere function or the polylogarithm of order 'n' and is the argument defined by power series $Li_n(\alpha)=\sum_{k=1}^{\infty}\frac{\alpha^n}{k^n}$In contrast, we obtain velocity profile by considering Debye-Huckel linearization approximation with the dimensionless EDL potential distribution as given in Eq. (3.7), to obtain

$$\tilde{u}(\tilde{y})=\frac{3}{8\tilde{k}^4\cosh\left[\tilde{k}\right]^2}\begin{pmatrix}\tilde{k}^4\left(-2+\Lambda-\tilde{y}^2\Lambda+4\,\tilde{\in}\,\tilde{W}i_k^2\left(1+\left(-1+\tilde{y}^2\right)\Lambda\right)\right)\\+\,\tilde{\in}\,\tilde{W}i_k^2\left(-24\Lambda+\tilde{k}^2\left(-1-12\Lambda-\left(-1+\tilde{y}^4\right)\Gamma^2\right)\right)\end{pmatrix}$$

$$+\frac{3\cosh\left[3\tilde{k}\right]}{8\tilde{k}^4\cosh\left[\tilde{k}\right]^3}\left(\tilde{k}^4\left(6+4\,\tilde{\in}\,\tilde{W}i_k^2+3\left(-1+\tilde{y}^2\right)\Lambda\right)+3\,\tilde{\in}\,\tilde{W}i_k^2\Lambda\left(24\Lambda+\tilde{k}^2\left(3+12\Lambda+\left(\tilde{y}^4-1\right)\Lambda^2\right)\right)\right)$$

$$+\frac{3}{2\tilde{k}^4\cosh\left[\tilde{k}\right]^3}\left(\tilde{\in}\,\tilde{W}i_k^2\tilde{k}^4\cosh\left[\tilde{k}y\right]^3+3\left(\tilde{k}^4+6\,\tilde{\in}\,\tilde{W}i_k^2\Lambda^2\left(2+\tilde{k}^2y^2\right)\right)\sinh\left[2\tilde{k}\right]\sinh\left[\tilde{k}\tilde{y}\right]\right)$$

$$+\frac{9\cosh\left[\tilde{k}\tilde{y}\right]}{2\tilde{k}^4\cosh\left[\tilde{k}\right]^3}\left(\tilde{k}^4-\tilde{\in}\,\tilde{W}i_k^2(3(\tilde{k}^4+2\Lambda^2\left(2+\tilde{k}^2\tilde{y}^2\right)+\tilde{k}^4\sinh\left[\tilde{k}\tilde{y}\right]^2)\right)-\frac{27\,\tilde{\in}\,\tilde{W}i_k^2\Lambda}{4\tilde{k}^2\cosh\left[\tilde{k}\right]^2}\cosh\left[2\tilde{k}\tilde{y}\right]$$

$$+\frac{27\,\tilde{\in}\,\tilde{W}i_k^2}{2\tilde{k}^4\cosh\left[\tilde{k}\right]^2}\left(-2\tilde{k}\Lambda^2+\tilde{k}\Lambda\left(\tilde{k}^2+6\Lambda\right)+\tilde{k}\Lambda\left(\tilde{k}^2+4\Lambda\right)\cosh\left[2\tilde{k}\right]\right)\tanh\left[\tilde{k}\right]$$

$$+\frac{54\,\tilde{\in}\,\tilde{W}i_k^2\tilde{y}\Lambda^2}{\tilde{k}^3\cosh\left[\tilde{k}\right]^3}\left(\sinh\left[\tilde{k}\tilde{y}\right]+\cosh\left[2\tilde{k}\right]\sinh\left[\tilde{y}\tilde{k}\right]\right)+\frac{27\,\tilde{\in}\,\tilde{W}i_k^2\tilde{y}\Lambda}{2\tilde{k}\cosh\left[\tilde{k}\right]^2}\sinh\left[2\tilde{k}\tilde{y}\right]$$

(3.19)

The dimensionless volume flow rate per unit width is evaluated by integrating the velocity distribution Eq. (3.17),

$$Q_f = \frac{Q}{2Hwu_{HS}} = \int_0^1 \tilde{u}(y)dy$$

$$= \frac{72\,\tilde{\in}\,\tilde{\mathrm{Wi}}_k^2\Lambda^2}{\tilde{k}^5\tilde{\zeta}}\left[\mathrm{Li}_4(\text{-}p) - \mathrm{Li}_4(p) + \mathrm{Li}_4(pe^{-\tilde{k}})\text{-}\mathrm{Li}_4(-e^{-\tilde{k}}p)\right] + \frac{72\,\tilde{\in}\,\mathrm{Wi}_k^2\Lambda^2}{\tilde{k}^4\tilde{\zeta}}\left[\mathrm{Li}_3(p) - \mathrm{Li}_3(\text{-}p)\right]$$
$$+ \frac{16\,\tilde{\in}\,\tilde{\mathrm{Wi}}_k^2 p}{\tilde{k}\tilde{\zeta}^2}\left[\frac{e^{2\tilde{k}}}{e^{2\tilde{k}} - p^2} + \frac{1}{p^2 - 1} + \frac{\tilde{k}(p^2+1)}{(p^2-1)^2}\right]$$
$$+ \frac{24\,\tilde{\in}\,\tilde{\mathrm{Wi}}_k^2\Lambda}{\tilde{k}^2\tilde{\zeta}^2}\left[\ln\frac{1-p}{1+p} - \ln\frac{p^2-1}{p^2} - \frac{1}{\tilde{k}}\ln(e^{\tilde{k}})^2 + \frac{2\Lambda}{\tilde{\zeta}}\ln\left(\frac{1+p}{1-p}\right)\right]$$
$$+ \frac{24\,\tilde{\in}\,\tilde{\mathrm{Wi}}_k^2\Lambda}{\tilde{k}^3\tilde{\zeta}^2}\left[\ln\frac{e^{\tilde{k}}(1+p)-p}{e^{\tilde{k}}(1+p)-e^{-\tilde{k}}p} + \ln\frac{e^{\tilde{k}}(1-p)-p}{e^{\tilde{k}}(1-p)+e^{-k}p}\right]$$
$$+ \frac{24\,\tilde{\in}\,\tilde{\mathrm{Wi}}_k^2\Lambda}{\tilde{k}^3\tilde{\zeta}^2}\left\{\mathrm{Li}_2(1\text{-}p) - \mathrm{Li}_2(1-e^{-\tilde{k}}p) + \frac{3\Lambda\tilde{\zeta}}{2}\left[\mathrm{Li}_2(\text{-}p) - \mathrm{Li}_2(p)\right]\right\}$$
$$+ \frac{1}{\tilde{k}\tilde{\zeta}}\left\{\left[\mathrm{Li}_2(\text{-}p) - \mathrm{Li}_2(p) + \mathrm{Li}_2(pe^{-\tilde{k}})\text{-}\mathrm{Li}_2(-e^{-\tilde{k}}p)\right] + \frac{1}{\tilde{\zeta}^2}\left[\mathrm{Li}_2(\text{-}p) - \mathrm{Li}_2(p) + \mathrm{Li}_2(-pe^{-\tilde{k}})\text{-}\mathrm{Li}_2(e^{-\tilde{k}}p)\right]\right\}$$
$$+ \frac{2}{\tilde{\zeta}}\left\{\ln\left(\frac{1+p}{1-p}\right) + \frac{4\,\tilde{\in}\,\mathrm{Wi}_k^2}{\tilde{\zeta}^2}\ln\left(\frac{1-p}{1+p}\right)\right\} - \Lambda\left[\frac{2\,\tilde{\in}\,\mathrm{Wi}_k^2\Lambda^2}{5} + \frac{1}{3}\right]$$

(3.20)

We integrate the closed-form expression for the velocity distribution as given by Eq. (3.19) to get the corresponding expression for the dimensionless volume flow rate under Debye-Huckel linearization approximation as

$$\tilde{Q}_f = \frac{1}{60\tilde{k}^4 \cosh\left[\tilde{k}\right]^2}\begin{pmatrix} \tilde{\in} Wi_k^{\tilde{2}}\Lambda(720\Lambda + \left(60(1-\tilde{y}) + (1-\tilde{y}^5)\Lambda\right) + 5\tilde{k}^4\left(\tilde{y}-1\right)\begin{pmatrix} 20\,\tilde{\in} Wi_k^{\tilde{2}} - \left(\tilde{y}^2+\tilde{y}-2\right)\Lambda \\ +6\,\tilde{\in} Wi_k^{\tilde{2}}\left(\tilde{y}^2+\tilde{y}-2\right)\Lambda - 6 \end{pmatrix} \\ +3\tilde{k}^2\Lambda\left(5\,\tilde{\in} Wi_k^{\tilde{2}}\Lambda^2\left(\tilde{y}-1\right)\right) \end{pmatrix}$$

$$+\frac{1}{180\tilde{k}^5\cosh\left[\tilde{k}\right]^2}\left[\sinh\left[2\tilde{k}\right] - \sinh\left[2\tilde{k}\tilde{y}\right] - 135\,\tilde{\in} Wi_k^{\tilde{2}}\tilde{k}^2\Lambda\left(\tilde{k}\tilde{y}\cosh\left[2\tilde{k}\tilde{y}\right]\right)\right]$$

$$+\frac{1}{36\tilde{k}^5\cosh\left[\tilde{k}\right]^3}\begin{pmatrix} \tilde{\in} Wi_k^{\tilde{2}}\tilde{k}^2\left(108\left(\tilde{y}-1\right)\Lambda^2 + \tilde{k}^2\left(2+27\left(\tilde{y}-1\right)\Lambda\right)\right)\sinh\left[3\tilde{k}\right] \\ +2\left(\left(9-26\,\tilde{\in} Wi_k^{\tilde{2}}\right)k^4 + \tilde{\in} Wi_k^{\tilde{2}}\left(324\Lambda^2 + 54\tilde{k}^2\tilde{y}^2\Lambda^2 + 2\tilde{k}^4\cosh\left[2\tilde{k}\tilde{y}\right]\right)\right)\sinh\left[\tilde{k}\tilde{y}\right] \end{pmatrix}$$

$$+\frac{1}{4\tilde{k}^5\cosh\left[\tilde{k}\right]^2}\left(\tilde{k}^4\left(-2+3\,\tilde{\in} Wi_k^{\tilde{2}}\left(2+\left(\tilde{y}-1\right)\Lambda\right)\right) - 12\,\tilde{\in} Wi_k^{\tilde{2}}\Lambda^2\left(\tilde{k}^2\left(\tilde{y}-1\right) - \tilde{k}^2\left(2\tilde{y}-3\right)+6\right)\tanh\left[\tilde{k}\right]\right.$$

$$-\frac{\cosh\left[2\tilde{k}\right]}{60\tilde{k}^5\cosh\left[\tilde{k}\right]^2}\begin{bmatrix} 360\,\tilde{\in} Wi_k^{\tilde{2}}\tilde{k}\left(\tilde{y}-3\right)\Lambda^2 5\tilde{k}^5\left(4\,\tilde{\in} Wi_k^{\tilde{2}}\left(\tilde{y}-1\right)+6\tilde{y}+\Lambda(\tilde{y}^3-3\tilde{y}+3)-6\right) \\ +3\tilde{k}^3\Lambda\left(-5\,\tilde{\in} Wi_k^{\tilde{2}}\Lambda^2\left(\tilde{y}-1\right)+\tilde{\in} Wi_k^{\tilde{2}}\left(-30+15\tilde{y}-60\Lambda(y+1)-\left(y^5+1\right)\Lambda^2\right)\right) \end{bmatrix}$$

$$-\frac{\cosh\left[2\tilde{k}\right]}{60\tilde{k}^5\cosh\left[\tilde{k}\right]^2}\left[30\begin{pmatrix} 24\,\tilde{\in} Wi_k^{\tilde{2}}\tilde{k}y\Lambda^2\cosh\left[\tilde{k}\tilde{y}\right]sech\left[\tilde{k}\right] \\ -\left(\tilde{k}^4+36\,\tilde{\in} Wi_k^{\tilde{2}}\Lambda^2+6\,\tilde{\in} Wi_k^{\tilde{2}}\tilde{k}^2\tilde{y}^2\Lambda^2\right)sech\left[\tilde{k}\right]\sinh\left[\tilde{k}\tilde{y}\right] \\ +\left(\tilde{k}^4+36\,\tilde{\in} Wi_k^{\tilde{2}}\Lambda^2+6\,\tilde{\in} Wi_k^{\tilde{2}}\tilde{k}^2\Lambda^2\right)\tanh\left[\tilde{k}\right] \end{pmatrix}\right] \tag{3.21}$$

We employ the constitutive relationships expressed in Eq. (3.12) and obtain the expressions for the polymeric stress distribution. We can write the interrelationship between normal and shear stress as

$$\tau_{xy}^2 = \frac{\eta}{2\lambda}\tau_{xx} \tag{3.22}$$

We now substitute the Eq. (3.15) in Eq. (3.21) to obtain the following expressions for dimensionless normal and shear stress components

$$\tilde{\tau}_{xx} = \frac{\tau_{xx}}{\eta\tilde{k}u_{hs}} = \frac{2\tilde{W}i_k^2}{\tilde{k}^2}\left[\Lambda.\tilde{y} - \left(\frac{1}{\tilde{\zeta}}\right)\left\{\frac{4p\tilde{k}\,\tilde{\in}^{(\tilde{y}-1)\tilde{k}}}{1-p^2\,\tilde{\in}^{2(\tilde{y}-1)\tilde{k}}}\right\}\right]^2 \tag{3.23}$$

$$\tilde{\tau}_{xy} = \left(\Lambda.\tilde{y}\right) - \frac{1}{\tilde{\zeta}}\times\frac{4p\tilde{k}\,\tilde{\in}^{(\tilde{y}-1)\tilde{k}}}{1-p^2\,\tilde{\in}^{2(\tilde{y}-1)\tilde{k}}} \tag{3.24}$$

Furthermore, the non-dimensional form shear rate may be expressed as

$$\dot{\gamma} = \frac{\tilde{x}}{-u_{hs}/H} = \left[(\Lambda.\tilde{y}) - \frac{1}{\tilde{\zeta}} \times \frac{4p\tilde{k}\ \tilde{\in}^{(\tilde{y}-1)\tilde{k}}}{1-p^2\ \tilde{\in}^{2(\tilde{y}-1)\tilde{k}}} \right] + \left[1 + \frac{2\tilde{\in}\tilde{W}i_k^2}{\tilde{k}^2} \left((\Lambda.\tilde{y}) - \frac{1}{\tilde{\zeta}} \times \frac{4p\tilde{k}\ \tilde{\in}^{(\tilde{y}-1)\tilde{k}}}{1-p^2\ \tilde{\in}^{2(\tilde{y}-1)\tilde{k}}} \right)^2 \right] \tag{3.25}$$

Finally, the non-dimensional shear viscosity profile is given by

$$\tilde{\mu} = \frac{\tilde{\tau}_{xy}}{\dot{\gamma}} \left[1 + \frac{2\tilde{\in}\tilde{W}i_k^2}{\tilde{k}^2} \left((\Lambda.\tilde{y}) - \frac{1}{\tilde{\zeta}} \times \frac{4p\tilde{k}\ \tilde{\in}^{(\tilde{y}-1)\tilde{k}}}{1-p^2\ \tilde{\in}^{2(\tilde{y}-1)\tilde{k}}} \right)^2 \right]^{-1} \tag{3.26}$$

The expression for the transverse averaged shear viscosity may be defined as

$$\tilde{\mu}_{av} = \int_0^1 \tilde{\mu} d\tilde{y} \tag{3.27}$$

Note that for the Newtonian fluid, $\tilde{\epsilon}\widetilde{W}\imath_{\mathrm{k}}^2 = 0$ and hence, $\tilde{\mu}_{av} = \tilde{\mu}$.

It is important to mention here that normal stresses will depend directly on $\tilde{\epsilon}\widetilde{W}\imath_{\mathrm{k}}^2$ and inversely on some power, as shown in the equation (3.23). $\tilde{\epsilon}\widetilde{W}\imath_{\mathrm{k}}^2$, but shear stress will be solely determined by $\tilde{\epsilon}$. The dependence on $\widetilde{W}\imath_{\mathrm{k}}^2$ is purely a normal stress effect, but the dependence on $\tilde{\epsilon}\widetilde{W}\imath_{\mathrm{k}}^2$ combines a normal stress effect with the elongational parameter $\tilde{\epsilon}$ and this combination causes the viscosity function to shear. When referring to the impact of shear-thinning the term $\tilde{\epsilon}\widetilde{W}\imath_{\mathrm{k}}^2$, will be used in this context from now on in the study.

3.4 Results and Discussion

In this section, we discuss the important results from our work in terms of non-dimensional parameters. At first, we have validated the solutions for the velocity across the microchannel with the corresponding data available in the literature. In an effort to do so, in Fig.3.2, we plot the variation of dimensionless velocity $(\tilde{u})$ distribution across the microchannel for pure electroosmotic flow $(\Lambda = 0)$ of PTT fluids and compare the present analytical solution with the analytical results reported by Afonso et.al[53]. The other pertinent parameters are given in the caption. We can see from Fig. 3.2 that our results are in good agreement with the literature. We consider the non-Newtonian fluid as a typical biofluidic sample, whose thermophysical properties at a reference temperature $T = 300K$ are: density, $\rho = 10^3 kg\ m^{-3}$,

permittivity $\varepsilon_p = 701.24 \times 10^{-12} C^2/J.m$, fluid viscosity $\eta = 10^{-3} - 10^{-2} Pa.s$.For a microchannel, the length and width generally varies of the order of $L \approx W \approx O(10^3 \mu m)$, whereas the channel height $H \approx O(10\,\mu m)$, and hence, the relevant dimensionless parameters fall in the range of $\tilde{k} = 10 - 40$, and $\tilde{\zeta} = 1 - 10$. For thermally developing flows, we have considered,$Pe = 0.1 - 10$, $Br = 0.01 - 100$, $S_p = 1 - 100$ and presented the analysis in the subsequent section.

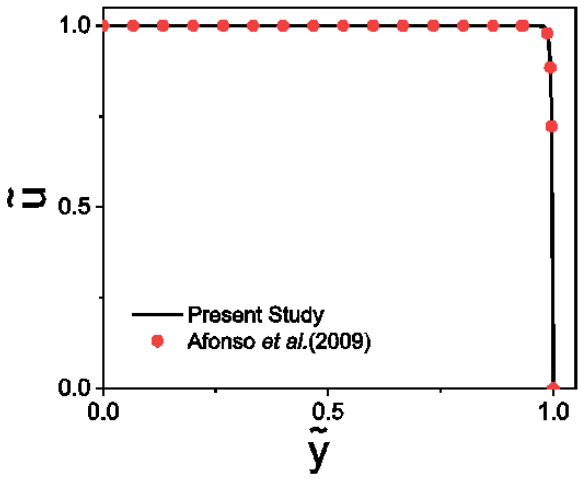

Fig. 3.2. Variation of dimensionless velocity distribution across the channel width for pure electroosmotic flows of PTT fluids at $\tilde{\varepsilon}\widetilde{W}\iota_k^2$=1 and $\tilde{\zeta}$=1. A comparison has been made between the present analytical solution and theoretical result reported in Afonso et al[53].

3.4.1 Velocity distribution and volumetric flow rate

We first focus on studying the nature of fully developed electrohydrodynamic velocity distribution for a specified range of the aforementioned parameters. Fig. 3.3(a) depicts the variation in the nondimensional velocity along the transverse cross-section of the microchannel. The other related value is mentioned in the caption. Here we study the effect of different values of EDL thickness $\tilde{k}$ on the velocity distribution for the PTT fluid. We observe that by increasing the EDL thicknesses, the accumulation of the electroosmotic forces within the EDL provides a smaller electrostatic pull of the counter-ion near the wall. That, in turn, reduces the flow velocity. Fig. 3.3(b) shows the variation of velocity distribution for various ratios of a pressure gradient to the electroosmotic forces. The pertinent values of other parameter are displayed in caption. The velocity profile is "plug-like" for $\Lambda = 0$ and thus represents pure electroosmotic flow.

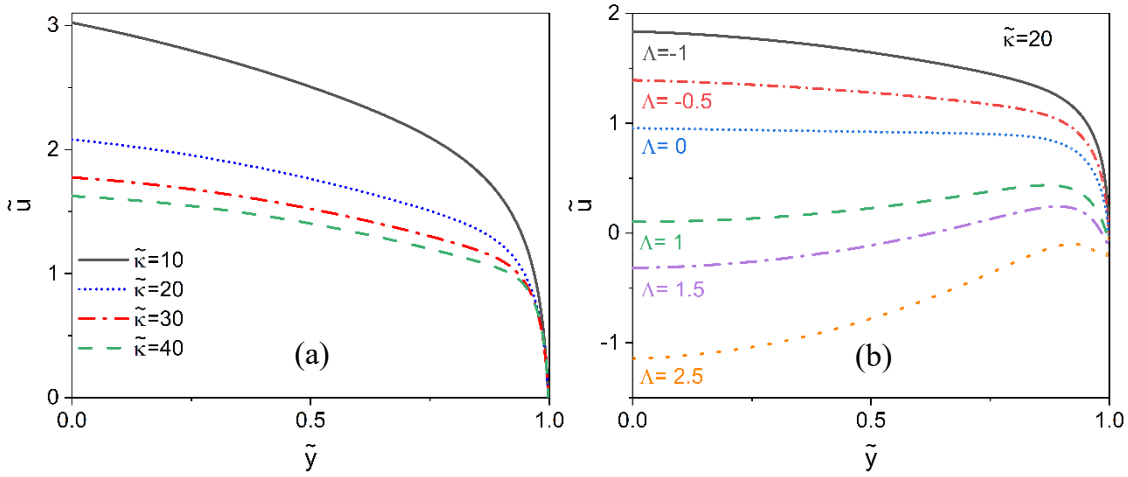

Fig. 3.3. Variation in dimensionless velocity profile across the transverse cross section of the microchannel for (a) varying EDL thickness and at $\tilde{\varepsilon}\widetilde{W}\iota_{\mathrm{k}}^{2}$ = 2, $\tilde{\zeta}$=5, Λ = -1. (b) Variation of $\tilde{u}$ with $\tilde{y}$ for favorable to adverse pressure gradients at $\tilde{\varepsilon}\widetilde{W}\iota_{\mathrm{k}}^{2}$ = 1, $\tilde{\zeta}$=5, $\tilde{k}$=20.

Favourable ($\Lambda < 0$) and adverse pressure gradient ($\Lambda > 0$) conditions indicate that the pressure contribution on the flow is more dominant than the electroosmotic contributions for altering the flow velocity. This results in a conventional parabolic velocity profile representing the Poiseuille flow. Favourable pressure gradient favours the electroosmotic flow, and therefore there is an augmentation in the magnitude of the flow velocity. In contrast, the adverse pressure gradient opposes the electroosmotic flow contribution, resulting in a gradual reduction in the flow rate

The influence of complex rheology of the PTT fluid can be accounted for by considering the effect of the viscoelastic set $\tilde{\varepsilon}\widetilde{W}\iota_{\mathrm{k}}^{2}$ on the flow field. Fig. 3.4(a) shows the dimensionless velocity profile for pure electroosmotic flow ($\Lambda = 0$).We observed that at $\tilde{\varepsilon}\widetilde{W}\iota_{\mathrm{k}}^{2} = 0$, the flow is purely Newtonian and a velocity profile is nearly "plug like" with essentially no shear rate over much of the channel cross section. However, we observe a cross-over point in the velocity distribution for $\Lambda = 0$, which is attributed to the combined consequences of electroosmotic forces and the fluid rheology, which culminates into corresponding alternations in the local velocity gradient in a more dominant manner. Fig. 3.4(b) depicts the corresponding velocity distribution for $\Lambda < 0$. Flow enhancement in the microchannel is the combined influence of favourable pressure gradient and rheological parameter. We explain that with an increase in $\tilde{\varepsilon}\widetilde{W}\iota_{\mathrm{k}}^{2}$ causes the enhancement of the axial velocity within the EDL and in the bulk flow. Augmented value of $\tilde{\varepsilon}\widetilde{W}\iota_{\mathrm{k}}^{2}$ enhances the shear thinning characteristics of the PTT fluid. This leads to a

corresponding flow enhancement. However, for $\Lambda < 0$ the pressure forces acts along the same direction of electroosmotic forces inside the EDL, which rises the velocity gradient at the wall this leads to the increase in velocity. Hence both $\Lambda < 0$ condition and larger $\tilde{\varepsilon}\widetilde{W}\iota_k^2$ values contribute towards a net gain in flow velocity through the microchannel. Nevertheless, for the augmentation of flow velocity across the channel, the contribution of $\Lambda < 0$ is always predominant.

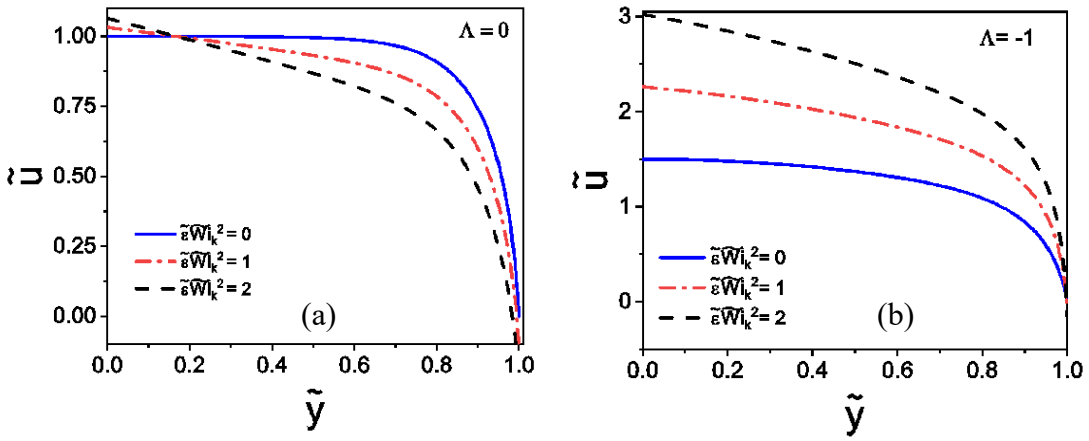

Fig. 3.4. The effect of varying viscoelastic set $\tilde{\varepsilon}\widetilde{W}\iota_k^2$ on the variation of dimensionless velocity profile across the transverse cross section of the microchannel at $\tilde{\zeta}$=5, $\tilde{k}$ =10 for (a) pure EOF ($\Lambda = 0$) and (b) at $\Lambda = -1$.

We plot the variation of dimensionless flow rate as a function of $\tilde{\varepsilon}\widetilde{W}\iota_k^2$ for various Λ in Fig. 3.5(a). It shows that, a favourable pressure gradient accelerates the overall ionic transport, resulting in an increase in the flow rate. In contrast, for pure electroosm otic flow, we observe that the degree of surface charging has a weak influence on the volumetric flow rate as the overall ionic transport primarily dictates by the EOF force, which in general has a lower strength compared to the pressure gradient forces. Moreover, an increment in the value of $\tilde{\varepsilon}\widetilde{W}\iota_k^2$ attributes towards increasing shear thinning effect that leads to the linear enhancement in the flow rate. In Fig. 3.5(b), we show the variation of $\tilde{Q}_f$ with $\tilde{\varepsilon}\widetilde{W}\iota_k^2$ for different $\tilde{\zeta}$ and at $\Lambda = -1$. In general, an increase in surface charging enhances the bulk ionic concentration of ions and thereby triggers bulk advective transport of the fluid flow. This effect results in the gradual amplification of the flow velocity and, therefore, corresponding augmentation of the flow rate. We see that the dimensionless volumetric flow rate increases with $\tilde{\varepsilon}\widetilde{W}\iota_k^2$ for all $\tilde{\zeta}$. The shear thinning effect is brought about in the flow rheology by an increase in $\tilde{\varepsilon}\widetilde{W}\iota_k^2$. That, in turn, triggers the fluid velocity within the microchannel and as a result gradual increase

in volumetric flow rate. We also note that higher magnitude of surface charging leads to a sharper gradient in the $\tilde{Q}_f - \tilde{\varepsilon}\widetilde{W}\iota_{\mathrm{k}}^2$ distribution.

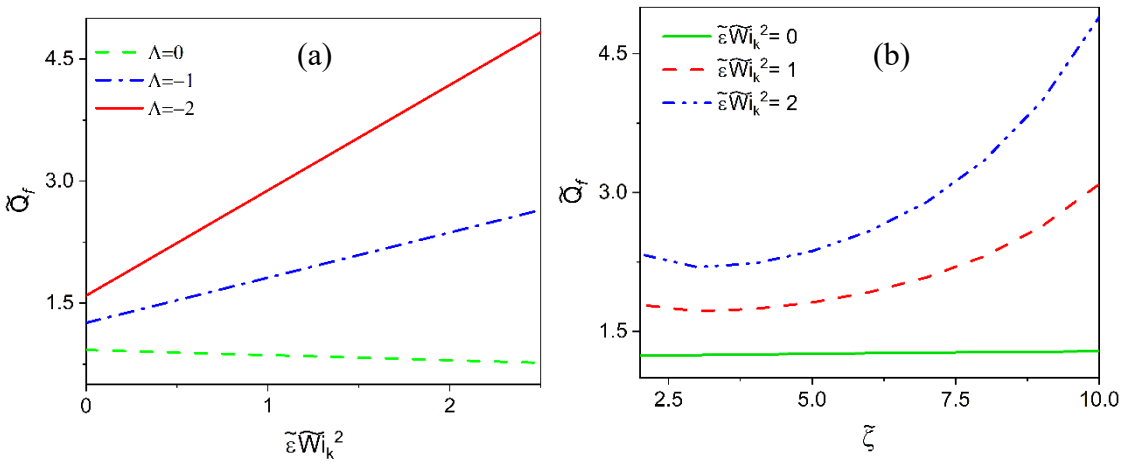

Fig. 3.5. (a) Variation in volumetric flow rate with dimensionless $\tilde{\varepsilon}\widetilde{W}\iota_{\mathrm{k}}^2$ for various Λ, at $\tilde{\zeta}$=5, $\tilde{k}$=10. (b) Dependence of $\tilde{Q}_f$ with $\tilde{\zeta}$ for varying $\tilde{\varepsilon}\widetilde{W}\iota_{\mathrm{k}}^2$ at $\tilde{k}$=10 , $\Lambda = -1$.

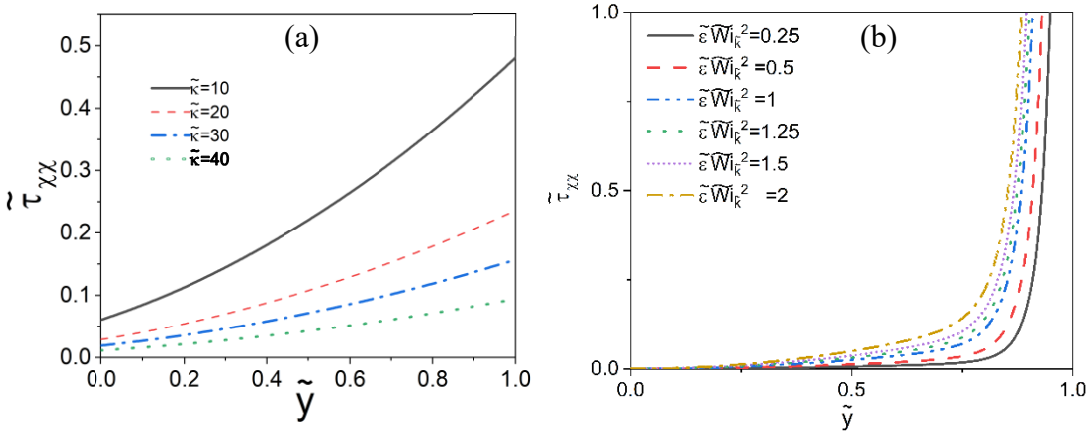

Fig. 3.6. Variation in normal stress across the microchannel for (a) different values of EDL thickness $\tilde{k}$ and at Λ =-1, $\tilde{\zeta}$=1, $\tilde{\varepsilon}\widetilde{W}\iota_{\mathrm{k}}^2 = 1$; (b) various values of $\tilde{\varepsilon}\widetilde{W}\iota_{\mathrm{k}}^2$ and at Λ =-1, $\tilde{\zeta}$=5, $\tilde{k} = 10$.

3.4.2 Normal and shear stress distribution

Fig. 3.6 illustrate the variation of dimensionless normal stress across the microchannel for different values of the dimensionless EDL thickness $\tilde{k}$ Fig.3.6(a) and $\tilde{\varepsilon}\widetilde{W}\iota_{\mathrm{k}}^2$ Fig.3 6(b.) The other pertinent parameters are mentioned in the caption. We see that in Fig 3.6(a) $\tilde{\tau}_{xx}$ reduces with an increase in $\tilde{k}$. A larger value of $\tilde{k}$ signifies thin EDL, whereas at lower $\tilde{k}$ causes considerable enhancement in the electroosmotic body forces due to accumulation of counterions within EDL. As a result, the shear rate gradually rises within the EDL, which eventually yields in the concomitant rise of the near wall velocity gradient owing to the combined consequence of applied pressure gradient and electrokinetic forcing. Fig.3 6(b) depicts that increasing values of $\tilde{\varepsilon}\widetilde{W}\iota_{\mathrm{k}}^2$

contributes towards the shear thinning effect of the fluid. That attributes to the gain in flow velocity at the core of the channel. As a consequence, there is a significant rise in the velocity gradient in the vicinity of the wall. That, in turn, causes a sudden increase in normal stress. We observe that the normal stress vanishes as it approaches the centerline of the channel. This behavior indicates a lowering of velocity radient at the channel core as attributed to the mass conservation within the flow domain.

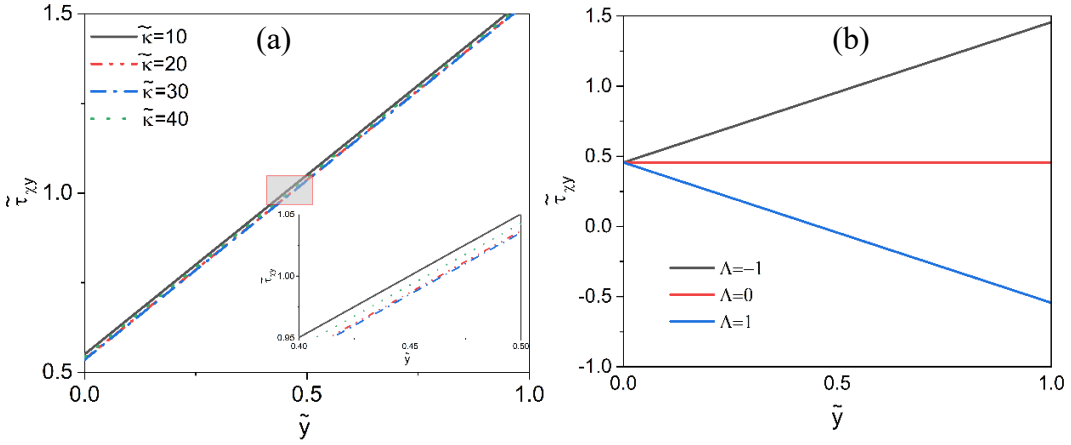

Fig. 3.7. Variation of dimensionless shear stress across the microchannel for various values of (a) $\tilde{k}$ and at $\tilde{\zeta}$=1, $\tilde{\varepsilon}\widetilde{W}\iota_{\mathrm{k}}^{2} = 1$; in (b) for Λ and at $\tilde{\zeta}$=1, $\tilde{\varepsilon}\widetilde{W}\iota_{\mathrm{k}}^{2} = 1$,$\tilde{k}$=10

Fig 3.7 delineates the effect of $\tilde{k}$ and Λ on shear stress distribution across the microchannel. It is important to note that, same as normal stress, the shear stress also vanishes to zero at the core region and shows sudden upsurge near the wall. This distinctive phenomenon is due to complex interplay between the fluid rheology and physiochemical surface conditions which results in sharp increase in velocity gradient within the EDL. This is illustrated more in Fig.3.7(a), which describes that the overall impact of $\tilde{k}$ results a concurrent rise in the magnitude of shear stress near the wall. We further observe that though not very significant but shear stress follows a decreasing trend for higher values of $\tilde{k}$. This attributed to the facts that, a lower value of $\tilde{k}$ represents the thick EDL, where Debye length is higher.

This significantly increases the bulk ionic conductivity of the flow, resulting in a sudden rise in velocity gradient near the wall. This, in turn, leads to the increment in shear stress. Similarly for higher values of $\tilde{k}$, due to lower Debye length, bulk resistivity is more that opposes the flow, thereby decreases the velocity gradient and correspondingly the shear stress. In the core region, the flow is steady as the velocity gradient as well as shear stress diminishes to zero. The shear thinning fluid, because

of its intrinsic nature, experience a dramatic alternation in the shear stress behavior under the influence of axial pressure gradient. Fig.3. 7(b) depicts the influence of the mixed pressure gradient /electro-osmotic forcing on the $\tilde{\tau}_{xy}$ (the other related parameter has been mentioned in caption).

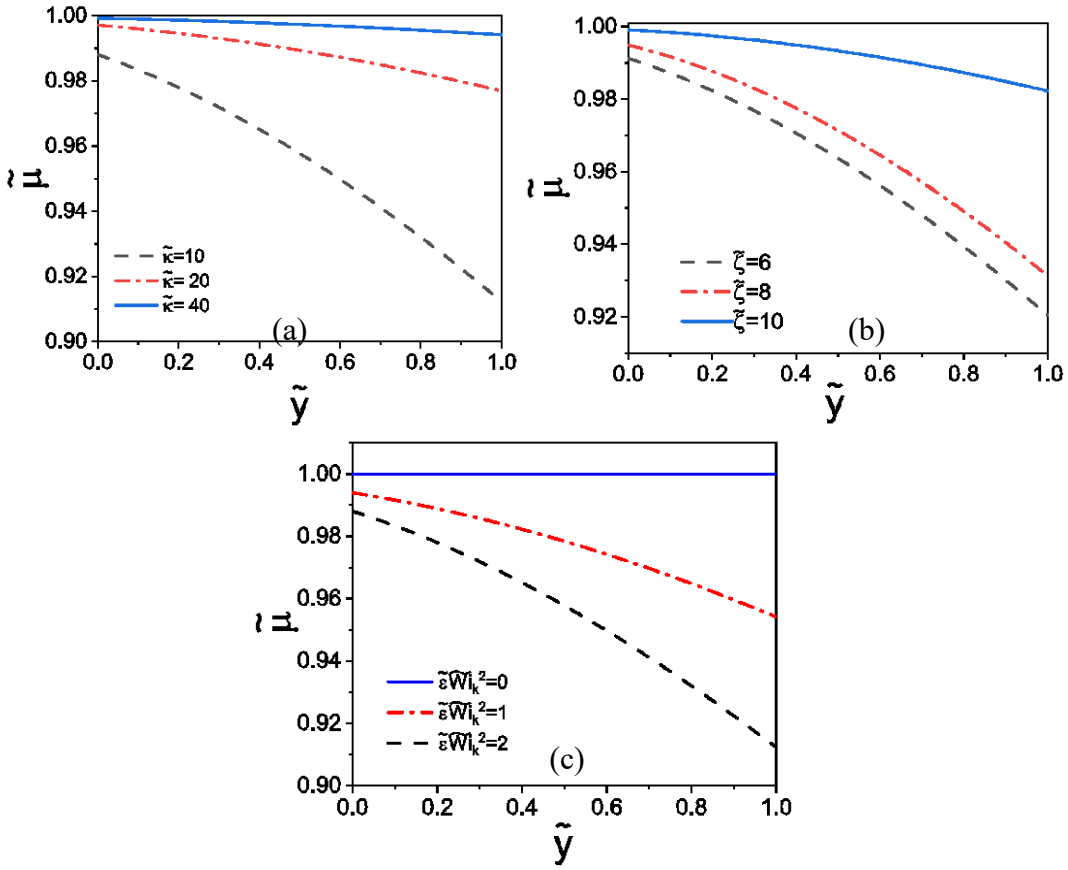

Fig. 3.8. Variation of dimensionless shear viscosity across microchannel at Λ = -1 for different values of (a) EDL thickness and at $\tilde{\zeta} = 5$, $\tilde{\varepsilon}\widetilde{W}\iota_k^2 = 2$; (b) dimensionless zeta potential and at $\tilde{k} = 10$, $\tilde{\varepsilon}\widetilde{W}\iota_k^2$ =2; (c) viscoelastic set $\tilde{\varepsilon}\widetilde{W}\iota_k^2$ and at $\tilde{\zeta} = 5$, $\tilde{k} = 10$.

It shows that at the wall, τ_{xy} increases for favourable pressure gradient, remains constant for pure electroosmotic flow and then it reduces for adverse pressure gradient condition. The reason is that the favourable pressure gradient assists the electroosmotic flow inside the EDL which results in higher velocities and thereby larger velocity gradients near the wall and then results in higher $\tilde{\tau}_{xy}$. Without an applied pressure gradient, the resulting "plug-type" flow represents the pure electroosmotic flow associated with a constant velocity gradient, encountering negligible or null variation in the shear stress. In contrast, an adverse pressure gradient opposes the electroosmotic body forces inside the EDL and causes impediment in the flow due to a decrease in velocity gradient concurrent with the shear stress.

Fig. 3.8(a), depicts the distribution of shear viscosity $\tilde{\mu}$ across the microchannel as a function of $\widetilde{k}$. We observe that in case of shear thinning fluid, $\tilde{\mu}$ gradually decays from the core to the wall of microchannel. This is attributed to the fact that the core region encounters a lower velocity gradient and thus, there is an increment in the value of $\tilde{\mu}$. Hence, in the core region, we observe the maximum value of $\tilde{\mu}$ which is approximately equals to 1. In contrast, at the wall of microchannel, there is sudden augmentation in the velocity gradient. A higher velocity gradient reduces $\tilde{\mu}$ at the wall. We found that the variation in velocity gradient at wall is due to the change in electroosmotic forces inside the EDL, and the variation in electroosmotic forces depends on the value of $\widetilde{k}$. The electroosmotic forces at $\widetilde{k}$=10 is higher and as result there is a preferential accumulations of counterions inside the EDL, that results in a larger wall velocity gradient. That ultimately reduces $\tilde{\mu}$ to its minimum value. In contrast, weak ionic strength at $\widetilde{k}$=40 lowers the velocity gradient within the EDL, resulting in a larger value of $\tilde{\mu}$.

Fig. 3.8(b) illustrates the effect of surface charging on shear viscosity distribution across the channel. A general trend followed in this plot is that by increasing value of $\tilde{\zeta}$ there is a progressive decrement in $\tilde{\mu}$ from the core to the wall region of the channel. An increase in $\tilde{\zeta}$, increases the concentration of counterions in the EDL region. This leads to the enhancement in the advective transport of the bulk flow. Consequently, there is a sharp rise in the velocity gradient, which subsides $\tilde{\mu}$ at the wall. We observe that $\tilde{\mu}$ peaks at the core of the bulk flow and is subjected to the least velocity gradient. It is observed that for higher values of $\tilde{\zeta}$, the rate of fall of shear viscosity from the core to the wall region is lower. The physical reason behind this behaviour is that a higher value of $\tilde{\zeta}$ increases the advective strength of the ionic species. That gives rise to the back electrokinetic strength. This consequential influence leads to the electroviscous retardation, which gradually drops the velocity gradient. Hence, at higher values of $\tilde{\zeta}$, the overall reduction of $\tilde{\mu}$ is lesser.

Fig.3. 8(c) displays the variation in $\tilde{\mu}$ with $\tilde{y}$ for varying magnitude of $\tilde{\varepsilon}\widetilde{W}\iota_{\mathrm{k}}^{2}$ (other related parameter are mention in caption). It is found that with the increase in $\tilde{\varepsilon}\widetilde{W}\iota_{\mathrm{k}}^{2}$, there is a corresponding decrement in $\tilde{\mu}$ across the channel. It has already been mention in the preceding section that an increase in $\tilde{\varepsilon}\widetilde{W}\iota_{\mathrm{k}}^{2}$ enhances the shear thinning effect of the fluid, that contributes towards the rise in the velocity gradient near the wall.

Thus, it offers less resistance to the flow and thereby causing the concomitant reduction in $\tilde{\mu}$ near the wall. We notice that at the core region of channel, $\tilde{\mu}$ attains the maximum value and is as a result of the lower velocity gradient due to vanishing shear thinning effect.

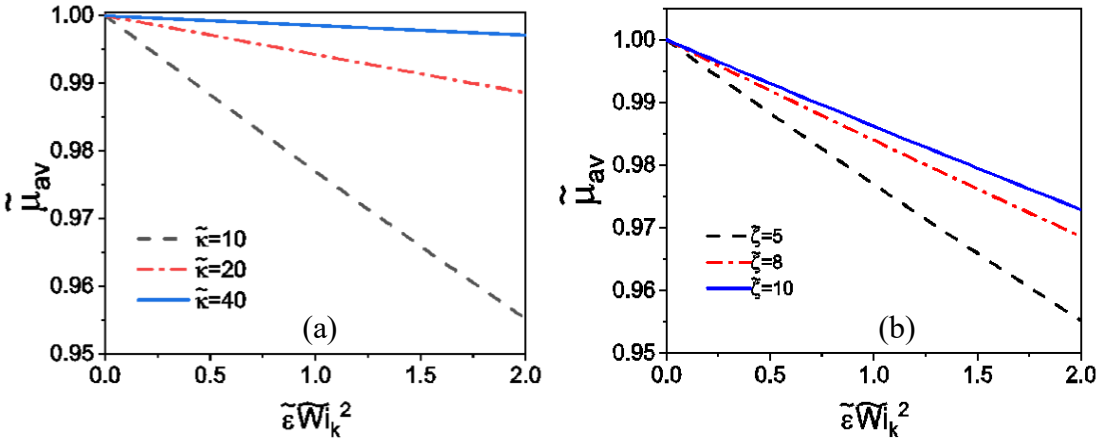

Fig. 3.9. Variation of the dimensionless average shear viscosity with $\tilde{\varepsilon}\widetilde{W}\iota_k^2$ for various values of (a) $\tilde{k}$ and at Λ =-1, $\tilde{\zeta}$=5, $\tilde{\varepsilon}\widetilde{W}\iota_k^2 = 2$; (b) $\tilde{\zeta}$ and at Λ =-1$\tilde{\varepsilon}\widetilde{W}\iota_k^2 = 2$, $\tilde{k}$=10.

Fig. 3.9 illustrates the effects of electro hydrodynamic flow parameters on the dimensionless transverse average shear viscosity $\tilde{\mu}_{av}$. The other pertinent parameters are mentioned in the caption. We observe that at $\tilde{k} = 10$, there is a sharp drop of $\tilde{\mu}_{av}$ at higher values of $\tilde{\varepsilon}\widetilde{W}\iota_k^2$. The underlying physics behind such trend is as follows: at the lower value $\tilde{k} = 10$, large accumulation of counterions inside the EDL causes enhancement in the near wall velocity gradient, that leads to the reduction in the value of $\tilde{\mu}_{av}$ to its minima. In contrast, for higher values of $\tilde{k}$, the weak ionic strength inside the EDL depletes the growth in velocity gradient near the wall. Thus we found that at $\tilde{k} = 40$, there is a gradual rise in $\tilde{\mu}_{av}$. We further notice that $\tilde{\mu}_{av}$ attains the minimum value at higher magnitude of $\tilde{\varepsilon}\widetilde{W}\iota_k^2$ and is invariant with $\tilde{k}$. This implies that the viscoelastic set $\tilde{\varepsilon}\widetilde{W}\iota_k^2$ contributes towards the shear thinning effect, that results in rise of the liquid velocity.

Therefore, a higher values of $\tilde{\varepsilon}\widetilde{W}\iota_k^2$ represents a larger flow velocity possessing lower magnitude of $\tilde{\mu}_{av}$. Hence, the cumulative effect of $\tilde{k}$ and $\tilde{\varepsilon}\widetilde{W}\iota_k^2$ culminates in the reduction of the average shear viscosity. Fig. 3.9(b) delineates the combined influence of rheological and electrokinetic parameters on the average shear viscosity. The flow velocity augments with $\tilde{\zeta}$ and its contribution towards electrokinetic flow is to amplify the relative strength of counterions inside the EDL, which results in an amplification

of the flow velocity. That consequently reduces the value of $\tilde{\mu}_{av}$. An increase in $\tilde{\varepsilon}\widetilde{W}\iota_{\mathrm{k}}^{2}$ leads to the growth in the near wall velocity gradient and thereby yielding a decrement in $\tilde{\mu}_{av}$. The physical reason behind the phenomena is due to the enhanced shear thinning effect at higher $\tilde{\varepsilon}\widetilde{W}\iota_{\mathrm{k}}^{2}$. We further notice that the slope of $\tilde{\mu}_{av}$ across the $\tilde{\varepsilon}\widetilde{W}\iota_{\mathrm{k}}^{2}$ is more steeper for higher values of $\tilde{\zeta}$ as compared to larger value of $\tilde{k}$.

3.5 Concluding remarks

This chapter has provided a rigorous hydrodynamic assessment of combined electroosmotic and pressure-driven flow of sPTT viscoelastic fluids through narrow confinements, capturing the intricate interplay between electrokinetic forcing, pressure gradients, and viscoelastic stresses. Analytical solutions obtained for velocity, volumetric flow rate, stress components, and shear viscosity were systematically evaluated under varying EDL thickness, surface charge strength, and viscoelastic parameter set.

The velocity profiles demonstrated distinct asymmetries near the walls due to enhanced shear rates in the EDL, with significant influence from the viscoelastic parameter . A favorable pressure gradient combined with higher viscoelastic relaxation amplified flow rates, whereas adverse pressure gradients suppressed flow due to electroviscous opposition. Volumetric flow rate showed non-linear dependence on both surface charge and viscoelastic strength, emphasizing rheology-sensitive electrohydrodynamic modulation. Normal and shear stress distributions revealed sharp peaks near the walls, vanishing at the centreline, consistent with mass conservation and shear-thinning behavior. Increased EDL strength and surface charge elevated near-wall stress gradients, indicating elastic stretching and stress localization. Shear viscosity exhibited a strong transverse decay from the channel core to walls, driven by local shear enhancement and electrostatic interactions. Notably, higher κ and ζ values led to reduced average viscosity, confirming viscoelastic softening effects under strong electroosmotic action.

Altogether, the results emphasize the non-trivial coupling of fluid rheology with electrohydrodynamic phenomena, underscoring the need for stress-based viscoelastic models like sPTT in accurate electrokinetic flow prediction. These findings lay the groundwork for subsequent analyses involving thermal transport, streaming potential, and entropy generation, particularly relevant in energy conversion, bioanalytical devices, and soft microfluidics.

Chapter 4. Streaming potential mediated pressure driven flow of sPTT fluids in a microchannel

This chapter presents a comprehensive numerical investigation into the streaming potential-driven transport of viscoelastic fluids modeled via the simplified Phan–Thien–Tanner (sPTT) constitutive framework. The electrostatic interactions are modeled using the nonlinear Poisson–Boltzmann equation, thereby capturing the spatial variation of electric double layer potential beyond the linearized Debye–Hückel regime. The governing equations are solved under isothermal, steady-state, and low Reynolds number assumptions, with emphasis on the electrohydrodynamic interplay, velocity field modulation, and rheological stress distribution.

4.1 Mathematical formulation

4.1.1 Physical model

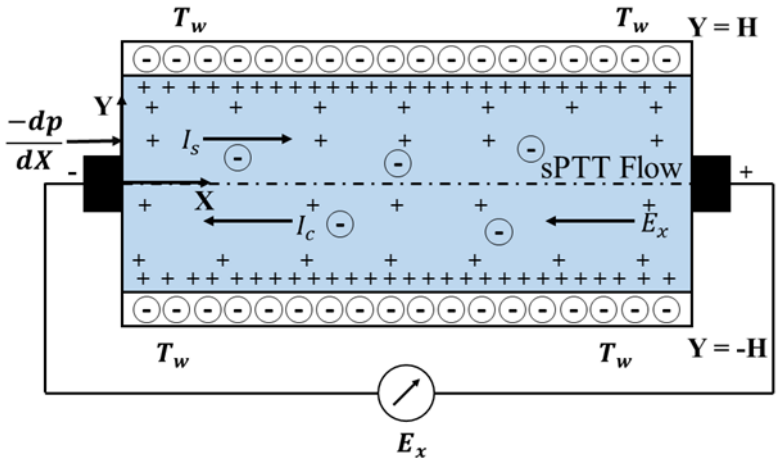

Fig. 4.1. Schematic diagram of the set-up showing streaming mediated pressure driven sPTT fluid through a rectangular microchannel.

We study steady, incompressible, two-dimensional pressure-driven flow of sPTT fluids with symmetric electrolytes ($z_+ = z_- = z$, z being the valency) through a long, narrow slit-like microchannel with parallel walls at a constant wall temperature T_w. Fig.4.1 shows the schematic of the problem, including the coordinate system. Two parallel walls of a narrow confinement are separated by a height of $2H$ and a length of L. The width is assumed to be much larger than these dimensions. The origin is set at the center of the confinement, with coordinates X along the axial direction and Y along the direction

transverse to the walls. The flow is driven by a constant axial pressure gradient $-dp/dX$. In microchannels, even without an applied electric field, fluid flow generates an electrical field. The potential difference across the confinement due to this field, called the streaming potential E_x, opposes the driving convective influences of the pressure gradient, as illustrated in Fig. 1. We further assume that the thermophysical properties of the fluid are independent of temperature, the ionic species behave as point charges, and the wall zeta potential (ζ) is uniform throughout the channel walls.[48]

4.1.2 EDL potential distribution

The EDL potential distribution (ψ) within the EDL, is governed by the Poisson equation and is represented in terms of the net charge density distribution (ρ_e) [10]

$$\frac{d^2\psi}{dY^2} = -\frac{\rho_e}{\varepsilon_p} \tag{4.1}$$

Here ε_p the fluid permittivity. We assume insignificant ionic advection compared to diffusion in the wall-transverse direction and for a symmetric dilute electrolyte, the ion concentration can be expressed as

$$n_{\pm} = n_0 \exp(z_{\mp} e\psi / k_B T) \tag{4.2}$$

where, e denotes protonic charge, and n_0 is the bulk ionic concentration (the product of the ionic molar concentration C and Avogadro's number N_A), k_B is the Boltzmann constant and T is the absolute temperature. Therefore,

$$\rho_e = e(z_+ n_+ - z_- n_-) = -2n_0 ez \sinh\left(\frac{ez\psi}{k_B T}\right) \tag{4.3}$$

We employ Eqs. (4.1) and (4.3), to obtain,

$$\frac{d^2\psi}{dY^2} = k^2 \sinh\left(\frac{ez\psi}{k_B T}\right) \tag{4.4}$$

Where $k = (2n_0 z^2 e^2 / \varepsilon_p k_B T)^{1/2} = 1/\lambda_D$ is the Debye–Hückel parameter with λ_D denoting the Debye length .

On integrating the Eq. (4) which is subjected to set of boundary conditions as $\left[\frac{d\psi}{dY}\right]_{Y=0} = 0$ and $[\psi]_{Y=H} = \zeta$, we obtain an analytical solution for governing EDL potential distribution in dimensionless form as [2]

$$\bar{\psi}(\bar{y}) = 4\tanh^{-1}\left[\tanh\left(\frac{\bar{\zeta}}{4}\right)\exp\left\{-\bar{k}\left(1-\bar{y}\right)\right\}\right] \tag{4.5}$$

We have used the following dimensionless scales to make Eq. (4.5) dimensionless: $\bar{y} = Y/H$, $\bar{k} = kH$, $\bar{\psi} = ez\psi/k_BT$ and $\bar{\zeta} = ez\zeta/k_BT$.

For small values of zeta potential $(\zeta \le 25mV)$, one may obtain the EDL potential distribution using the Debye–Hückel linearization approximation[48]

$$\bar{\psi}(\bar{y}) = \bar{\zeta}\frac{\cosh\left\{\cosh\left(\bar{y}\bar{k}\right)\right\}}{\cosh\left(\bar{k}\right)} \tag{4.6}$$

4.1.3 Velocity distribution and the streaming potential

The fluid flow equations for the electrokinetically mediated pressure-driven flow of sPTT fluid is governed by the continuity and modified Cauchy's momentum equation,[34]

$$\nabla.\vec{U} = 0 \tag{4.7a}$$

$$\rho\frac{D\vec{U}}{Dt} = -\nabla P + \nabla.\tau + \mu_{eff}\nabla^2\vec{U} + F_B \tag{4.7b}$$

where $\vec{U}$ is the velocity vector, ρ is density of fluid, and τ is the extra stress tensor subjected to the polymeric contribution, μ_{eff} is the Newtonian solvent viscosity. For present viscoelastic fluid, we assume that the Newtonian solvent viscosity is negligible in contrast to polymeric contribution, thus $\mu_{eff} = 0$. In momentum equation Eq. (4.7b), the source term F_B is the body force per unit volume in consequence of electrokinetic flow resulting from development in streaming potential field E_X and is given as

$$F_B = \rho_e E_X \tag{4.8}$$

Constitutive Equation for PTT Model

The sPTT constitutive relationships, the polymeric extra-stress tensor τ can be represented in a compact generic equation as[34]

$$f(tr\tau)\tau + \lambda\overset{\nabla}{\tau} = 2\eta_v\overline{\overline{D}} \tag{4.9}$$

Here, λ is the fluid relaxation time, η_v is the polymeric viscosity coefficient, $\overline{\overline{D}}$ is the tensor indicating the rate of deformation which reads as $\overline{\overline{D}} = (\nabla\vec{U} + \nabla\vec{U}^T)/2$, and $\overset{\nabla}{\tau}$ is the Gordon-Schowalter convective derivative of the stress tensor represented as

$$\overset{\nabla}{\tau} = \frac{D\tau}{Dt} - \left(\nabla \vec{U}^T.\tau + \tau.\nabla \vec{U}\right) \tag{4.10}$$

Additionally, $f(tr\tau)$ is the scalar function representing the trace of the polymeric extra-stress tensor for sPTT model, given as,

$$f(tr\tau) = 1 + \frac{\varepsilon\lambda}{\eta_v}\tau_{kk} \tag{4.11}$$

The extensibility parameter ε in Eq. (4.11) controls the fluid extensional viscosity, is coupled with the trace of the extra stress tensor $\tau_{kk} = \tau_{xx} + \tau_{yy} + \tau_{zz}$. It should be mentioned that the Johnson-Segalman constitutive equation $\left(f(\tau_{kk}) = 1\right)$ can be obtained for diluted polymeric solutions by setting $\varepsilon = 0$. We assume fully developed, two-dimensional, unidirectional flow $(\tau_{zz} = 0)$, which invokes $(u(\bar{y}),0,0)$. These factors allow Eq. (9) to be simplified to the following form[48]

$$f(\tau_{xx} + \tau_{yy})\tau_{xx} = 2\lambda\left(\frac{dU}{dY}\right)\tau_{xy} \qquad \tilde{u}\big|_{y=\pm 1} = 0 \qquad \text{4. 12(a)}$$

$$f(\tau_{xx} + \tau_{yy})\tau_{yy} = 0 \qquad u\big|_{y=\pm 1} = du/dy \qquad \text{4. 12(b)}$$

$$f(\tau_{xx} + \tau_{yy})\tau_{xy} = \left(\eta_v + \lambda\tau_{yy}\right)\left(\frac{dU}{dY}\right) \qquad \text{4. 12(c)}$$

From the above, we obtain the following relationship among shear and normal stresses

$$\tau_{xy} + \frac{2\varepsilon_s\lambda^2}{\eta_v^{\,2}}\left(\tau_{xy}\right)^3 = \eta_v\left(\frac{dU}{dY}\right) \tag{4.13}$$

4.1.4 Analytical solution for the velocity distribution

In the study, we examined steady, incompressible, and fully developed microchannel flow, accordingly, the Cauchy momentum equations (Eq. 4.7) becomes

$$\frac{d\tau_{xy}}{dY} = \frac{dp}{dX} + \varepsilon_p E_x \frac{d^2\psi}{dY^2} \tag{4.14}$$

In the study, the pressure gradient along the streamwise direction is denoted by dp/dX, while E_x represents the induced streaming potential field. By assuming symmetric

conditions at the channel centerline and a nonoverlapping EDL, Equation (4.14) can be integrated once to derive an expression for shear stress,

$$\tau_{xy} = \left(\frac{dp}{dX}\right) Y + \varepsilon_p E_x \frac{d\psi}{dY} \tag{4.15}$$

By substituting Eq. (4.15) into Eq. (4.13) and after making dimensionless with the following dimensionless variables: $\bar{u} = U/U_{ref}$ here the reference velocity $U_0 = -(dp/dX)H^2/\eta_v$, $E = E_x/E_0$, with the reference induced potential $E_0 = -(dp/dX)H^2/\varepsilon_p\zeta$, to obtain

$$\frac{d\bar{u}}{d\bar{y}} = \left(\frac{E}{\bar{\zeta}}\frac{d\bar{\psi}}{d\bar{y}} - \bar{y}\right) + \frac{2\varepsilon\bar{W}i_k^2}{\bar{k}^2}\left(\frac{E}{\bar{\zeta}}\frac{d\bar{\psi}}{d\bar{y}} - \bar{y}\right)^3, \tag{4.16}$$

where the viscoelastic parameter is referred as Weissenberg number and is given as $\bar{W}i_k^2 = \lambda k U_{ref} = \lambda\bar{k}U_{ref}/H$ .We employ symmetry boundary conditions at the channel centreline and no-slip boundary conditions for velocity at the walls and integrate Eq. (4.17) to obtain an analytical formula for the velocity distribution of the form

$$\begin{aligned}
\bar{u}(\bar{y}) &= \frac{24\varepsilon\bar{W}i_k^2 E}{\bar{\zeta}\bar{k}^4}\left[Li_3\left\{ge^{\bar{k}(\bar{y}-1)}\right\} - Li_3\left\{-ge^{\bar{k}(\bar{y}-1)}\right\} + Li_3(-g) - Li_3(\mathrm{g})\right] \\
&+ \frac{24\varepsilon\bar{W}i_k^2 E}{\bar{\zeta}\bar{k}^3}\left[\bar{y}Li_2\left\{-ge^{\bar{k}(\bar{y}-1)}\right\} - \bar{y}Li_2\left\{ge^{\bar{k}(\bar{y}-1)}\right\} + Li_2(g) - Li_2(-g)\right] \\
&- \frac{24\varepsilon\bar{W}i_k^2 E}{\bar{\zeta}^2\bar{k}^2}\left[\ln\left(\frac{e^{2\bar{k}} - g^2e^{2\bar{k}\bar{y}}}{e^{2\bar{k}} - g^2e^{2\bar{k}}}\right) - \frac{\bar{\zeta}\bar{y}^2}{2E}\ln\left\{\frac{1+ge^{\bar{k}(\bar{y}-1)}}{1-\left\{ge^{\bar{k}(\bar{y}-1)}\right\}}\right\} - \frac{\bar{\zeta}}{2E}\ln\left\{\frac{1+g}{1-g}\right\} + \frac{\varepsilon\bar{W}i_k^2}{2\bar{k}^2}\left(1-\bar{y}^4\right)\right] \\
&+ 16\varepsilon\bar{W}i_k^2 g\left(\frac{E}{\bar{\zeta}}\right)^3\left[\frac{e^{\bar{k}(\bar{y}+1)}}{g^2e^{2\bar{k}\bar{y}} - e^{2\bar{k}}} + \frac{2e^{\bar{k}(\bar{y}+3)}}{\left(e^{2\bar{k}} - g^2e^{2\bar{k}\bar{y}}\right)^2} - \frac{3\bar{y}\bar{\zeta}e^{2\bar{k}}}{gE\bar{k}\left(e^{2\bar{k}} - g^2e^{2\bar{k}\bar{y}}\right)} + \frac{3\bar{\zeta}}{gE\bar{k}(1-g^2)}\right] \\
&- \frac{48\varepsilon\bar{W}i_k^2 E}{\bar{\zeta}^2\bar{k}}(1-\bar{y}) - \frac{16\varepsilon\bar{W}i_k^2 gE(1+g^2)}{\bar{\zeta}^3(1-g^2)^2} + \frac{16\varepsilon\bar{W}i_k^2 E}{\bar{\zeta}^3}\left[\tanh^{-1}(g) - \tanh^{-1}\left\{ge^{\bar{k}(\bar{y}-1)}\right\}\right] \\
&+ \frac{4E}{\bar{\zeta}}\left[\tanh^{-1}\left\{ge^{\bar{k}(\bar{y}-1)}\right\} - \tanh^{-1}(g)\right] + \frac{1}{2}(1-\bar{y}^2)
\end{aligned} \tag{4.17}$$

Here, $g = \tanh(\bar{\zeta}/4)$. The Jonquière's function, also known as the polylogarithm $Li_r(\alpha) = \sum_{i=1}^{\infty}\frac{\alpha^i}{i^r}$, with order *r* and argument α.

4.1.5 Analytical solution for volumetric flow rate and stress distribution

We provide an analytical equation for the dimensionless volumetric flow rate, as

$$\bar{Q}_f = \frac{Q_f}{2HwU_{ref}} = \int_o^1 \bar{u}(\bar{y})d\bar{y} \tag{4.18a}$$

$$\begin{aligned}\bar{Q}_f = {} & \frac{72\varepsilon\bar{W}i_k^2E}{\bar{\zeta}\bar{k}^5}\left[Li_4(g)-Li_4(-g)+\frac{2}{3}Li_4\left(-e^{-\bar{k}}g\right)+\frac{1}{3}Li_4\left(-e^{\bar{k}}g\right)-Li_4\left(e^{-\bar{k}}g\right)\right]+\frac{72\varepsilon\bar{W}i_k^2E}{\bar{\zeta}\bar{k}^4}\left[Li_3(-g)-Li_3(g)\right] \\ & +\frac{72\varepsilon\bar{W}i_k^2E^2}{\bar{\zeta}^2\bar{k}^3}\left[Li_2\left(g^2\right)-\frac{1}{3}Li_2\left(e^{-2\bar{k}}g^2\right)+\frac{\bar{\zeta}}{36\varepsilon\bar{W}i_k^2E}Li_2(-g)\left\{2\varepsilon\bar{W}i_k^2\left(\frac{2\bar{k}^2E^2}{\bar{\zeta}^2}-9\right)-\bar{k}^2\right\}\right. \\ & \left.+\frac{\zeta}{36\varepsilon\bar{W}i_k^2E}Li_2(g)\left(-\frac{4\varepsilon\bar{W}i_k^2\bar{k}^2E^2}{\bar{\zeta}^2}+18\varepsilon\bar{W}i_k^2+\bar{k}^2\right)\right]+\frac{24\varepsilon\bar{W}i_k^2E^2}{\bar{\zeta}^2\bar{k}^2}\left[\ln\left\{\frac{\left(1-g^2\right)}{\left(e^{2\bar{k}}-g^2\right)}\right\}-\frac{\bar{\zeta}}{2E}\ln\frac{1-g}{1+g}+\frac{2\bar{k}}{1-g^2}+\frac{\bar{\zeta}^2}{60E^2}\right] \\ & +\frac{16\varepsilon\bar{W}i_k^2E^3}{\bar{\zeta}^3\bar{k}}\left[\frac{g}{1-g^2}-\frac{ge^{\bar{k}}}{e^{2k}-g^2}+\frac{1}{2}Li_2(-ge^{-\bar{k}})-\frac{\bar{k}g(1+g^2)}{(1-g^2)^2}-\frac{\bar{k}}{2}\ln\frac{1-g}{1+g}\right] \\ & +\frac{2E}{\bar{\zeta}\bar{k}}\left[Li_2\left(-ge^{-\bar{k}}\right)-Li_2\left(ge^{-\bar{k}}\right)\right]+\frac{2E}{\bar{\zeta}}\ln\frac{1-g}{1+g}+\frac{1}{3}\end{aligned} \tag{4.18b}$$

The dimensionless streaming potential field E in Eqs. (4.17) -(4.18) is an unknown parameter, whose value can be determined by assessing the electroneutrality condition, as elaborated in detail in section 4.1.6.

To derive expressions for the polymeric stress distribution, we simplify the constitutive relationships expressed in Eqs. 4.12(a)-(c) to establish an interrelationship between normal and shear stress as follows:[48], [53]

$$\tau_{xy}^2 = \frac{\eta_v}{2\lambda}\tau_{xx} \tag{4.19}$$

We now substitute the Eq. (15) in Eq. (19) to obtain the following expressions for dimensionless normal and shear stress components

$$\bar{\tau}_{xx} = \frac{\tau_{xx}}{\eta_v\bar{k}U_0} = \frac{2\varepsilon\overline{Wi}_k^2}{\bar{k}^2}\left[\frac{E}{\bar{\zeta}}\left(\frac{d\psi}{dY}\right)-Y\right]^2 \tag{4.20a}$$

$$\bar{\tau}_{xy} = \bar{y}-\frac{4Eg\bar{k}e^{(\bar{y}-1)\bar{k}}}{\bar{\zeta}\left(1-g^2e^{2\left(\bar{k}\bar{y}-\bar{k}\right)}\right)} \tag{4.20b}$$

$$\bar{\tau}_{xx} = \frac{2\varepsilon\overline{Wi}_k^2}{\bar{k}^2}\left[\frac{4Eg\bar{k}e^{(\bar{y}-1)\bar{k}}}{\bar{\zeta}\left(1-g^2e^{2(\bar{k}\bar{y}-\bar{k})}\right)}\right]^2 \tag{4.20c}$$

Furthermore, the non-dimensional shear rate may be expressed as

$$\dot{\gamma} = \frac{\bar{\chi}}{\left(-U_0/H\right)} = \left[\bar{y} - \frac{4Eg\bar{k}e^{(\bar{y}-1)\bar{k}}}{\bar{\zeta}\left(1-g^2e^{2(\bar{k}\bar{y}-\bar{k})}\right)}\right]\left[1 + \frac{2\varepsilon\overline{Wi}_k^2}{\bar{k}^2}\left(\bar{y} - \frac{4Eg\bar{k}e^{(\bar{y}-1)\bar{k}}}{\bar{\zeta}\left(1-g^2e^{2(\bar{k}\bar{y}-\bar{k})}\right)}\right)^2\right] \tag{4.21}$$

Finally, the non-dimensional shear viscosity is given by

$$\bar{\mu} = \left[1 + \frac{2\varepsilon\overline{Wi}_k^2}{\bar{k}^2}\left(\bar{y} - \frac{4Eg\bar{k}e^{(\bar{y}-1)\bar{k}}}{\bar{\zeta}\left(1-g^2e^{2(\bar{k}\bar{y}-\bar{k})}\right)}\right)^2\right]^{-1} \tag{4.22}$$

The expression for the transverse averaged shear viscosity may be defined as

$$\bar{\mu}_{av} = \int_0^1 \bar{\mu}\, d\bar{y} \tag{4.23}$$

Note that for the Newtonian fluid, $\varepsilon\overline{Wi}_k^2 = 0$ and hence, $\bar{\mu}_{av} = \bar{\mu}$.

4.1.6 The overall electroneutrality condition

In the absence of an external electric field, the induced electric field maintains zero net current through the narrow confinement. This net current arises from the streaming current due to net ionic advection, conduction current from electromigration, and conduction current through the Stern layer. This condition constrains the solution's electrical neutrality. Hence[48]

$$I_{stream} + I_{cond} + I_{stern} = 0 \tag{4.24}$$

Here, I_{stream} denotes the streaming current, I_{cond} the conduction current flowing through the fluid layers that are "mobile," and I_{stern} is the conduction current flowing through the layer of fluid that is "immobilized." We make the assumption that the ions are moving through EDL at the local fluid velocity, and may write,

$$I_{stream} = \int_{-H}^{H} ze(n_+ - n_-)Udy \tag{4.25a}$$

$$I_{cond} = \frac{z^2 e^2 E_x}{f} \int_{-H}^{H} (n_+ - n_-)dy \tag{4.25b}$$

$$I_{stern} = 2\sigma_{stern} E_x \tag{4.25c}$$

Here, the ionic friction factor, $f = 2n_0 z^2 e^2 / \sigma_B$, is considered to be the same for both cationic and anionic species; σ_{stern} denotes the conductivity of the stern layer, while σ_B denotes the bulk ionic conductivity. The above physical statement has a dimensional mathematical expression expressed as:

$$\cdot\ I_{stream} = \int_{-H}^{H} ze(n_+ - n_-)Udy + \frac{z^2 e^2 E_x}{f} \int_{-H}^{H} (n_+ - n_-)dy + 2\sigma_{stern} E_x. \tag{4.25d}$$

Dimensionless form of equation (25d) will be given as below

$$\int_0^1 \bar{u}(\bar{y}) \sinh(\bar{\psi}) d\bar{y} - \frac{\alpha E}{\bar{\zeta}} \left[\int_0^1 \cosh(\bar{\psi}) d\bar{y} + Du \right] = 0, \tag{4.25e}$$

where $Du = \sigma_{stern} / H\sigma_B$ is the Dukhin number and $\alpha = \eta_v \sigma_B / 2\varepsilon n_0 \left(k_B T\right)$ is the dimensionless conductivity parameter[48].

4.2 Results and Discussions

To validate our numerical model, we compare our semi-analytical findings for streaming potential-mediated pressure-driven flow of a Newtonian fluid in parallel plate microchannels with a previously established semi-analytical solution documented in Dey *et al*.[137] Fig. 4.2 compares the dimensionless velocity variation across the microchannel for the parameters mentioned in the caption. We clearly observe that our results are in good agreement with the data shown in Dey *et al*.[137]. To integrate practical considerations into our physical description, we model the non-Newtonian fluid as a representative biofluidic sample. We characterize its thermophysical properties at a standard temperature T=300 K as: density $\rho \approx 10^3\ kg/m^3$, fluid viscosity $\eta_v \sim 10^{-3} - 10^{-2}$ Pa s, permittivity $\varepsilon_p \approx 702.24 \times 10^{-12}\ C^2/Jm$ and the Boltzmann constant $k_B = 1.38064852 \times 10^{-23} m^2 kg s^{-2} K^{-1}$.

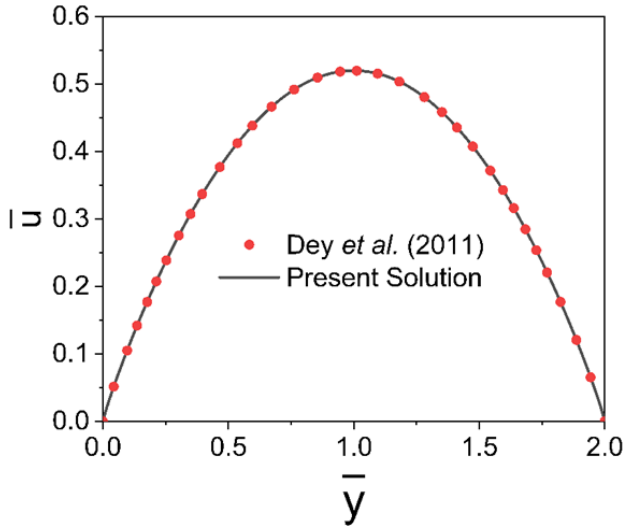

Fig. 4.2. Comparison results between the dimensionless velocity cross the microchannel with the published results of Dey *et al.*[137] for $\varepsilon \bar{W} i_k^2 = 0$ at $\bar{k} = 5$, and $\bar{\zeta}$=5.

Additionally, when considering the aforementioned parameters, the dimensional zeta potential ranges from 0 to 50mV. The analysis incorporates several dimensionless parameters, including the ratio of the half-height of the confinement to the Debye length ($\bar{k}$), dimensionless zeta potential ($\bar{\zeta}$), thermal Peclet number (Pe), effective Joule heating parameter (Sp_{eff}), and the viscous dissipation parameter (Br). For thermally developing flows, we have considered, Pe = 1-3, Br =0.01-10, Sp_{eff}=0-10. For a microchannel, the length and width generally varies of the order of L≈ W≈ O($10^3 \mu m$), whereas the channel height H≈ $O(10\mu m)$, and hence, the relevant dimensionless electrokinetic parameter value throughout the analysis is kept in the range $\bar{k} = 10 - 40$.

4.2.1 Streaming potential and flow field

Fig. 4.3(a) shows the dependence of dimensionless streaming potential as a function of $\bar{\zeta}$ and $\bar{k}$ for the parameters given in the caption. We see that as the zeta potential increases, the streaming potential field initially peaks and then declines exponentially at higher $\bar{\zeta}$ values. This occurs because higher zeta potentials boost ion concentration in the EDL, promoting pressure-driven ion streaming.

This enhances both reverse streaming potential and back electrokinetic transport, but they offset each other, resulting in a peak streaming potential field at an intermediate zeta potential. Beyond this, forward streaming current dominates, decreasing the streaming potential to maintain electroneutrality. Higher $\bar{\zeta}$ values accelerate the streaming potential decay in the diffuse EDL. In high zeta potential regimes, interactions between

electrokinetic effects and fluid rheology become nonlinear, making them difficult to superimpose. Notably, beyond $\bar{k} = 40$, streaming potential remains unchanged, attributed to thin EDL limits with increased ionic resistance and decreased bulk ionic conductivity. This leads to a weaker streaming potential field. For detailed electrohydrodynamics within the EDL, characteristics resembling thick EDL limits, preferably $\bar{k} = 10$, are essential.[48]

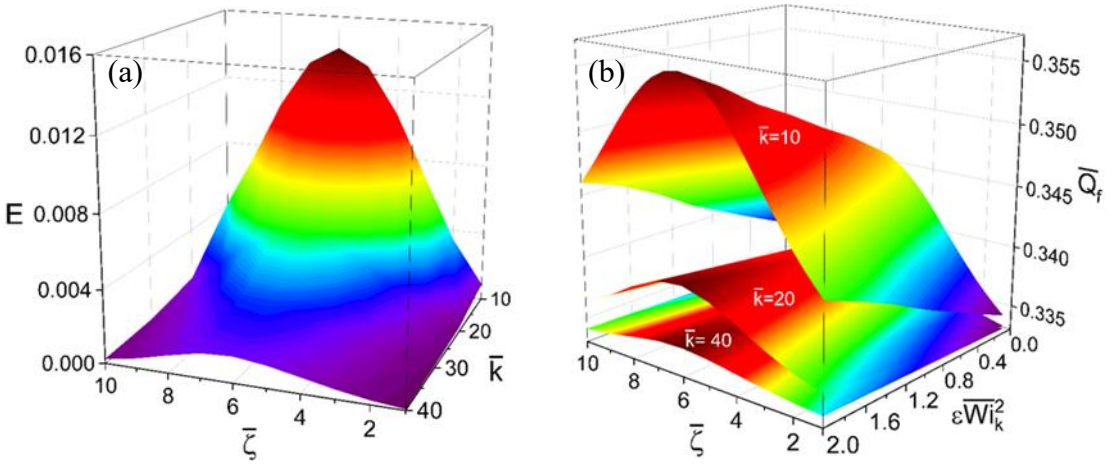

Fig. 4.3. Variation of (a) streaming potential (E) with $\bar{\zeta}$ and $\bar{k}$ for $\varepsilon\overline{Wi}_k^2 = 2$ (b) volumetric flow rate $\bar{Q}_f$ with $\varepsilon\overline{Wi}_k^2$ and $\bar{\zeta}$ for $\bar{k} = 10, 20\ and\ 40$

Fig. 4.3(b) depicts how the volumetric flow rates responds to the corresponding change in fluid rheology and degrees of surface charging. Surface charging influences the volumetric flow rate by affecting ionic concentration and advective fluid transport. Initially, increased surface charge boosts flow velocity and flow rate due to enhanced ionic concentration. However, once surface charging surpasses a threshold ($\bar{\zeta} \approx 6$), forward streaming current reduces induced streaming potential, diminishing flow rate over time. In the diffuse zone of the electrical double layer (EDL), higher $\bar{\zeta}$ values lead to an immediate drop in streaming potential magnitude and flow rate due to an increase in the effective pre-exponentiation factor. Additionally, nonlinear coupling between electrokinetic effects and non-Newtonian fluid rheology at higher zeta potential regimes has a non-trivial effect on flow rate. We observe that $\bar{Q}_f$ increases with $\varepsilon\overline{Wi_k}^2$, enhancing shear thinning and fluid velocity within the microchannel, consequently raising the flow rate. However, beyond the threshold vicinity of $\bar{\zeta}$=6, the cumulative effect of $\bar{\zeta}$ and $\varepsilon\overline{Wi_k}^2$ decreases flow rate exponentially due to the predominance of the electroviscous effect. Notably, electrohydrodynamic effects are more pronounced at lower $\bar{k}$ values. At $\bar{k}$=10,

variations in flow rate are more amplified compared to $\bar{k}$=40, indicating that appropriate $\bar{\zeta}$ and $\varepsilon\overline{Wi_k}^2$ values can maximize flow rates.

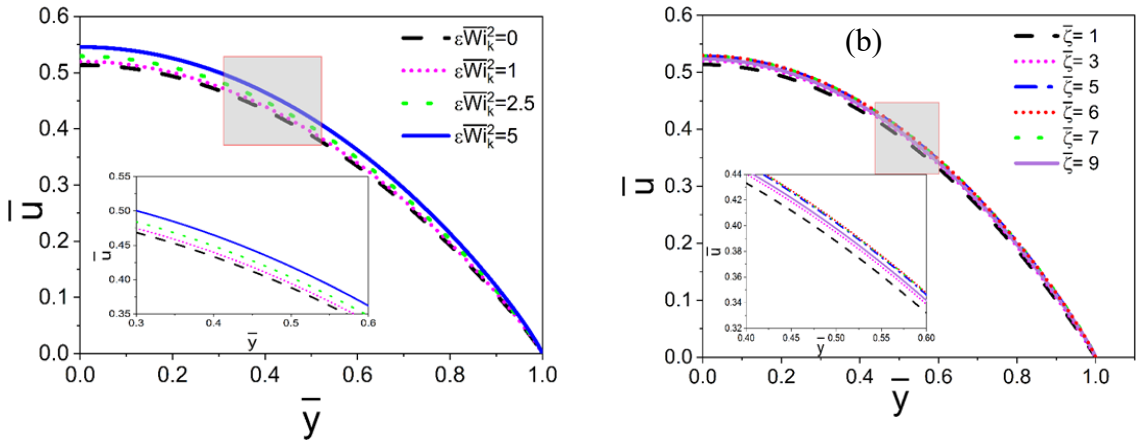

Fig. 4.4. Variation of dimensionless velocity profile across the microchannel at $\bar{k}=10$ for various values of (a) $\varepsilon\overline{Wi_k}^2$ at $\bar{\zeta}$=6; (b) $\bar{\zeta}$ at $\varepsilon\overline{Wi_k}^2$=1.5.

Fig. 4.4 shows the dimensionless velocity variation across the microchannel for various values of $\varepsilon\overline{Wi_k}^2$ and $\bar{\zeta}$ for the parameters given in the caption. We observe that the overall velocity distribution is parabolic, flattening at the channel centerline. The dimensionless velocity increases with $\varepsilon\overline{Wi_k}^2$. As discussed, the flow rheology exhibits a shear thinning effect when the non-dimensional viscoelastic parameter $\varepsilon\overline{Wi_k}^2$ increases, leading to an increase in fluid velocity within the microchannel. Fig. 4.4(b) shows that as the surface charge, $\bar{\zeta}$, increases, the dimensionless velocity $\tilde{u}$, also increases, peaking around $\bar{\zeta}$=6. Beyond this point, $\tilde{u}$ asymptotically declines as $\bar{\zeta}$ increases further. These opposing trends in the hydrodynamic scenario at different $\bar{\zeta}$ values are attributable to the development of the streaming potential.[48] The Fig.4.5 (a) clearly illustrate that an increase in $\varepsilon\overline{Wi_k}^2$ leads to higher stress components. This increase indicates a shift in fluid rheology towards a more pronounced shear-thinning behavior, which significantly raises the velocity gradient within the EDL near the wall. This notable change in velocity gradients also causes the stress components to rise. As a result, the normal stress is higher near the wall and diminishes to zero in the core region. We observe that the normal stress is only slightly influenced by the level of surface charge ($\bar{\zeta}$). The increase in shear thinning due to higher $\varepsilon\overline{Wi_k}^2$ has a more impact on the normal stress than the increase in bulk ionic conductivity from greater. $\bar{\zeta}$ However, it's worth noting that higher surface

charge does enhance ionic transport in the EDL region near the wall, leading to a slight increase in $\bar{\tau}_{xy}$.

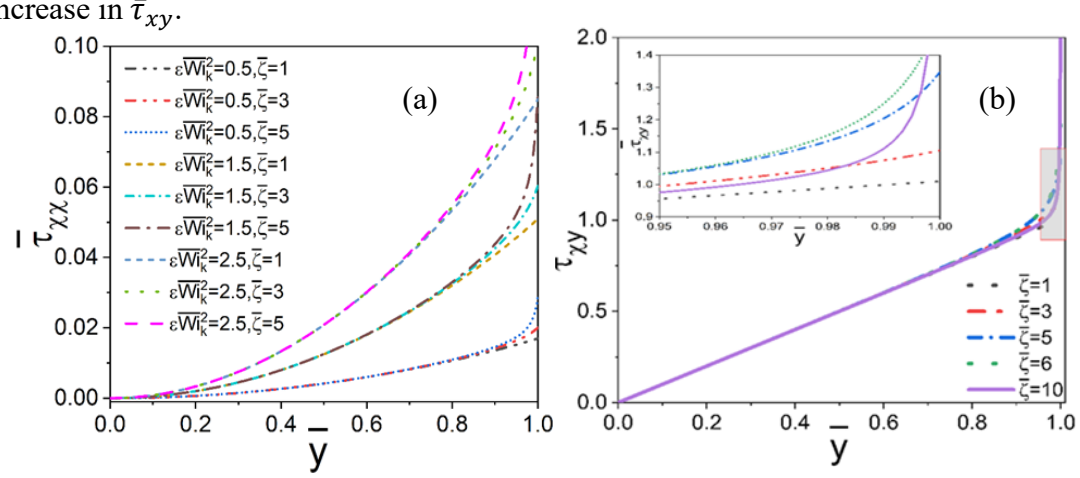

Fig. 4.5. Distribution of dimensionless (a) normal stress for various $\varepsilon\overline{Wi_k}^2$ and $\bar{\zeta}$ at $\bar{k} =$ 10 ; (b) shear stress for different $\bar{\zeta}$ at =1.5, $\varepsilon\overline{Wi_k}^2$ at $\bar{k}$=10.

Fig.4.5(b) shows the influence of $\bar{\zeta}$ on $\bar{\tau}_{xy}$ across the microchannel for various$\bar{\zeta}$. Shear stress reduces to zero at the core region and sharply increases near the wall. This behavior can be explained as follows. An increase in zeta potential significantly affects the dimensionless shear stress near the wall, causing the curve to bifurcate at the transition point *P*. This indicates that a higher surface charge intensity in the EDL region enhances ionic advective transport, which in turn increases the fluid velocity gradient and varies the dimensionless shear stress. Additionally, although Eq. (4.20b) shows that the viscoelastic parameter does not directly affect shear stress distribution, $\overline{\tau}_{xy}$ is indirectly related to $\varepsilon\overline{Wi_k}^2$ through the induced streaming potential field *E*, which depends on $\varepsilon\overline{Wi_k}^2$.

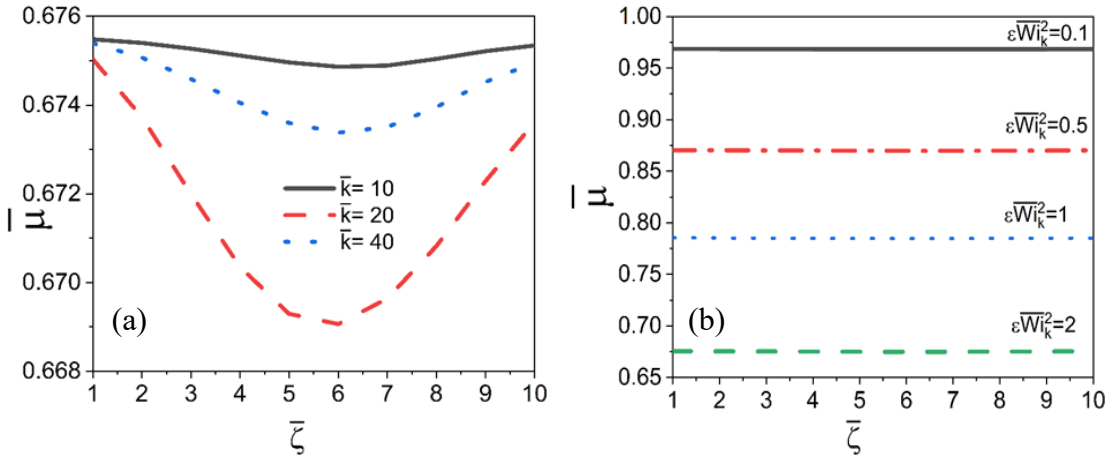

Fig. 4.6. Variation of (a) shear viscosity ($\bar{\mu}$) with $\bar{\zeta}$ for different (a) $\bar{k}$ and for $\varepsilon\overline{Wi_k}^2 = 2$; (b) $\varepsilon\overline{Wi_k}^2$ and for $\bar{k} = 10$.

Fig. 4.6(a) shows the variation of $\bar{\mu}$ with $\bar{\zeta}$ for various $\bar{k}$, while, corresponding variations for different $\varepsilon\overline{Wi_k}^2$ is shown in Fig.4. 6(b) (other pertinent parameters are mentioned in the caption. As $\bar{\zeta}$ increases, $\bar{\mu}$ experiences a notable decline, reaching a minimum around$\bar{\zeta} = 6$. This minimum signifies a critical point where the shear-thinning behavior of the fluid is most pronounced, leading to reduced flow resistance. However, beyond this threshold, $\bar{\mu}$ gradually increases, indicating a shift towards higher viscosity. The inverse correlation between $\bar{\mu}$ and $\bar{\zeta}$ is evident, reflecting the intricate interplay between electrokinetic effects and fluid rheology. Furthermore, the significant influence of the parameter $\bar{k}$ on $\bar{\mu}$ underscores the importance of considering confinement effects on viscosity dynamics. In Fig. 4.6(b), the relationship between $\bar{\mu}$ and $\bar{\zeta}$ is further explored, shedding light on the impact of $\varepsilon\overline{Wi_k}^2$. Remarkably, increasing $\varepsilon\overline{Wi_k}^2$ induces a considerable decrease in $\bar{\mu}$, indicative of enhanced shear thinning properties within the PTT fluid.[34] This reduction in viscosity can be attributed to intensified flow velocity gradients, resulting in diminished flow resistance and shear viscosity. Notably, the viscosity profile remains spatially invariant with respect to $\bar{\zeta}$, highlighting a distinct feature—a sudden dip near the channel wall rather than a gradual decline from the core. This observation underscores the complex interplay between fluid behavior and boundary effects, offering valuable insights for understanding microfluidic phenomena.

4.3 Concluding remarks

This study presents a detailed analytical framework to characterize pressure-induced streaming potential-mediated transport in microchannel confinements, wherein the working fluid exhibits viscoelastic behavior governed by the simplified Phan–Thien–Tanner (sPTT) model. By resolving the nonlinear Poisson–Boltzmann equation in conjunction with the momentum and rheological transport equations under isothermal and low Reynolds number constraints, the analysis captures the complex interdependence between charge distribution, elastic stress evolution, and flow kinematics. The results reveal that the loss of local electroneutrality within the electric double layer, induced by pressure-driven ion advection, generates a streaming potential that feeds back into the momentum balance through an opposing electric field which significantly alters the hydrodynamic response of the system, particularly under conditions of elevated Weissenbergh number $\varepsilon\overline{Wi_k}^2$ and moderate-to-high zeta potential. Notably, the elastic contributions inherent to the sPTT model intensify the non-

uniformity in velocity gradients and enhance axial stress asymmetry, which, in turn, modulate the induced electrostatic body force distribution. Such nonlinear coupling leads to marked deviations in volumetric throughput and wall shear stress profiles compared to Newtonian analogs.

Furthermore, confinement effects accentuate the competition between elastic relaxation time scales and electrokinetic force fields, giving rise to rheo-electrohydrodynamic feedback that is highly sensitive to channel dimensions and fluid rheology. These insights are critical for advancing the design and optimization of micro- and nano-scale electrokinetic platforms, where accurate prediction of flow characteristics under coupled electro-rheological effects is imperative.

Chapter 5. Thermally developing combined electroosmotic and pressure driven transport of sPTT fluids in a microchannel

This chapter presents a focused analysis of thermally developing flow and convective heat transfer in narrow microchannels under combined electroosmotic and pressure-driven actuation, with the fluid modeled using the simplified Phan–Thien–Tanner (sPTT) viscoelastic framework. Building on the hydrodynamic studies in earlier chapters, the emphasis here is on the thermal entrance region, where axial temperature gradients evolve from an initially uniform profile. This region is particularly sensitive to electrokinetic and rheological parameters, significantly affecting local heat transfer, boundary layer growth, and entropy generation. By solving the coupled momentum and energy equations—including Joule heating and viscous dissipation—the study captures the interplay of electrohydrodynamics and thermal transport, offering insights into Nusselt number variation and thermodynamic efficiency relevant to microfluidic device design

5.1 Mathematical Model

5.1.1 Physical problem

We consider the model problem of pressure driven flow through a 2D rectangular microchannel separated by two parallel walls of height $2H$, length L, and its width is assumed to be much larger than either of these dimensions. The origin is set at the centre of the confinement; coordinates X, the axial direction, and Y being the direction transverse to the walls. In addition to a favourable pressure gradient $-dP/dX$ acting along the axial (X) direction, an applied electric field of strength E_X also acts and imparts necessary driving force for EOF. The combined pressure–driven and electroosmotic actuation turns out to be the governing mechanism for the resultant fluidic transport through a narrow confinement. The physical problem together with the various external body forces as described here is schematically shown in Fig. 5.1. We consider that the microchannel walls are maintained at a constant temperature T_W. It may be mentioned in this context that we have assumed temperature independent

thermophysical properties of the fluid and also variation due to changes in local ionic concentration are neglected. In the following analysis, we delineate the development of electrical double layer (EDL) at the walls of the micrchannel and its implication on the associated thermofluidic transport phenomena.[36]

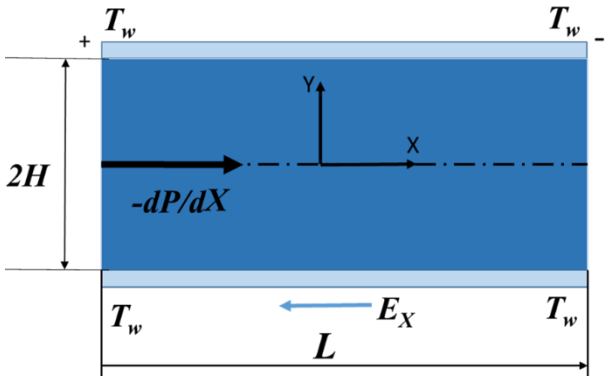

Fig. 5.1. Schematic depiction of the physical problem together with the various external body forces.

5.1.2 Thermal energy transport equation for thermally developing flow

From the theoretical models presented earlier, it is evident that a combination of applied electric field, and imposed pressure gradient, in effect, governs the thermofluidic flow and heat transfer characteristics within the narrow confinement. In the foregoing discussions, we elucidate the interesting interplay between various physical parameters that give rise to the resultant flow actuation mechanism imparted through the several forcing parameters on the system. In order to demonstrate the results, we choose corresponding thermo–physical properties at a reference temperature $T_W = 300\,\mathrm{K}$ to be of order, $\mu \approx 10^{-3}\,\mathrm{kg/m.s}$, $\rho \approx 10^3\,\mathrm{kg/m^3}$, $\varepsilon \approx 702.24\times10^{-12}\,\mathrm{C^2/J.m}$ [55]. For a $z:z$ symmetric electrolyte, the bulk ionic concentration (n_0) ranging from millimolarity to molarity, the magnitude of the dimensional zeta potential turns out to be in the tune of ~ 10 mV –50 mV We obtain the results in terms of the appropriate dimensionless parameters, the half channel height (H), we assume the range of H *as* 100 – 1000 nm. Furthermore, noting nondimensionlization of the pertinent parameters involved and typical to a fixed surface reaction conditions with a constant value of the zeta potential, the governing thermo–fluidic characteristics depend on the following dimensionless parameters: Λ (representing the relative strengths of the pressure-driven and electroosmotic flow actuations), Pe (thermal Peclet number), S_p (the Joule heating parameter), and Br (the viscous

dissipation parameter). For thermally developing flows we have considered,$Pe = 0.1 - 10,\ Br = 0.01 - 100,\ S_p = 1 - 100$ and presented the analysis in the subsequent section[36]

5.1.3 Electrohydrodynamic thermal transport

We have employed the velocity solution to characterize the temperature distribution and heat transfer inside the microchannel. We consider a typical situation for a thermally developing flow and solve thermal energy equation at a representative case when the channel walls are subjected to a constant wall temperature boundary condition. By taking into account of axial conduction, viscous dissipation, and volumetric Joule heating, the governing thermal energy transport equation for a temperature independent thermophysical and electrical property fluid can be written as follows[42]

$$\rho_e C_p \left[u \frac{\partial T}{\partial X} \right] = k_T \left(\frac{\partial^2 T}{\partial X^2} + \frac{\partial^2 T}{\partial Y^2} \right) - \eta \left(\frac{\partial u}{\partial Y} \right)^2 - S_j \tag{5.1}$$

where T is the local fluid's temperature. The density, heat capacity, and thermal conductivity of the fluid are given by ρ, C_p, and k_T, respectively. The term S_j is the volumetric heat generation due to Joule heating and the penultimate term $\eta(\partial u/\partial y)^2$ is the heat generation due to viscous dissipation. Following the assumption of weak advective effect on the transport of ionic species, we may write $S_j = \sigma_r E_x^2$. We now made Eq. (5.2) dimensionless with the following nondimensional variables: $\tilde{x} = x/H$, $\theta = (T - T_w)/(T_i - T_w)$ is the non-dimensional temperature of the fluid, where T_i is the fluid inlet temperature. Finally, the dimensionless form of energy transport equation Eq. (5.1) becomes

$$Pe \left[\tilde{u}(\tilde{y}) \frac{\partial \theta}{\partial \tilde{x}} \right] = \left(\frac{\partial^2 \theta}{\partial \tilde{x}^2} + \frac{\partial^2 \theta}{\partial \tilde{y}^2} \right) - Br \left(\frac{\partial u}{\partial \tilde{y}} \right)^2 - S_p \tag{5.2}$$

where $Pe = u_{HS} H / \{k_T (\rho C_p)\}$ is the thermal Peclet number. The dimensionless quantity signifying the contribution due to viscous dissipation is the Brinkman number, expressed as $Br = \eta u_{HS}^2 / k_T (T_w - T_i)$. The nondimensional quantity $S_p = H^2 S_j / k_T (T_w - T_i)$ represents the volumetric heat generation due to Joule heating. Equation (28) is subjected to the following boundary conditions in dimensionless form

$$(\theta)_{x=0} = 1 \quad \forall \quad 0 \le \tilde{y} \le 1 \tag{5.3a}$$

$$(\theta)_{y=\pm 1} = 0 \ \forall \ \ 0 < \tilde{x} < +\infty \tag{5.4b}$$

$$\left(\frac{\partial \theta}{\partial y}\right)_{y=0} = 0 \quad \forall \quad 0 < \tilde{x} < +\infty \tag{5.5c}$$

$$\theta < \infty \quad as \quad \tilde{x} \to +\infty \quad \forall \quad 0 \le \tilde{y} \le 1 \tag{5.6d}$$

To obtain the dimensionless temperature distribution, we have solved Eq. (5.1) along with the pertinent boundary conditions using finite volume based numerical technique. We developed a 2D numerical code that uses the first order upwind scheme for the convective terms, whereas second order central differencing scheme for the diffusion terms. The discretized sets of algebraic equations are then solved using a line-by-line TDMA (tri-diagonal matrix method) solver. The computational domain is chosen as shown in Fig. 1, where we have generated nonuniform quadrilateral finite volume cells with finer meshes near the channel boundaries. Finally, at various axial locations throughout the microchannel, we obtain the temperature distribution along the transverse sections.

At any arbitrary axial location, the dimensionless bulk mean temperature can be calculated as

$$\theta_m(\tilde{x}) = \frac{\int_{-1}^{1} \tilde{u}(\tilde{y})\theta(\tilde{x},\tilde{y})d\tilde{y}}{\int_{-1}^{1} \tilde{u}(\tilde{y})d\tilde{y}} \tag{5.7}$$

We consider the steady state energy balance at the walls and the bulk flow of the microchannel and obtain the corresponding expression for the *Nu* Nusselt number as

$$N_u = \frac{1}{\theta_m}\left(\frac{\partial \theta}{\partial \tilde{y}}\right)_{wall} \tag{5.8}$$

It is appropriate to note here that the numerical value of the Nusselt number is evaluated (from Eq. 5.8) by calculating the computationally obtained value of θ_m transverse direction at different axial locations of the narrow confinement.[36]

5.2 Results and Discussion

From the theoretical models presented earlier, it is evident that a combination of applied electric field, and imposed pressure gradient, in effect, governs the thermofluidic flow and heat transfer characteristics within the narrow confinement. In the foregoing discussions, we elucidate the interesting interplay between various physical parameters that give rise to the resultant flow actuation mechanism imparted through the several forcing parameters on the system. In order to demonstrate the results, we choose corresponding thermo–physical properties at a reference temperature $T_0 = 300\,\mathrm{K}$ to be of order, $\mu \approx 10^{-3}\ \mathrm{kg/m.s}$, $\rho \approx 10^{3}\ \mathrm{kg/m^3}$, $\varepsilon \approx 702.24\times10^{-12}\ \mathrm{C^2/J.m}$ .For a $z:z$ symmetric electrolyte, the bulk ionic concentration (n_0) ranging from millimolarity to molarity, the magnitude of the dimensional zeta potential turns out to be in the tune of $\sim 0-50$ mV. We obtain the results in terms of the appropriate dimensionless parameters, the half channel height (H), we assume the range of H *as* 100 –1000 nm. Furthermore, noting nondimensionlization of the pertinent parameters involved and typical to a fixed surface reaction conditions with a constant value of the zeta potential, the governing thermo–fluidic characteristics depend on the following dimensionless parameters: Λ (representing the relative strengths of the pressure-driven and electroosmotic flow actuations), Pe (thermal Peclet number), S_p (the Joule heating parameter), and Br (the viscous dissipation parameter). For thermally developing flows, we have considered,$Pe = 0.1-10$, $Br = 0.01-100$, $S_p = 1-100$ and presented the analysis in the subsequent section.[36]

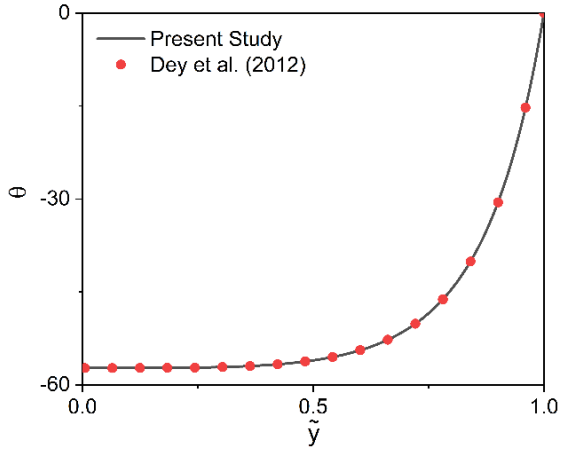

Fig. 5.2. Variation of dimensionless temperature distribution across the microchannel for thermally developed flow of Newtonian fluids at $\tilde{k} = 5$, $Br = 100, Pe = 1, S_p = 1$, $\Lambda = -1$. Results are compared with the data reported by Dey et al[33].

Figure 5.2. presents the dimensionless temperature profile across the channel height in the thermally fully developed region for Newtonian fluid flow. The numerical results obtained in this study show excellent agreement with the benchmark data from Dey et al.[33] , validating the thermal model and numerical scheme. The symmetric parabolic temperature distribution, with a maximum at the channel centerline and steeper gradients near the walls, is consistent with analytical expectations under constant wall heat flux. This validation confirms the accuracy of the simulation setup and supports its applicability for extended studies involving viscoelastic and electrokinetic effects.

5.2.1 Electrohydrodynamic thermal transport

In this section, we assess the influence of the electrohydrodynamic forcing on the temperature distribution in thermally developing flow for the selected range of parametric space discussed in the preceding sections.

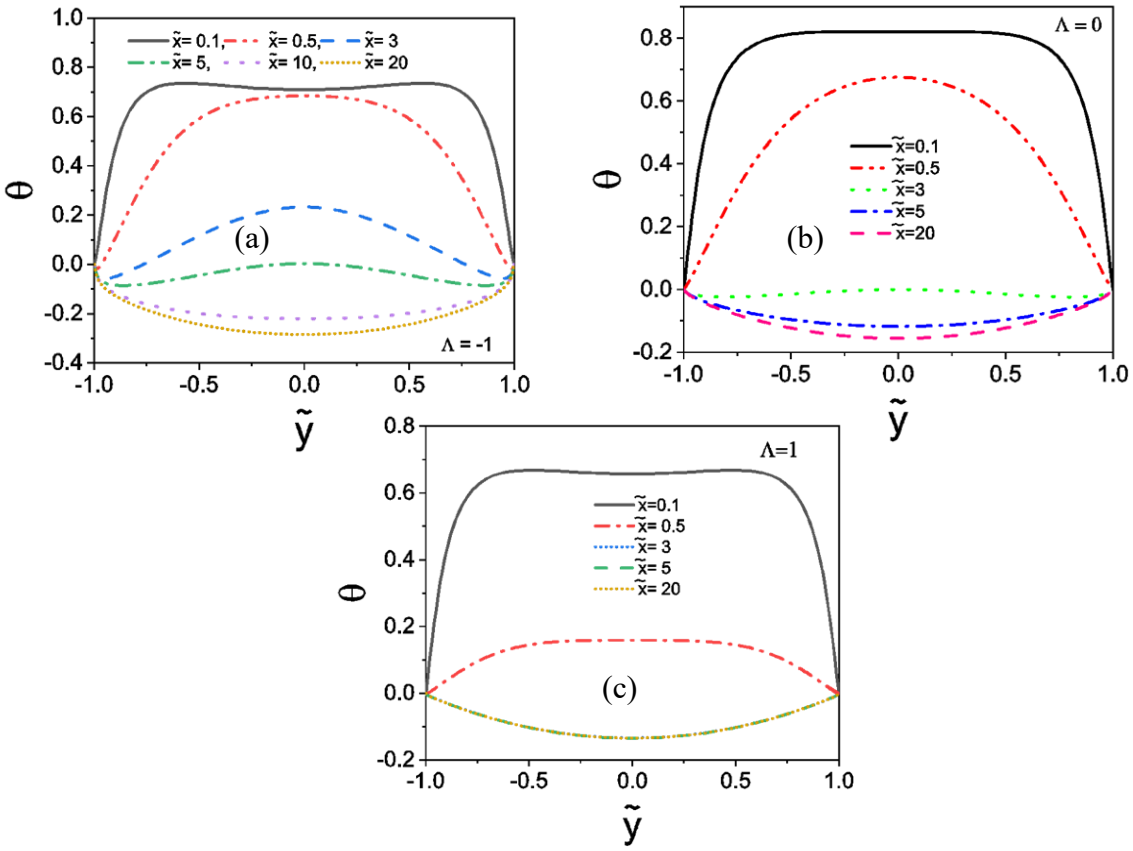

Fig. 5.3. Variation in temperature distribution along the transverse dimensionless coordinate axis $\tilde{y}$ at various axial locations for $\tilde{k} = 10, \tilde{\zeta} = 5, \tilde{\varepsilon}\widetilde{W}\iota_k^2 = 2$, $Pe = 3$, $Sp = 1$, $Br = 0.1$ at (a) $\Lambda = -1$, (b) $\Lambda = 0$, and (c) $\Lambda = 1$.

Figures 5.3 (a) – 5.3(c) represent the effects of parametric variations of Λ on the non-dimensional temperature distributions at different axial locations across the microchannel. Figure 5.3 (a) delineates the effect of favourable pressure gradient ($\Lambda <$

0) on the temperature distribution. We observe that the difference between fluid temperature T and wall temperature T_w (characterised by θ), at the entry region ($\tilde{x}$=0.1) reduces due development of the thermal boundary layer. Thereby augmenting the energy transfer from the wall to the flowing fluid. As a result, θ at the near wall region becomes minimum. However, θ increases from the channel wall to the core region due to the gradual convective heat transfer, moreover $T_w > T$. We also found that after attaining peak, θ remains fairly constant at most of the transverse locations, thereafter gradually falls to its minimum value in the near wall region. We further note that at $\tilde{x}$=10, θ is negative and is attributed to the fact that the value of the dimensionless temperature would always be positive if there is more wall heat transfer to the bulk flow, thereby causing the liquid temperature to increase. As such, T is always takes lesser value as $T_w > T_i$. The dimensionless temperature profile ceases to change on after $\tilde{x}$=15, indicating the flow to attain the thermally fully developed state. In this context, it may be mentioned here that the favourable pressure gradient enhances the advective bulk fluid transport, signifying the thinning of thermal boundary layer thickness.

Thus, thermally developing region is prominently visible here due to the extension in thermal entrance length. Moreover, advective bulk transport accelerates the heat transfer rate, which ultimately rises the bulk mean temperature of the fluid. Therefore, the difference between the wall and bulk mean temperature reduces. The resultant effect lowers the magnitude of θ and it progressively decreases till the thermally fully developed state.

The overall trend in the temperature distribution for Λ=0 Fig. 5.3(b) remains the same as in the favourable-pressure-gradient case. Although, we observe plug-flow type temperature distribution at $\tilde{x}$=0.1. For pure electroosmotic flow, the Joule heating effect is more dominant than that of $\Lambda < 0$. Also the dominant effect of volumetric heat generation imparts heat to the bulk fluid such that the bulk mean temperature exceeds the wall temperature at much faster rate, which subsides the value of θ. Therefore, the flow attains the thermally fully developed state at much lower axial distance from the inlet as compared to the favourable pressure gradient situation. Figure 5.3(c) depicts the temperature distribution across the microchannel at various axial locations for the adverse-pressure gradient case. It is found that the overall fluid temperature distribution at any axial location (Λ>0) opposes the electroosmotic flow, thus retards the advective

fluid transport at a smaller rate. Therefore, the effects of volumetric heat source become more dominant as the flow rate becomes smaller. Hence, the thermal entry length is much shorter when an adverse pressure gradient is imposed to the pure electro-osmotic flow. This implies that at any particular location, the difference in wall and bulk fluid temperature is less than that of a favourable-pressure-gradient flow. Through a comparative study we may conclude that the fluid temperature at any axial position will be higher in an adverse-pressure-gradient situation than that of the pure electro-osmotic or favourable-pressure-gradient mixed flow, is higher than that of favourable-pressure-gradient case. Since the adverse pressure gradient that results quick attainment of thermally fully develop flow at shortest axial distance.

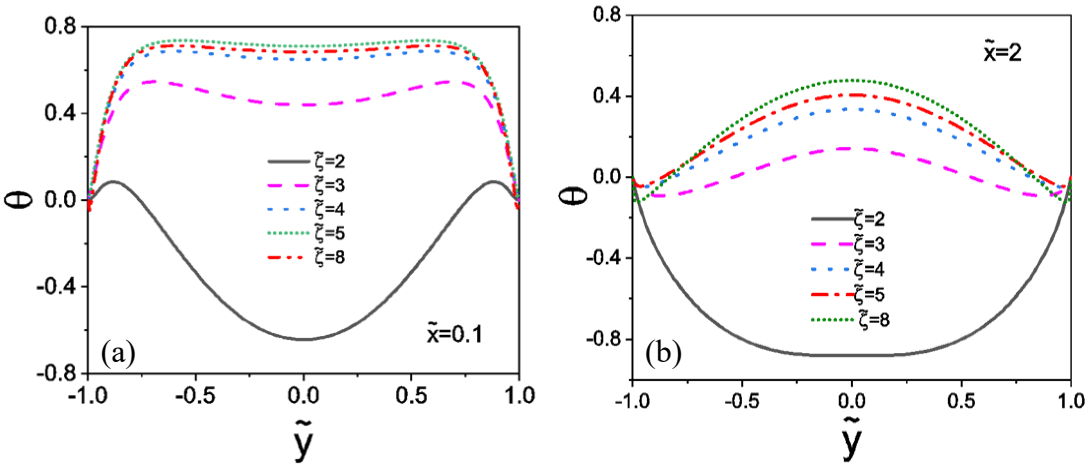

Fig. 5.4. Variation in temperature distribution along the transverse dimensionless coordinate axis $\tilde{y}$ for different values of surface potential at a fixed value of $\tilde{k} = 10,\ \Lambda = -1, \tilde{\varepsilon}\widetilde{W}\iota_{\mathrm{k}}^{2} = 2\,, Pe = 3,\ Sp = 1$, and Br =0.1 for (a) $\tilde{x} = 0.1$ and (b) $\tilde{x} = 2$

The effect of nontrivial interplay between the surface charging and the confluence of heat transfer is illustrated in Figs. 5.4(a)-5.4(b). We observe that at both the axial locations, with the increase in surface potential, the wall temperature gradient increases. As explained in previous section, the surface potential distinctly influences the velocity gradient near the wall. Therefore, with enhancement in $\tilde{\zeta}$, the advective fluid transport is more dominant. That, in turn, causes the alteration in temperature gradient near the wall. This leads to the convective heat transfer to occur at much faster rate. Therefore, an increasing strength of $\tilde{\zeta}$ results in progressive increment in the thermal entrance length. In contrast, we observe that at a lower $\tilde{\zeta}$, the volumetric heat source is more dominant.

As a result, the bulk mean temperature exceeds than that of wall temperature. That, in effect, reduces the temperature difference between the bulk and wall temperature to such

an extent that the temperature gradient becomes negative. Therefore, at a lower $\tilde{\zeta}$, the thermally fully developed state occurs at a much shorter axial distance from the inlet.

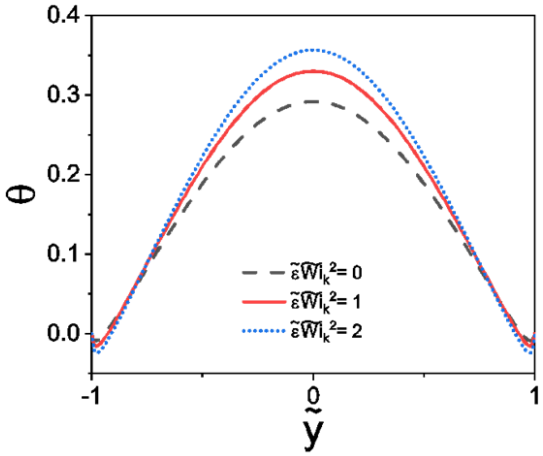

Fig. 5.5. Variation in temperature distribution along the transverse microchannel axis for different values of viscoelastic set $\tilde{\varepsilon}\widetilde{W}\iota_k^2$ at $\tilde{x}$=2 for $\tilde{k} = 10, \tilde{\zeta} = 5,\ \Lambda = -1, Pe = 3,\ Sp = 1$, and Br =0.1.

In Fig.5.5, we illustrate the influence of $\tilde{\varepsilon}\widetilde{W}\iota_k^2$ on the temperature distribution at specific axial location $\tilde{x}$=2. Here we found that for increasing values of $\tilde{\varepsilon}\widetilde{W}\iota_k^2$, the wall temperature gradient progressively increases from the channel wall to the core. We attribute this observation to the corresponding enhancements in the velocity gradient observed for increasing $\tilde{\varepsilon}\widetilde{W}\iota_k^2$. That, in turn, causes a gradual thinning of the boundary layer thickness and therefore concomitant enhancement in the heat transfer. We find that for increasing values of the viscoelastic parameter, the dimensionless temperature gradient tends to decrease with respect to that of the Newtonian case at $\tilde{\varepsilon}\widetilde{W}\iota_k^2 = 0$.The underlying physics is that increasing $\tilde{\varepsilon}\widetilde{W}\iota_k^2$ results in an increase in the flow velocity. This tendency is evident due to the inherent shear thinning effect associated with the higher value of $\tilde{\varepsilon}\widetilde{W}\iota_k^2$.Therefore an increase in flow velocity ensures higher convective heat transfer, which lowers the local fluid's temperature (T). As the value of T decreases, the magnitude of (T-T_W) increases, and therefore enhancing the value of the wall temperature gradient.

5.2.2 Nusselt number distribution and heat transfer characteristics

This section delineates the variation of local and average Nusselt numbers along the microchannel to quantify convective heat transfer performance under thermally developing flow of sPTT viscoelastic fluids subjected to combined electroosmotic and pressure-driven forces. The analysis captures the coupled influence of nonlinear

electrokinetics, fluid elasticity (Weissenberg number), and axial conduction on the evolution of the thermal boundary layer, thereby providing critical insights into the spatial modulation of heat transfer coefficients. Fig. 5.6(a) shows the variation of the local Nusselt number along the length of the microchannel for various values of Pe, whereas, Fig. 5.6(b) shows corresponding variation for different magnitudes of viscoelastic set (while the other pertinent parameters are given in the caption).In general, from the inlet of the channel, the local Nusselt number gradually decays along the axial direction until a particular axial location, where a sudden discontinuity in the local Nusselt number profile is observed.

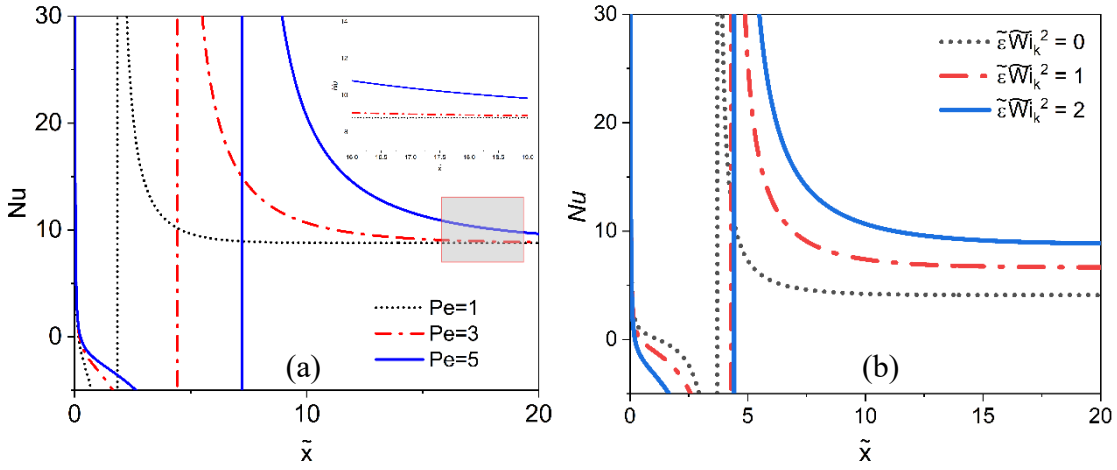

Fig. 5.6. Variation of local Nusselt number along the microchannel at $\tilde{k} = 10, \tilde{\zeta} = 5,\ \Lambda = -1,$ Sp = 1, and Br =0.1 for varying (a) Peclet numbers and at $\tilde{\varepsilon}\widetilde{W}i_k^2 = 2$; (b) $\tilde{\varepsilon}\widetilde{W}i_k^2$ for $Pe = 3$.

We attribute this behavior to the increase in fluid temperature in the thermal entrance region owing to the gradual heat transfer from the wall to the liquid and the heat generation due to viscous dissipation and Joule heating. That, in consequence, leads to an increase in the bulk mean temperature of the fluid and, therefore, a subsequent reduction in the local Nusselt number value. Now, nearer to the point of discontinuity, the bulk mean temperature approaches that of the wall temperature yielding. Therefore, we observe a bifurcation region in the local Nusselt number distribution that can be realized by examining Eq. (5.8). However, beyond the region of discontinuity, the volumetric heat generation sources primarily contribute toward increasing the fluid temperature. As a result, it generates a wall heat flux from the fluid to the microchannel walls. That, in turn, causes a gradual decrement in the local Nusselt number value till an axial threshold position, beyond which it becomes axially invariant, indicating a thermally fully developed region. In the thermally fully developed region, the heat transferred to the fluid from the walls is balanced continuously with the volumetric heat

generation sources. Accordingly, thermal entrance length may be defined as the axial distance from the channel inlet beyond which the local Nusselt number shows an axial invariance.

It is inferred from the Fig. 5.6(a) that the thermal entrance region gets more extended at higher values of the Peclet number. A gradual increment in the Peclet number slowly diminishes the diffusion strength with respect to the advective strength. Consequently, there is a delay in the development of the thermal boundary layer. In contrast, in the fully developed region, the local Nusselt value does not vary much with increasing *Pe*, as it asymptotically converges to a specific value.We observe from Fig. 5.6(b) that the local Nusselt number increases with $\tilde{\varepsilon}\widetilde{W}\iota_k^2$. This is because an increasing value of $\tilde{\varepsilon}\widetilde{W}\iota_k^2$ is associated with the strong shear thinning effect in viscosity that attenuates the velocity distribution across the microchannel, leading to an additional reduction in the bulk fluid temperature. In effect, the temperature difference between the wall and the bulk flow gradually reduces.

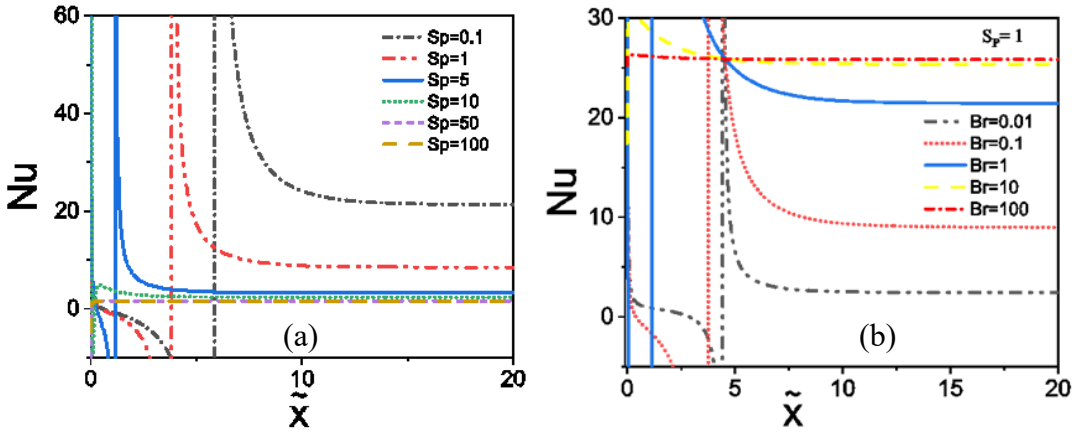

Fig. 5.7. Variation of the local Nusselt number along the microchannel axis$\tilde{x}$ for different values of (a) Sp and at fixed value of Br $= 0.1$; (b) Br at $Sp = 1$. Results are shown at $\tilde{k} = 10, \tilde{\zeta} = 5,\ \Lambda = -1,\ Pe = 3$, and $\tilde{\varepsilon}\widetilde{W}\iota_k^2 = 2$.

Fig. 5.7(a) depicts the variation in the local Nusselt number along the axial length with parametric variations inSp , while Fig. 5.7 (b) shows corresponding results for various *Br*. The other pertinent parameters are mention in the caption. We found that there is a gradual reduction in the local Nusselt number value for increasing Sp. In general, an increase in the Joule heating parameter continuously adds heat to the bulk flow, which causes the bulk mean temperature to exceed the constant wall temperature at a faster rate. As a result, the fluid becomes more homogenized. Such homogeneity significantly diminishes the temperature gradient near the walls, thereby leading to a gradual reduction

in heat transfer. Interestingly, for the extremely high value of Joule heating ($Sp = 100$), the bulk mean temperature of fluid immediately exceeds the wall temperature as soon as it enters the microchannel and thus quickly attains the thermally developed regime hence corresponding discontinuity in *Nu* variation does not occur.

We found from Fig. 5.7(b) that since *Br* is dependent on the velocity gradient near the wall, with the increase in viscous dissipation an appreciable enhancement in the fluid temperature is found near the wall than in the core region. Hence, in the upstream region, there is a substantial rise in the bulk mean temperature, which minimizes the difference between the bulk mean and wall temperature. Hence, the discontinuity in the variation of *Nu* occurs at the smaller value of $\tilde{x}$ near the upstream region. However, the contrasting behaviour is observed in the downstream region. As such, increasing values of *Br* cause a steady rise in the temperature gradient at the wall that augments the convective heat transfer rate, leading to an enhancement in the Nusselt number value. At a larger viscous dissipation (Br =100), excessive heat is added to the fluid at the entrance region of the microchannel. The bulk mean temperature rises progressively, thereby eliminating the discontinuity in the Nusselt number variation. The flow is thermally fully developed at a very shorter axial distance as large viscous dissipation involves intense volumetric heating. It is important to note here that the effect of viscous dissipation on heat transfer is prominently observed at a lower value of Joule heating. In Figs.4.7(a)-(c), we delineate the effect of imposed pressure gradient on the local Nusselt number distribution along the microchannel axis for varying Λ. The other parameters are given in the caption.

We find from Fig.5.8(a) that for a favorable pressure gradient, there is a progressive enhancement in the thermal entrance length and also the magnitude of the Nusselt number. The underlying physics is that with an increase in imposed pressure gradient, there is an augmentation in the advective transport of the bulk fluid at any axial location of the microchannel . This results in the thinning of the thermal boundary layer thickness, which causes a net delay in the development of the thermal boundary layer. The overall effect yields an increased thermal entrance length, and hence corresponding augmentation in the heat transfer rate. In Fig 5.8(b), we observe that the adverse pressure gradient opposes the electrokinetic actuation, causing a drop in the advective transport of the bulk flow. As a result, the fluid motion slows down, causing a decrement in the convective heat transfer rate. The overall consequence is a considerable contraction of the thermal entrance length.

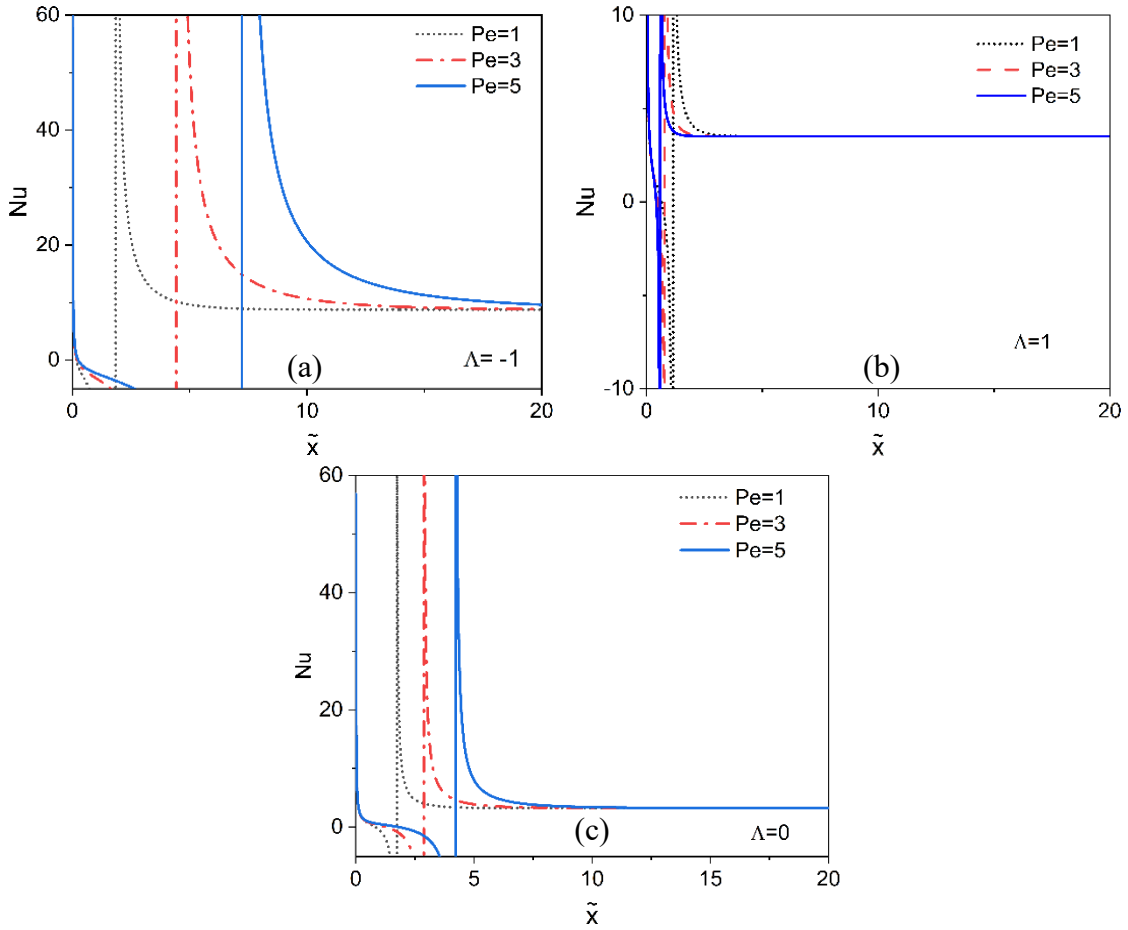

Fig. 5.8.. Variation of the local Nusselt number across the microchannel for varying Pe at (a) Λ = -1, (b) Λ = 1, and (c) Λ = 0. The other parameters are $\tilde{k} = 10, \tilde{\zeta} = 5, \tilde{\varepsilon}\widetilde{W}\iota_{\mathrm{k}}^2 = 2$, Sp = 1, and Br =0.1.

In Fig.5.8(c), we depict the variation in the local Nusselt number for pure electroosmotic flow (Λ= 0). We see a distinct increase in the thermal entrance length and the local Nusselt number value. This is due to the plug-like velocity profile for pure electroosmotic flow, which causes a substantial increase in the bulk advective transport of ions in the EDL region. That results in an enhancement in the local fluid velocity within the EDL, increasing the convective heat transfer from the wall to the bulk flow. In consequence, a larger value of the thermal entrance length with a higher local Nusselt number value.

Finally, in Fig. 5.9, we show the variation in the fully developed Nusselt number (defined as $Nu_{FD} = \lim_{x\to\infty} Nu(x)$) as a parametric function of $\tilde{\varepsilon}\widetilde{W}\iota_{\mathrm{k}}^2$ and $\tilde{\zeta}$. Figure. 5.9 demonstrates the operating regime of the set of input parameters for which the heat transfer is maximum. A typical observation from Fig.5.9. is that as the value of $\tilde{\varepsilon}\widetilde{W}\iota_{\mathrm{k}}^2$ is increased, heat transfer enhancement is noted for a microchannel with higher $\tilde{\zeta}$. Hence, along the plane of heat transfer, the peak heat transfer is noticed at $\tilde{\zeta} = 10$,

$\tilde{\varepsilon}\widetilde{W}\iota_{\mathrm{k}}^2 = 4$, although the minimum heat transfer regime is always for the Newtonian fluid at $\tilde{\zeta} = 2$. We, therefore, see that it is possible to maximize the heat transfer rate for a specific combination of degree of surface charging and the rheological properties of the fluid. From the industrial application perspective, one may alternatively chose the parametric set $\left(\tilde{\zeta}, \tilde{\varepsilon}\widetilde{W}\iota_{\mathrm{k}}^2\right)$ for the heat transfer modulations.

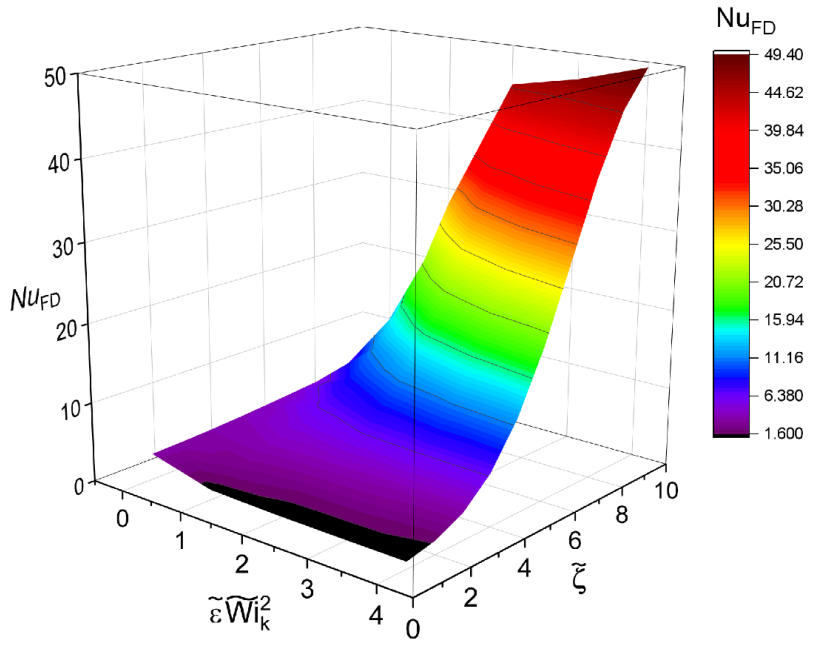

Fig. 5.9 Variations in fully developed Nusselt number as a function of viscoelastic parameter $\tilde{\varepsilon}\widetilde{W}\iota_{\mathrm{k}}^2$ and $\tilde{\zeta}$ at $\tilde{k} = 10, \Lambda$=-1, $Pe = 3, Sp = 1$, and $Br = 0.1$.

5.2.3 Entropy generation analysis for thermally developing flow

One may estimate the fraction of thermodynamic irreversibilities in any physical system through entropy generation analysis. The entropy generation is a direct function of lost available work. In any process, the efficiency loss is attributed to friction, chemical reaction, heat, and mass transfer.[42] Therefore, exergy loss due to entropy generation should be minimized to achieve optimum process design. Based on the local thermodynamic equilibrium of linear transport theory, the local total entropy generation S_T can be defined as [36], [138]

$$S_T = S_{\theta H} + S_{\theta V} + S_{\theta J} \tag{5.10}$$

Here, $S_{\theta H}$ is the local entropy generation due to heat transfer, $S_{\theta V}$ is the local entropy generation due to fluid friction, and $S_{\theta J}$ is the local entropy generation due to Joule heating effect. We express the dimensionless form of the total entropy generation based on the local thermodynamic equilibrium of linear transport theory as[138]

$$S_T = \frac{1}{(\theta+T_L)^2}\left\{\left(\frac{\partial\theta}{\partial\tilde{x}}\right)^2 + \left(\frac{\partial\theta}{\partial\tilde{y}}\right)^2\right\} - \frac{NuBr}{\theta}\left\{\left(\frac{\partial u}{\partial\tilde{y}}\right)^2\right\} - S_p Nu\frac{E_x^2}{(\theta+T_L)}, \quad (5.11)$$

where $T_L = \frac{T_W}{T_B - T_W}$ is the temperature ratio. The global total entropy generation over the flow domain (Ω) is given by

$$S_{Tg} = \int_{\Omega} S_T d\Omega \quad (5.12)$$

In this research, we theoretically estimate the electrohydrodynamic entropy generation for the convection of viscoelastic fluids through the microchannel. This is accomplished by determining the velocity and temperature fields and establishing different entropy parameters in a non-dimensional form.,

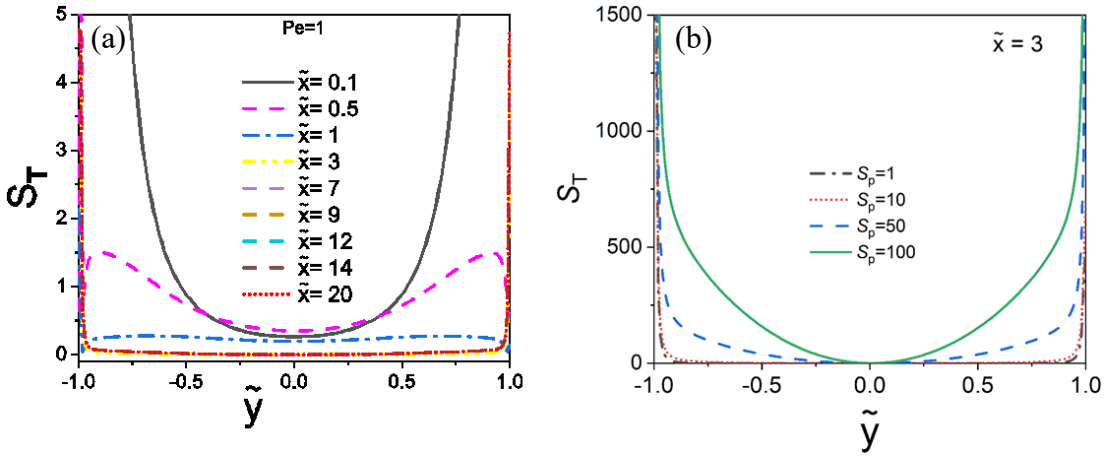

Fig. 5.10. The variation in total entropy generation across the microchannel for (a) different axial locations and at fixed values of $Pe = 1, Sp = 1, Br = 0.1$; (b) different values of the Joule heating parameters (Sp) and at $Pe = 3, Br = 0.1, \tilde{x} = 3$ at $\tilde{k} = 10, \Lambda$=-1, $\tilde{\zeta} = 5$, and $\tilde{\varepsilon}\widetilde{W}i_k^2 = 2$.

Fig. 5.10(a) shows the dimensionless total entropy generation as a function of the dimensionless transverse coordinate y, for different $\tilde{x}$. In general, the characteristics of total entropy generation show reflection symmetry about the centreline of the channel. The overall entropy generation reaches its maximum value near the confinement walls at all axial locations. This is due to the changes in the magnitudes of the velocity and temperature gradients, which generally encounter near the confinement walls. However, the total entropy generation is minimum at the centreline of the channel, where the changes in thermal and velocity gradients are the least. The functional dependence of S_T with S_p is shown in Fig. 5.10(b) as its variation along the microchannel axis at a specific axial location of $\tilde{x} = 3$. Apart from the usual feature of the total entropy generation curve, which shows a universal trend, we find that total entropy generation increases with

an increase of S_p. We attribute this to the enhanced thermal irreversibility owing to Joule heating effects ($S_{\theta J}$).

Fig. 5.10(a) shows the dimensionless total entropy generation as a function of the dimensionless transverse coordinate y, for different $\tilde{x}$. In general, the characteristics of total entropy generation show reflection symmetry about the centreline of the channel. The overall entropy generation reaches its maximum value near the confinement walls at all axial locations. This is due to the changes in the magnitudes of the velocity and temperature gradients, which generally encounter near the confinement walls. However, the total entropy generation is minimum at the centreline of the channel, where the changes in thermal and velocity gradients are the least. The functional dependence of S_T with S_p is shown in Fig. 5.10(b) as its variation along the microchannel axis at a specific axial location of $\tilde{x} = 3$. Apart from the usual feature of the total entropy generation curve, which shows a universal trend, we find that total entropy generation increases with an increase of S_p. We attribute this to the enhanced thermal irreversibility owing to Joule heating effects ($S_{\theta J}$).

One may directly relate this observation with the heat transfer rate, which shows the Joule heating effect decays the convective heat transfer and, in effect, increases the total entropy generation within the microchannel. To understand the relative dominance of thermal irreversibility over the total system's irreversibility, we have computed the dependence of Bejan number along the microchannel. The Bejan number is defined as,[36]

$$Be = \frac{\int_{\Omega} S_{\theta H} d\Omega}{\int_{\Omega} S_T d\Omega} \tag{5.13}$$

The physical significance of $Be$is detailed in the literature as, when $Be > 0.5$, heat transfer irreversibility is dominant, while when Be is less than 0.5, fluid friction irreversibility is dominant.

Fig.s 5.11(a)-(b) shows the axial dependence of Be as a function of $\tilde{\varepsilon}\widetilde{W}i_{\mathrm{k}}^2$ for two representative values of $Sp = 1$ (Fig. 5.11a) and $Sp = 10$ (Fig. 5.11b), while the other parameters are given in the caption. We observe that the effect of Joule heating causes the system to be dominated with the heat transfer irreversibility, since for both of the curves $Be > 0.5$. At the entrance region of the microchannel, the thermal boundary layer

development results in progressive enhancements in the wall temperature gradient, yielding dominance of heat transfer irreversibility over the fluid friction. In turn, tending the Bejan number value closer to one.

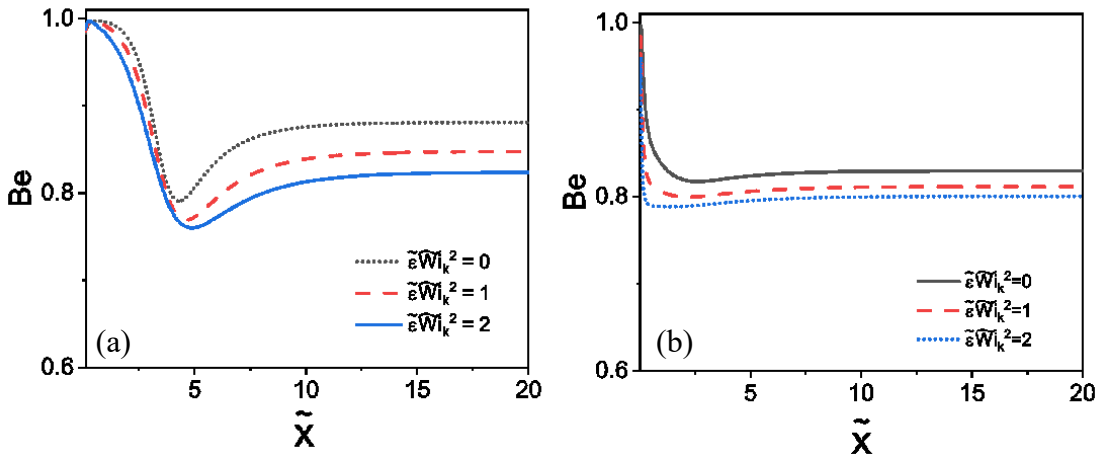

Fig. 5.11. Variation of the Bejan number across the microchannel for varying viscoelastic set $\tilde{\varepsilon}\widetilde{W}\iota_k^2$at $\tilde{k} = 10, \Lambda$=-1, $\tilde{\zeta} = 5, Pe = 3, Br = 0.1$ for (a) $Sp = 1$ and (b) $Sp = 10$.

In contrast, gradual reduction in surface temperature gradient culminates a drop in Be to minima away from the inlet region. Beyond the minimum point, the volumetric heat generation due to Joule heating and viscous dissipation again raises the wall temperature gradient. As a result, the value of Be increases till an axial threshold position is reached where there is an axial invariance in the Bejan number is observed corresponding to the thermally fully developed region. Further, it is observed that for increasing $\tilde{\varepsilon}\widetilde{W}\iota_k^2$, results in a reduction in the Bevalue. The physical explanation for this behaviour is that higher values of $\tilde{\varepsilon}\widetilde{W}\iota_k^2$ induces shear thinning effect on the flow. That, in turn, reduces near wall velocity gradient, leading to a lower heat transfer rate. We found that the drop in Be from the entrance region for $Sp = 1$ is more than for $Sp = 10$. A large volumetric heat generation occurs at a higher value of Sp, that helps in reaching the thermally developed state quickly, thus ceasing the thermal entry length.

In Fig. 5.12, we show it is possible to minimize the overall thermodynamic irreversibility through the combined consequences of fluid rheology and the surface charge modulation of the microchannel. We see that the degree of surface charging plays an inverse relationship with the viscoelastic set $\tilde{\varepsilon}\widetilde{W}\iota_k^2$ in exhibiting the fully developed total entropy generation of the microchannel. As such, one may enter a maximum thermodynamic irreversibility plane for reducing the values of $\tilde{\zeta}$ with an increased shear thinning

characteristics of the fluid. Therefore, we may record here that it is possible to customize the total entropy generation of the system for every choice of $\tilde{\zeta}$ and $\tilde{\varepsilon}\widetilde{W\iota}_{\mathrm{k}}^{2}$. The current research results serve as a starting point for the design of innovative micro heat transfer devices, where understanding the key influencing element in the development of total entropy is essential. Creating techniques to boost thermodynamic efficiency by limiting the microsystem's total entropy production in all such applications may be necessary.

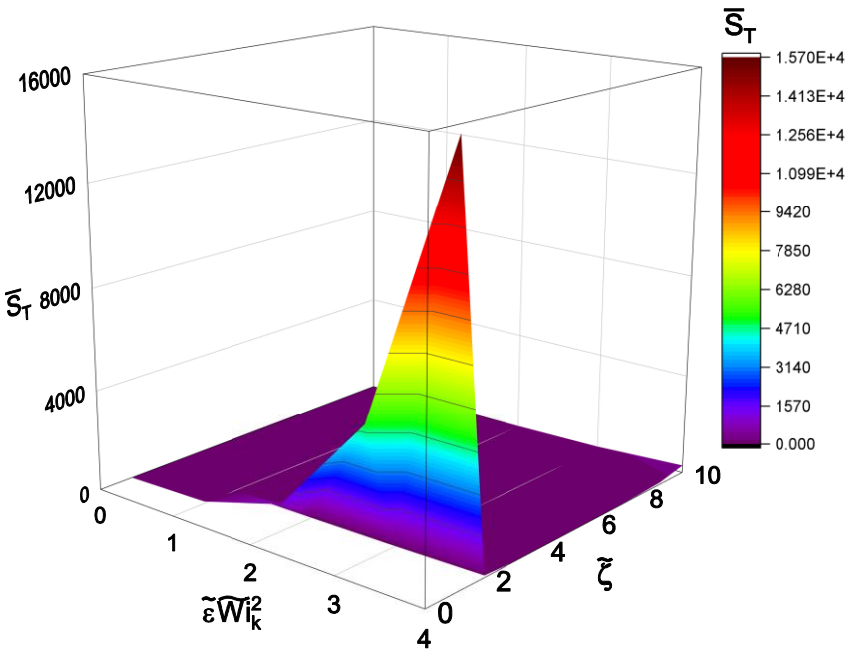

Fig. 5.12. Variations in total fully developed entropy generation as a function of viscoelastic parameter $\tilde{\varepsilon}\widetilde{W\iota}_{\mathrm{k}}^{2}$ and $\tilde{k}$ at $\tilde{\zeta} = 5, \tilde{k} = 10, \Lambda$=-1, $Pe = 3, Sp = 1$ and $Br = 0.1$.

Chapter 6. Thermally developing streaming potential mediated pressure driven transport of sPTT fluids in a microchannel

In this chapter, a detailed investigation is undertaken to understand the thermally developing transport characteristics of viscoelastic fluids, governed by the simplified Phan–Thien–Tanner (sPTT) model, in microchannel configurations where flow is driven by self-generated streaming potential fields, where the interplay between ionic convection, induced electric fields, and non-Newtonian rheology governs both momentum and thermal energy transport.

6.1 Mathematical formulation

6.1.1 Physical Model

We consider a steady, incompressible, two-dimensional, pressure-driven flow of a viscoelastic fluid described by the simplified Phan-Thien–Tanner (sPTT) model, containing a symmetric binary electrolyte ($z^+ = z^- = z$, where z denotes the ionic valency), through a long, narrow, slit-like microchannel. The microchannel comprises two parallel walls, maintained at a constant temperature T_w, as illustrated in Fig. 6.1. The channel height is 2H, and its length is L, such that $L \gg H$. The width is assumed to be much larger than both H and L, justifying the use of a quasi-two-dimensional formulation. A Cartesian coordinate system is adopted, with the axial coordinate X directed along the channel length and the transverse coordinate Y oriented perpendicular to the walls. The origin is located at the mid-height of the channel. The flow is driven by a constant axial pressure gradient, $-dP/dX$. In microfluidic systems, pressure-driven transport of electrolytic solutions naturally induces charge separation due to ionic advection, resulting in the development of an electric field along the axial direction. This generates a streaming potential Ex, which acts to oppose the pressure-driven flow, as indicated in Fig. 6.1. This electrohydrodynamic coupling, even in the absence of an externally applied electric field, is intrinsic to confined electrolyte flows and significantly influences the flow dynamics.[55], [138]. The fluid is assumed to have temperature-independent thermophysical properties, and the electrolyte ions are modeled as point charges in a

dilute solution. The channel walls possess a uniform zeta potential ζ, leading to the formation of electrical double layers (EDLs) near the surfaces. The interaction between EDL-induced electrokinetic phenomena and the viscoelastic flow behavior governed by the sPTT model plays a crucial role in the transport characteristics.[48]

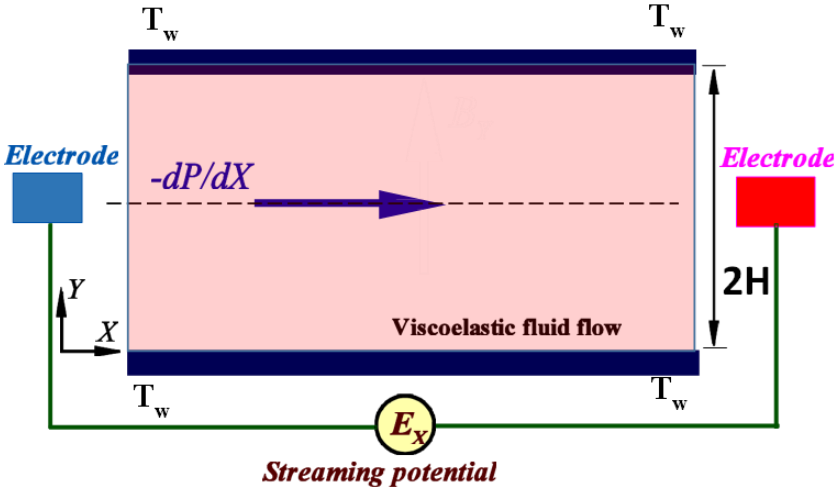

Fig. 6.1. Schematic diagram of the set-up showing streaming mediated pressure driven sPTT fluid through a rectangular microchannel whose wall are maintain at constant temperature Tw.

6.1.2 Temperature field for thermally developing flow

To obtain the temperature distribution, we solve the thermal energy equation utilizing the velocity distribution solution. This equation is influenced by four potential sources of energy fluxes: convective transport through the fluid, conduction of moving fluid particles, Joule heating effects from the induced streaming potential field, and viscous dissipation. Hence, for a fully developed pressure-driven flow with constant wall temperature boundary conditions, the energy equation is expressed as [55]

$$(\rho C_p)U\frac{\partial T}{\partial X}=\kappa\left(\frac{\partial^2 T}{\partial X^2}+\frac{\partial^2 T}{\partial Y^2}\right)+\eta_v\left(\frac{\partial U}{\delta Y}\right)^2+S_j, \tag{6.1}$$

where T is the temperature, ρ is the density, C_p is the heat capacity, and κ is the thermal conductivity. The Joule heating contributes volumetric heat generation S_j, while viscous dissipation is represented by $\eta_v\left(\frac{\partial U}{\partial Y}\right)^2$. Assuming a weak advective effect on ionic species transport, S_j is computed as $S_j=\sigma_e E_X^2$. We make Eq. (26) dimensionless, to obtain[55]

$$\left(Pe\frac{U_{ref}}{U_{avg}}\right)\bar{u}(\bar{y})\frac{\partial\theta}{\partial\bar{x}}=\left(\frac{\partial^2\theta}{\partial\bar{x}^2}+\frac{\partial^2\theta}{\partial\bar{y}^2}\right)-Br\left(\frac{\partial\bar{u}}{\partial\bar{y}}\right)^2-S_{peff} \tag{6.2}$$

The dimensionless variables for Eq. (27) are: $\bar{x}=X/H$, $U_{ref}=-(dp/dX)H^2/\eta_v$ dimensionless temperature $\theta=(T-T_w)/(T_i-T_w)$. The other dimensionless numbers are: thermal Peclet number $Pe=U_{ref}H/(\kappa/\rho C_p)$, Brinkmann number $Br=\eta_v U_{ref}/\kappa(T_w-T_i)$ represents the contribution resulting from viscous dissipation. Here, $S_{p_{eff}}=S_pE^2$ is the effective Joule heating parameter, where $S_p=H^2S_j/\kappa(T_w-T_i)$.

Equation (6.2) is subjected to the following sets of boundary conditions in dimensionless form:

$\theta|_{\bar{x}=0} = 1 \quad \forall \quad 0\le\bar{y}\le 1$ 6.3(a)

$\theta|_{\bar{y}=0} = 0 \ \forall \quad 0<\bar{x}<+\infty$ 6.3(b)

$\frac{\partial\theta}{\partial\bar{y}}|_{\bar{y}=0}=0\ \forall\ 0<\bar{x}<+\infty$ 6.3(c)

$\theta<\infty$ as $\bar{x}\to+\infty \ \ \forall\ 0\le\bar{y}\le 1$ 6.3(d)

We have used a finite volume based numerical method for obtaining numerical solution of the energy equation to obtain the dimensionless temperature across various axial locations of the microchannel. On the other hand, an iterative method is used for calculating the streaming potential field by continuously satisfying electroneutrality constraint [42].

The expression for bulk mean temperature θ_b at any axial location of microchannel is given as,

$$\theta_b(x)=\frac{\int_{-1}^{1}u(\bar{y})\theta(\bar{x},\bar{y})d\bar{y}}{\int_{-1}^{1}u(\bar{y})d\bar{y}} \tag{6.4}$$

Finally, by invoking the steady state energy balance between the walls and the bulk fluid temperature, the expression for the Nusselt number may be obtained as,[55]

$$Nu=\frac{1}{\theta_b}\frac{\partial\theta}{\partial\bar{y}} \tag{6.5}$$

6.2 Results and Discussions

To validate our numerical model, we compare our semi-analytical findings for streaming potential-mediated pressure-driven flow of a Newtonian fluid in parallel plate microchannels with a previously established semi-analytical solution documented in Dey *et al* [78]. Fig 6.2 compares temperature variation across the microchannel for the parameters mentioned in the caption. We clearly observe that our results are in good agreement with the data shown in Dey *et al*.[137] To integrate practical considerations into our physical description, we model the non-Newtonian fluid as a representative biofluidic sample. We characterize its thermophysical properties at a standard temperature T=300 K as: density $\rho \approx 10^3\, kg/m^3$, fluid viscosity $\eta_v \sim 10^{-3} - 10^{-2}$ Pa s, permittivity $\varepsilon_p \approx 702.24 \times 10^{-12}\, C^2/Jm$ and the Boltzmann constant $k_B = 1.38064852 \times 10^{-23} m^2 kgs^{-2} K^{-1}$.

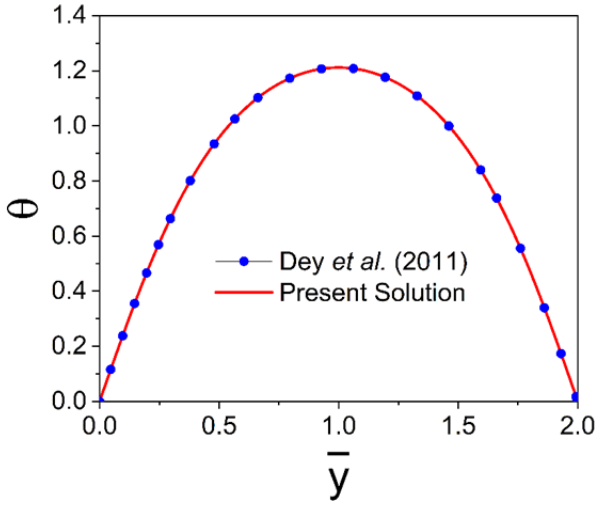

Fig. 6.2. Comparison results between the dimensionless temperature variation across the microchannel with the published results of Dey *et al*.[137] for $\varepsilon \bar{W}i_k^2 = 0$ at $\bar{k} = 5$, and $\bar{\zeta} = 5$

Additionally, when considering the aforementioned parameters, the dimensional zeta potential ranges from 0 to 50 mV.[48] The analysis incorporates several dimensionless parameters, including the ratio of the half-height of the confinement to the Debye length ($\bar{k}$), dimensionless zeta potential ($\bar{\zeta}$), thermal Peclet number (Pe), effective Joule heating parameter (Sp_{eff}), and the viscous dissipation parameter (Br). For thermally developing flows, we have considered, $Pe = 1-3, Br = 0.01-10, Sp_{eff} = 0-10$. For a microchannel, the length and width generally varies of the order of L≈ W≈ O($10^3 \mu m$), whereas the channel height H≈ $O(10\mu m)$, and hence, the relevant dimensionless

electrokinetic parameter value throughout the analysis is kept in the range $\bar{k} = 10 - 40$ [55].

6.2.1 Thermal energy transport equation for thermally developing flow

We now explore how viscous dissipation factors influence temperature distribution within a narrow confinement as part of a thermally developing flow. Fig. 6.3 shows variation of dimensionless temperature (θ) across the microchannel axis $\bar{y}$ at various streamwise stations $\bar{x}$ for different values of *Br*, for the parameters given in the caption.

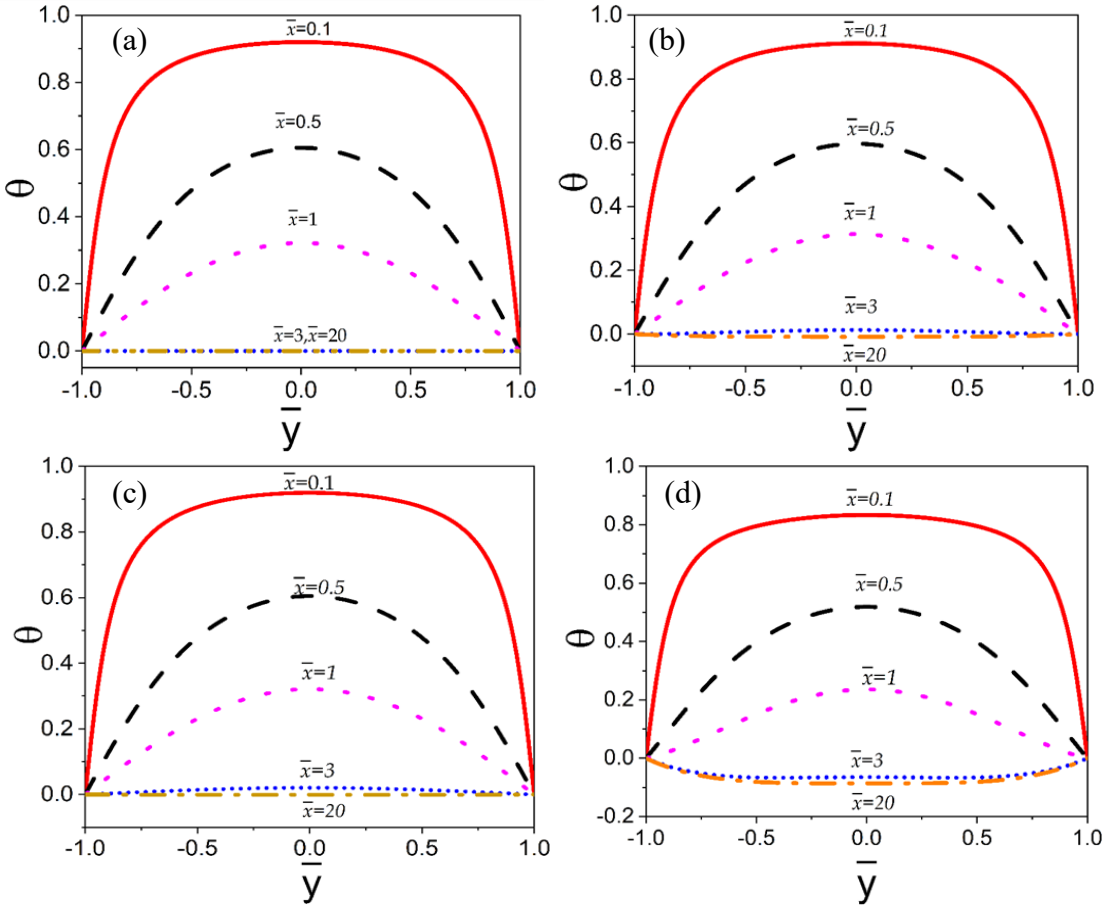

Fig. 6.3. Variation of dimensionless temperature (θ) across the microchannel axis $(\bar{y})$ at various streamwise stations $(\bar{x})$ for *Br*=(a) 0; (b) 0.01; (c) 0.1; (d) 1 at $\bar{\zeta} = 6$, $\bar{k}$=10, $\varepsilon\overline{W\iota}_k^2 = 1$, $Pe = 1$, and Sp_{eff}

The data presented in Fig. 6.3 reveals a nuanced pattern: dimensionless temperature progressively diminishes along the axial length, with intriguingly negative values emerging at specific axial locations. This phenomenon prompts a deeper exploration into its physical implications. Upon closer examination, we find that the increase in *Br*, which signifies enhanced viscous dissipation, introduces additional heat into the flow at its entrance. This influx of energy serves to reduce the temperature differential between the

wall temperature and the fluid temperature $(T_W - T)$. As a result, instances where the dimensionless temperature becomes negative suggest that, paradoxically, the fluid temperature surpasses the wall temperature. This counterintuitive observation highlights the complex interplay between viscous dissipation and temperature dynamics within confined flows. Moreover, a detailed analysis of Fig. 6.3(a)-(d) unveils a pivotal transition point at $\bar{x} = 5$, where a pronounced variation in the thermally developing region occurs. Beyond this juncture, the convective heat transfer rate begins to dwindle, signalling the onset of a thermally fully developed state. This transition to axially invariant temperature profiles marks a critical phase in the flow's thermal evolution.

Fig. 6.3(a)-(d) shows the distribution of θ across the microchannel axis at varying $\bar{x}$ for various Sp_{eff}. We observe that with increasing magnitudes of Sp_{eff} the magnitude of the dimensionless temperature decreases. This is because that on increasing Sp_{eff} enhances fluid temperature and promotes homogenization, but concurrently reduces the temperature gradient near the fluid-solid interface. This leads to a decrease in heat transfer rate as the magnitude of Joule heating increases. From Figs. 6.4(a)-(c), it's notable that θ is positive, indicating that at the entrance, the wall temperature exceeds the fluid temperature in the bulk flow. Although the temperature profile exhibits minimal variation for the four values of Sp_{eff} near the microchannel wall at axial locations $\bar{x} = 0.1$, $\bar{x} = 0.5$, and $\bar{x} = 1$, the dimensionless temperature gradient is still notably influenced by the parameter Sp_{eff}. Additionally, the variation at $\bar{x} = 3$ suggests that increasing negative values of θ relative to increasing values of Sp_{eff} indicate the predominance of the effective Joule heating. In Fig. 6.4(d), θ is negative for all values of Sp_{eff} and becomes more negative as the Joule hearing is triggered. From a physical perspective, negative temperature values arise because θ can only gradually become negative when T becomes increasingly greater than T_W, since $T_i < T_W$ and $\theta = T - T_W / T_i - T_W$. At $\bar{x} = 3$, it's observed that the flow ultimately reaches the thermal fully developed stage. Subsequently, at or after $\bar{x} = 3$, the temperature profile remains unchanged.

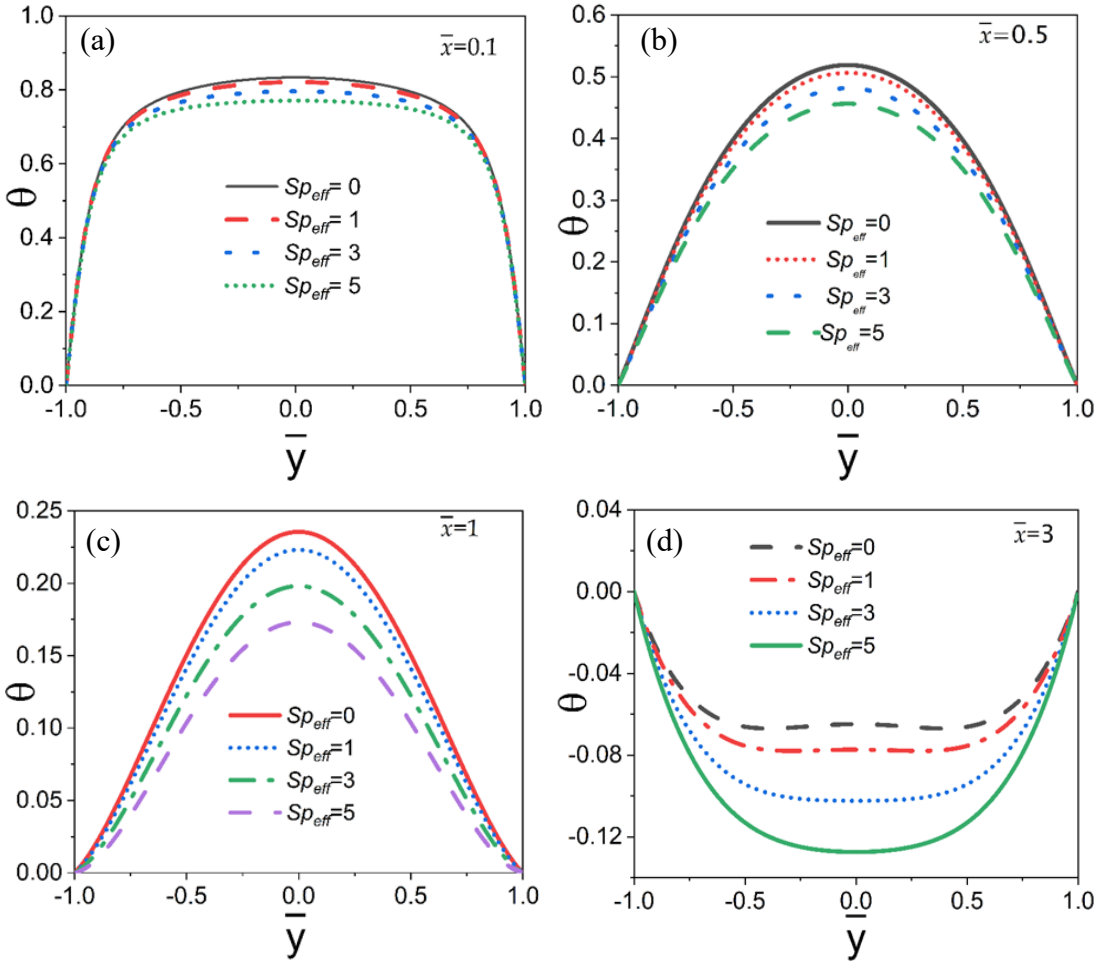

Fig. 6.4. Distribution of the dimensionless temperature across the microchannel at various axial locations for varying Sp_{eff} and at $\bar{\zeta} = 6$, $\bar{k}$=10, $\varepsilon\overline{Wi}_k^2$ = 1, Pe = 1, and Br = 1.

6.2.2 Nusselt number distribution and heat transfer characteristics

Fig. 6.5 shows the variation of the local Nusselt number along the microchannel for varying Sp_{eff} (Fig. 6.5a) and Br (Fig. 6.5b). We observe that the local Nusselt number exhibits a high value in the thermally developing region, gradually decreasing along the axial direction until it reaches a constant value in the thermally developed region. This decline in heat transfer rate is attributed to a decrease in the heat transfer coefficient, resulting from a reduction in the temperature gradient between the constant wall temperature and the flowing fluid. Consequently, the bulk temperature of the fluid (θ_b) steadily rises, leading to a thickening of the thermal boundary layer in the thermally developing region.

Eventually, this trend progresses to a point where the bulk mean temperature approaches the channel wall temperature, signifying a diminishing temperature difference, and

ultimately surpasses it. The equation for the Nusselt number (Eq. 6.5) reveals that the value of *Nu* corresponding to the axial point where T_m tends to T_w will inevitably exhibit a singularity. This occurs as the value of θ_b, which appears in the denominator of the expression for *Nu*, approaches zero.[55] This singularity is visually depicted by the discontinuity in the variation of *Nu* corresponding to that particular $\bar{x}$. We observe how the Joule heating effect influences the thermal behavior of electrokinetic flow. Both the heat transfer rate and *Nu* tend to decrease due to the Joule heating effect. Consequently, a higher Joule heating effect, indicated by the increased Sp_{eff}, elevates the bulk temperature, thereby reducing heat transfer performance. This can be explained by the fact that the rise in bulk fluid temperature homogenizes the fluid, leading to a reduction in the temperature gradient between the wall and the fluid interface.

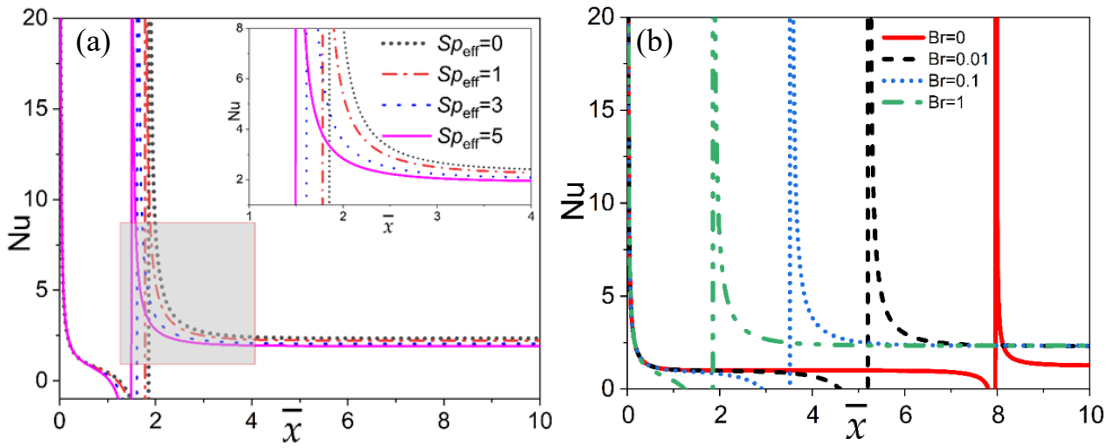

Fig. 6.5. Local Nusselt number variations along the axial length ($\bar{x}$) of the confinement for (a) various Sp_{eff} at *Br*=1; (b) different *Br* at $Sp = 1$. The other parameters are: $\bar{\zeta} = 6$, $\bar{k}$=10, $\varepsilon \overline{W} \iota_k^2 = 1$, $Pe = 1$

Fig. 6.5(a) depicts the streamwise variation of the local Nusselt number for varying, Sp_{eff} while the corresponding variations for different *Br* is shown in Fig.6.5(b). Apart from the usual signature of the *Nu* distribution, we observe that the heat transfer decreases due to the Joule heating effect. A higher Joule heating effect, indicated by the increased Sp_{eff}, raises the bulk temperature, thereby reducing heat transfer performance. [55] This occurs because the rise in bulk fluid temperature homogenizes the fluid, resulting in a reduction of the temperature gradient between the wall and the fluid interface. The higher Br value amplifies the viscous dissipation component, effectively narrowing the temperature gap between the channel wall and the bulk fluid. This phenomenon signifies an enhancement in heat transfer performance. It's worth noting that for shear thinning fluids, the impact

of higher Br values on the Nusselt number is more pronounced compared to Newtonian and shear thickening fluids. Given that sPTT fluid displays shear thinning characteristics, this results in a significant enhancement in heat transfer. Intense viscous dissipation leads to robust volumetric heating, facilitating complete thermal development over a shorter axial distance. Higher Br values accelerate the rate of thermal growth, thereby shortening the thermal entry length .Additionally, at larger Br, excessive heat is predominantly added at the entrance, eliminating the singularity in the variation of the Nusselt number. This suggests the formation of a thermally developed region closer to the entrance area. The effect of *Pe* on the heat transfer characteristics is shown in Fig. 6.6(a), whereas Fig. 6.6(b) shows the influence of $\varepsilon\overline{Wi_k}^2$ on the local Nusselt number distribution. The other parameters are mentioned in the caption.

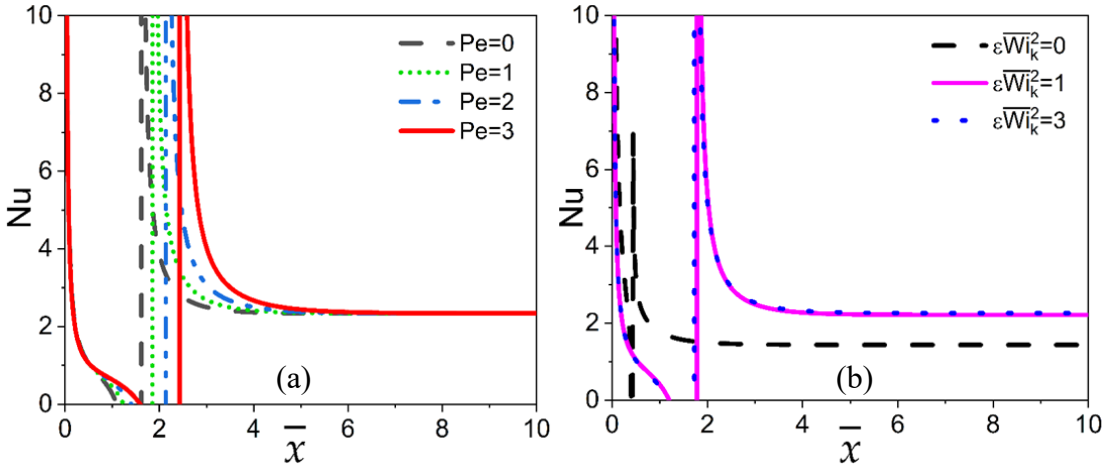

Fig. 6.6. The variation of the local Nusselt number across the microchannel length for various (a) *Pe* and at $Sp_{eff}=1$; (b) $\varepsilon\overline{Wi_k}^2$ and at $Pe=1$. The other parameters are: $\bar{\zeta}=6, \bar{k}=10, Br=1$.

Fig. 6.6(a) illustrates that the thermal entrance region expands notably with an increase in the Peclet number. However, variations in the *Pe* have no impact on the fully developed Nusselt number. The local Nusselt number profiles asymptotically converge to a certain constant value in a thermally fully developed region. A progressive increase in the *Pe* results in a gradual thinning of the thermal boundary layer due to the heightened advective transport strength relative to longitudinal diffusion strength. This slows down the growth of the thermal boundary layer, thereby expanding the thermal entry length with increasing values of *Pe*. However, in the thermally developed region, the rate of convective heat transfer remains constant, as the flow hydrodynamics and sources of volumetric heat generation remain unchanged. From Fig. 6.6(b), it is evident that

compared to the Newtonian fluid $\left(\varepsilon\overline{Wi_k}^2 = 0\right)$, the viscoelastic effect leads to an increase in heat transfer. Although increasing $\varepsilon\overline{Wi_k}^2$ does not result in a significant enhancement in Nu(x), this is due to the subtle impact of the operating range of other parameter sets on the overall augmentation in heat transfer. In general, an increase in $\varepsilon\overline{Wi_k}^2$ enhances the shear thinning effect, leading to a decrease in the bulk mean temperature of the fluid. This is attributed to the augmentation of advective bulk fluidic transport within the microchannel, resulting in the thinning of the thermal boundary layer thickness. Consequently, the thermal entrance region extends compared to the case where $\varepsilon\overline{Wi_k}^2 = 0$.

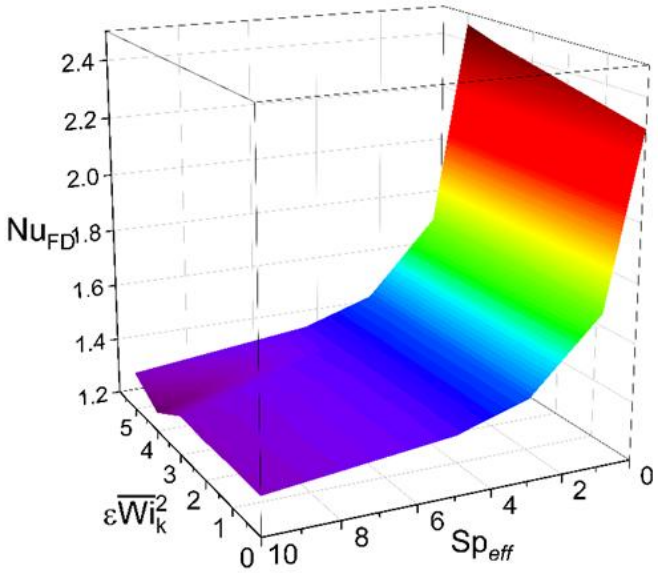

Fig. 6.7. Variation of the fully developed Nusselt number as parametric functions of $\varepsilon\overline{Wi_k}^2$ and Sp_{eff} for $\overline{\zeta} = 6, \overline{k} = 10, Pe = 1,$ and $Br = 1$.

To demonstrate the combined electrohydrodynamic implications on global heat transfer characteristics, we have included an exemplary case representing the combined effect of $\varepsilon\overline{Wi_k}^2$ and Sp_{eff} (associated with streaming potential *E*) on the fully developed Nusselt number, Nu_{FD} in Fig. 6.7. Mathematically, we define $Nu_{FD} = \lim_{x\to\infty} Nu\left(\overline{x}\right)$.[36] A preliminary analysis of Fig. 6.7 indicates that the convective heat transfer rate can be optimized for specific combinations of Sp_{eff} and $\varepsilon\overline{Wi_k}^2$. Although the impact of the viscoelastic parameter $\varepsilon\overline{Wi_k}^2$ on Nu_{FD} may be negligible individually, its collective

effect enhances the convective heat transfer rate and ultimately Nu_{FD}. From the Fig. Fig.6.7, it is evident that the optimal regime for Nu_{FD} lies within a small range of Sp_{eff} values. However, for an effective heat transfer rate, the corresponding regime is consistently located at a unique axial location where $\bar{\zeta} \approx 6$ and $\varepsilon \overline{Wi_k}^2 \approx 2$. This suggests that the synergies between rheology and interfacial electrokinetics play a crucial role in controlling Nu_{FD}. Consequently, the insights provided here can be strategically applied to advance more effective cutting-edge electromechanical devices relevant to thermal applications in both biological and non-biological domains.

6.2.3 Exergy Analysis

In physical systems, analyzing entropy generation helps understand irreversible thermodynamic processes. Minimizing entropy generation optimizes thermal system design by conserving system energy. We investigate the relationship between entropy generation rate and exergy loss, focusing on fundamental thermal transport mechanisms during combined streaming potential-mediated pressure-driven flow in microchannels. Fluid friction and heat transfer contribute to total entropy generation, analyzed through linear transport theory to derive dimensionless parameters.

Local entropy generation due to fluid friction is given by,[55]

$$S_f = \gamma \left[2\left\{ \left(\frac{\partial \bar{u}}{\partial \bar{x}} \right)^2 + \left(\frac{\partial \bar{v}}{\partial \bar{y}} \right)^2 \right\} + \left(\frac{\partial \bar{u}}{\partial \bar{x}} + \frac{\partial \bar{v}}{\partial \bar{y}} \right)^2 \right] \tag{6.6}$$

Here, the parameter γ is the irreversibility distribution ratio and is taken as 10^{-4}. Local entropy generation due to heat transfer is given by,

$$S_H = \left(\frac{\partial \theta}{\partial \bar{x}} \right)^2 + \left(\frac{\partial \theta}{\partial \bar{y}} \right)^2 \tag{6.7}$$

We calculate the global total entropy generation, $S_{T\Omega}$ over a domain Ω by integrating sum of the local entropy generations due to due to heat transfer and fluid friction.[36]

$$S_{T\Omega} = \int_{\Omega} S_f d\Omega + \int_{\Omega} S_H d\Omega \tag{6.8}$$

The relative influence of heat transfer irreversibility on the total is quantified by the dimensionless Bejan number,[55]

$$Be = \frac{\int_\Omega S_H d\Omega}{\int_\Omega S_f d\Omega + \int_\Omega S_H d\Omega} \tag{6.9}$$

If , heat transfer dominates; if $Be < 0.5$, fluid friction irreversibilities dominate.[55]

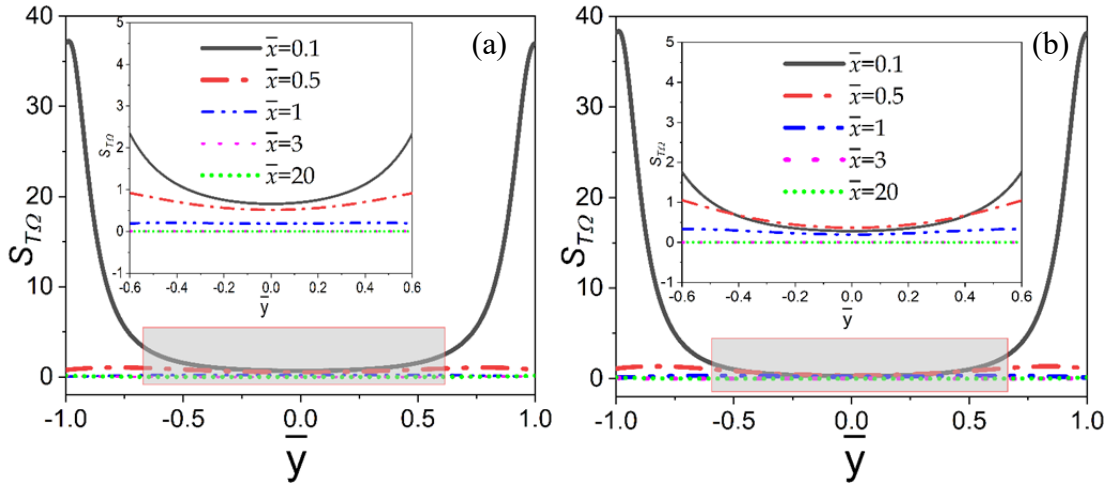

Fig.6.8. The distribution of $S_{T\Omega}$ across $\bar{y}$ at various axial locations for Pe = (a)1 and (b) Pe=3. The other parameters are: $\bar{\zeta} = 6$, $\bar{k} = 10$, $\varepsilon \overline{Wi_k}^2 = 1$, $Sp_{eff} = 1$, $Br = 1$.

Fig. 6.8 shows the distribution of $S_{T\Omega}$ across $\bar{y}$ at various axial locations for varying Peclet numbers. We see that the total entropy generation curve exhibits a symmetric distribution across every axial location. Regardless of the axial position, entropy generation peaks at the walls and gradually decreases towards the core. This can be explained by the fact that $S_{T\Omega}$ is highest near the wall due to significant changes in velocity and temperature gradients. Additionally, in the EDL region, thermal energy advection is high. As the flow moves towards the core from the wall, the decay in $S_{T\Omega}$ is progressively higher, attributed to the diminishing temperature gradient in the hydrodynamically fully developed flow. It is observed that total entropy generation is predominant in the thermally developing region but significantly reduces in the thermally developed region, indicating higher thermodynamic performance for the system.[55] The energy loss due to heat transfer irreversibility outweighs fluid frictional irreversibility, and thus, have a possible effect on the Bejan number. An increase in Pe triggers flow and temperature gradients, and hence, lead to higher fluid irreversibility in microchannels,. Overall, this parametric investigation on total entropy generation suggests that prudent

selection of thermofluidic body forces and interfacial electrokinetic parameters can minimize energy loss and maximize energy utilization in narrow confinement.

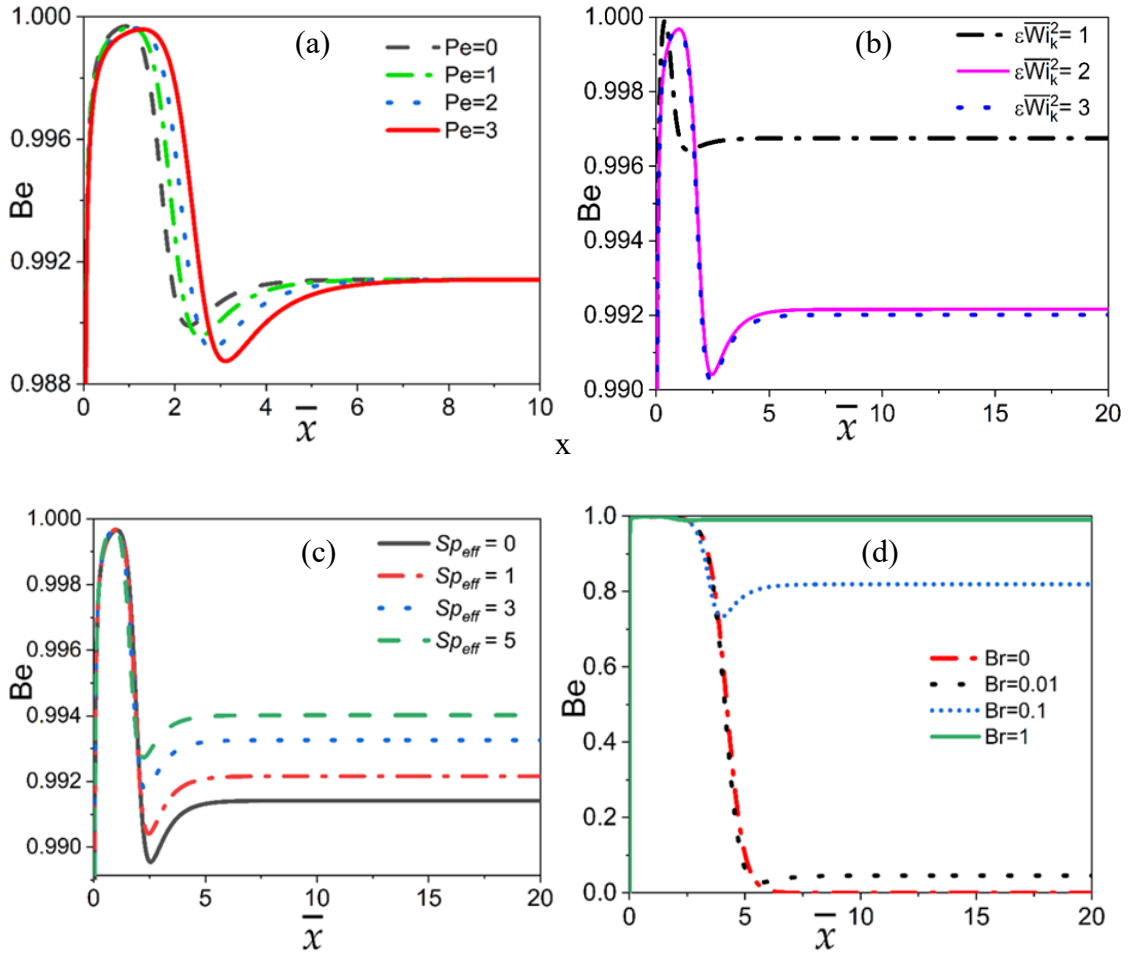

Fig. 6.9. Axial variations of the Bejan number for varying (a) Pe and at $\varepsilon\overline{Wi_k}^2 = 1, Br = 1, Sp = 1$; (b) $\varepsilon\overline{Wi_k}^2$ and at $Br = 1, Sp = 1, Pe = 1$; (c) $Sp_{eff} = 1$ and at $\varepsilon\overline{Wi_k}^2 = 1, Br = 1, Pe = 1$; (d) Br and at $\varepsilon\overline{Wi_k}^2 = 1, Pe = 1, Sp_{eff} = 1$. The other parameters are: $\bar{\zeta} = 6, \bar{k} = 10$.

Fig. 6.9 illustrates how the Bejan number changes along the narrow confinement $(\bar{x})$ across various input parameter ranges. We notice a significant decrease in the Bejan number throughout the confinement, reaching its lowest point at a specific axial location. Afterward, it gradually increases until it becomes constant beyond a certain axial position.

Interestingly, the lowest points of the *Be* curve coincide with the axial $(\bar{x})$ location marking the end of the thermal entry region. This alignment becomes evident when comparing the sudden drop in the *Be* number curve with those of singularity region in

the Nusselt number distribution. In the thermal entry region, $Be(x)$ tends to hover around unity, gradually decreasing until the system reaches its thermal entry length. Across all input parameter ranges, Figs. 6.9(a)-(c) show that heat transfer irreversibility predominantly influences the system irreversibility ($Be > 0.5$).

However, in Fig. 6.9(d), for $Br = 0.01$, convective heat transfer emerges as the primary contributor to system irreversibility at the entrance region, while friction losses take over beyond the thermal entry region. Typically, at the entrance region, $Be(x) \to 1$, due to heightened thermal irreversibilities arising from a sharp increase in the wall temperature gradient. Conversely, as we move away from the entrance region, the surface temperature gradient steadily decreases, leading to a reduction in *Be* to its minimum. Beyond this minimum point, volumetric heat generation becomes significant, elevating the temperature gradient at the wall and subsequently increasing *Be*.

6.3 Concluding remarks

Focusing solely on thermodynamic effects, this study explores the intricate interplay between electrokinetic phenomena and thermal transport in the thermally developing flow of a simplified Phan-Thien–Tanner (sPTT) viscoelastic fluid in microchannels. The thermal analysis incorporates two major internal heat sources: Joule heating—arising from the interaction between the induced streaming electric field and ionic conduction—and viscous dissipation, resulting from internal friction within the viscoelastic fluid due to shear deformation. A semi-analytical solution is derived for the dimensionless temperature distribution along the axial direction of the channel, capturing the transition from thermally developing to fully developed flow. The results show that the temperature gradient is steep near the entrance, where both Joule heating and viscous dissipation are significant. As the flow progresses, the temperature profile flattens, indicating thermal stabilization. Interestingly, in some cases, negative dimensionless temperatures appear locally due to overestimation of heat extraction near the entrance, revealing subtle energy redistribution effects. The Nusselt number, representing convective heat transfer strength, is found to be highest near the inlet and gradually declines along the channel length, eventually reaching a constant value in the thermally developed region. This trend underscores the enhanced convective transport in the thermal entrance zone due to strong temperature gradients and internal heat generation. A critical aspect of the thermodynamic analysis is the evaluation of entropy generation, which quantifies

irreversibility within the system. The study reveals that total entropy generation is most pronounced in the thermally developing region, where both temperature and electric field gradients are steep. This is particularly true under conditions of strong Joule heating and moderate to high viscoelastic response. The Bejan number (Be), a dimensionless measure comparing entropy generation due to heat transfer against total entropy generation, remains above 0.5 near the entrance, indicating that thermal irreversibility dominates over other dissipative mechanisms in this regime. These thermodynamic findings emphasize that optimal performance of electrokinetically driven microfluidic systems can be achieved by carefully tuning fluid viscoelasticity, zeta potential, and heat generation parameters to minimize entropy production while sustaining desirable thermal gradients. This has direct implications for the design of energy-efficient microscale devices such as electrokinetic heat exchangers, biosensors, and lab-on-a-chip systems.

Chapter 7. Conclusions

This thesis has progressively developed a multi-physics framework for understanding thermally developing electrokinetic transport of viscoelastic fluids in microchannels, building upon the foundations laid in earlier chapters. Chapter 3 established the electrostatic and hydrodynamic formulation for electrokinetically and pressure-driven flows, introducing the nonlinear Poisson–Boltzmann model for EDL potential distribution. Chapter 4 extended the analysis to incorporate the sPTT constitutive model, enabling prediction of viscoelastic effects on mixed electroosmotic–pressure-driven flows. Chapter 5 integrated the coupled energy equation, explicitly including Joule heating, and analysed its influence on both flow fields and EDL characteristics. Chapter 6 introduced a thermodynamic perspective via entropy generation analysis, systematically decomposing irreversibilities into viscous, thermal, and electrokinetic contributions. The present chapter synthesises these findings, distils the core insights, and outlines the broader implications of the work.

7.1 Model Validation Through Limiting Cases and Consistency

The robustness and physical reliability of the present mathematical formulation are demonstrated through its ability to recover several classical limiting behaviours reported in the literature. In the limit $\mathbf{Wi \rightarrow 0}$, the sPTT constitutive equation reduces to the Newtonian stress law, and the corresponding velocity field collapses to the classical electroosmotic–pressure-driven superposition profile, consistent with the Newtonian EOF theory (Fig. 3.4). Similarly, when thermal effects are suppressed **($\mathbf{Br \rightarrow 0}$, $\mathbf{Pe \rightarrow 0}$)**, the system becomes isothermal, and Joule heating and viscous dissipation vanish; under these conditions, the predicted potential and velocity distributions reduce to the standard isothermal Poisson–Boltzmann–EOF solutions (Fig. 4.2).

For small EDL potentials **($\Psi \ll 1$)**, the nonlinear Poisson–Boltzmann equation simplifies to the Debye–Hückel approximation, yielding the characteristic exponential decay of electrostatic potential (Fig. 2.3). Furthermore, in the absence of wall charge **($\zeta \rightarrow 0$)**, the electroosmotic contribution disappears, and the flow becomes purely pressure-driven, restoring the classical parabolic (or viscoelastic-modified) velocity profile illustrated in Fig. 3.1.

These limiting cases collectively demonstrate the internal consistency of the proposed formulation and confirm that it correctly reduces to established Newtonian, isothermal, and weak-field benchmarks, thereby reinforcing the soundness and applicability of the developed framework.

7.2 Comparison with Established Literature

A comparison of the present results with established literature reveals strong agreement in classical limits, while clear deviations emerge when nonlinear electrostatics, viscoelasticity (sPTT), and thermally developing conditions become dominant.

Electroosmotic and Pressure Driven Flow (Chapter 3)

In the low Wi and thin EDL regime, the predicted EOF velocity profiles (Fig. 3.2) closely match the Newtonian/PTT results of Afonso et al. [53], [54] and classical electroosmotic theory [68], confirming the correctness of the formulation. At moderate–high elasticity ($Wi \gtrsim O(1)$), deviations appear specifically, core flattening, wall localized shear thinning, and enhanced normal stresses as seen in Figs. 3.3–3.7. These nonlinear viscoelastic trends are consistent with observations reported by Sarkar and coworkers [36], [55]but are absent in Newtonian EOF theory.

Streaming Potential Mediated Flow (Chapter 4)

For weak zeta potentials and negligible elasticity, the streaming potential matches well with the Newtonian benchmark of Dey et al. [137](Fig. 4.2), validating the electrostatic formulation.

Incorporating viscoelasticity yields higher induced electric fields and reduced volumetric flow rate (Figs. 4.3–4.6). These deviations arise from polymeric normal stresses interacting with EDL charge convection—effects not captured in Newtonian or Oldroyd B based streaming potential models. Similar qualitative trends have been noted in polymeric electrolyte experiments [87], [109]and viscoelastic electrokinetics [48].

Thermally Developing EO–PD Flow (Chapter 5)

In the Newtonian limit, temperature profiles and Nusselt number variations (Fig. 5.2) compare excellently with the benchmark results of Dey et al. [33], validating the thermal model. With viscoelastic (sPTT) behaviour, two consistent deviations appear (Figs. 5.3–5.11):

- Delayed thermal boundary layer development due to shear thinning induced viscosity reduction near the wall.
- Stronger Joule heating nonlinearity, amplified by elastic stress contributions to viscous dissipation.

These effects agree with earlier electrothermal viscoelastic studies [38], [55], but previous works did not address thermally developing regimes, which the present model extends.

Thermally Developing Streaming Potential Flow (Chapter 6)

Baseline Newtonian behaviour (Fig. 6.2) closely matches Dey et al. [137], confirming accurate electro thermal coupling. With viscoelasticity, notable deviations emerge (Figs. 6.3–6.9):

- Stronger back electroosmotic flow induced by higher streaming potential, reducing local Nusselt number more than Newtonian predictions.
- Shift in entropy generation from heat transfer dominated (Newtonian) to viscous dissipation dominated (viscoelastic), consistent with trends reported by Goswami et al. [59].

Summary

Agreement in the Newtonian and low-elasticity limits confirms the accuracy of the model. The observed deviations are altered normal stresses, nonlinear streaming-potential effects, modified thermal boundary-layer growth, and shifted entropy generation which are arise from nonlinear viscoelasticity (sPTT), full Poisson–Boltzmann electrostatics, and thermally developing conditions. These features extend beyond earlier studies that typically assume Newtonian fluids or simplified EDL and thermal models.

7.3 Engineering Implications

The present results offer useful guidance for improving the design and performance of microfluidic devices such as microchannel heat exchangers, biochips, and lab-on-chip platforms. The modified velocity profiles observed under viscoelastic electroosmotic and pressure-driven conditions (Figs. 3.2–3.6) shows that regulating fluid elasticity or surface charge can promote smoother flow and lessen pressure loads in microdevices.

For energy-based applications, the variation in streaming potential (Figs. 4.2–4.5) shows that tuning viscoelastic electrolyte properties can modulate the induced electric fields, thereby improving the performance of electrokinetic pumps and self-powered biochip sensors.

Thermal analysis results (Figs. 5.2–5.7) show that viscoelasticity delays thermal boundary layer growth while amplifying Joule heating. These trends highlight the need to account for non-Newtonian rheology when designing micro heat exchangers, especially in systems handling polymeric or biological samples. Proper control of electric-field strength and wall properties can enhance heat removal and minimize hotspots.

Finally, the entropy-generation trends in streaming-potential-mediated thermal transport (Figs. 6.4–6.8) demonstrate that viscoelastic fluids shift irreversibility from heat-transfer-dominated to viscous-dissipation-dominated mechanisms. This insight can help engineers optimize device geometry, flow rates, and electric-field inputs to reduce energy losses and improve overall microdevice efficiency.

7.4 Key Conclusions

The major conclusions derived from this research are summarised below:

Nonlinear electrostatic modelling using the full Poisson–Boltzmann equation accurately predicts electroosmotic transport under high ζ-potential conditions, providing improved reliability over Debye–Hückel approximations and forming a robust basis for microfluidic device design.

Electrokinetic parameters—particularly zeta potential and Debye length—strongly govern electrohydrodynamics; increasing ζ or increasing EDL thickness intensifies electroosmotic body force, velocity gradients, and shear stress, while simultaneously enhancing Joule heating and modifying thermal development.

Viscoelastic effects, represented using the sPTT constitutive model, significantly influence flow structure. Moderate elasticity flattens the velocity profile and enhances heat transport, whereas excessive elasticity thickens the thermal boundary layer and reduces Nusselt number and flow rate.

Thermally developing operating conditions modify electrokinetic characteristics, as Joule heating and viscous dissipation reduce viscosity and reshape EDL potential

distribution, influencing streaming potential, flow resistance, and heat transfer behaviour.

Entropy generation analysis identifies distinct spatial irreversibility trends: heat transfer irreversibility dominates near the channel entrance, whereas fluid-friction irreversibility dominates downstream. Optimized selection of $\tilde{\zeta}$, Pe, Br, and viscoelastic parameters minimizes total entropy generation.

Coupled electrokinetic–viscoelastic interaction effects produce nonlinear transport behaviour, including a peak in streaming potential and polymeric stress near $\zeta \approx 6$, beyond which they decline due to reduced relaxation time and strain rate.

Bejan number behaviour demonstrates competing influences, where increasing viscoelasticity suppresses thermal irreversibility and increasing ζ amplifies it, offering clear strategies for performance-optimized microchannel and micro-thermal device development.

7.5 Limitations of the Present Mathematical Model

The present formulation, while comprehensive in capturing the essential electro-thermo-rheological coupling in viscoelastic microchannel flows, is subject to several simplifying assumptions that should be acknowledged. The analysis is limited to a two-dimensional, fully developed flow framework, neglecting three-dimensional effects such as secondary motions, and corner vortices that may occur in practical microchannels.

Fluid properties such as viscosity, thermal conductivity, permittivity, and electrical conductivity are treated as constant, aside from their implicit dependence through the sPTT stress–strain relation, thereby neglecting temperature or concentration induced variations that may become important under strong Joule heating or steep thermal gradients. The flow is assumed strictly laminar, but potential elastic instabilities at high Weissenberg numbers are not captured in the present steady, one dimensional formulation. The Poisson–Boltzmann model assumes a dilute symmetric electrolyte and neglects finite-ion size, surface-charge regulation, and steric effects, which can significantly alter the EDL at high zeta potentials or in concentrated solutions.

Further the model applies no-slip boundaries, overlooking wall slip that may affect electroosmotic mobility and thermal boundary-layer behaviour. Therefore, these

approximations facilitate semi-analytical progress but may limit predictive accuracy under strong electric fields, intense Joule heating, or highly elastic flow regimes.

7.6 Scope of future work

Future extensions of the present research will focus on the following directions:

The model will be extended to three-dimensional geometries and transient flow conditions, incorporating patterned surfaces and complex channel shapes to more accurately represent realistic microfluidic configurations.

- The framework will incorporate temperature and concentration-dependent viscoelastic rheology, together with non-ideal electrochemical effects such as finite ion size and surface charge regulation, to enhance predictive capability for biological and polymeric fluids.
- Experimental validation will be undertaken using polymeric electrolytes, employing techniques such as micro-PIV, μ-LIF, and micro-thermography to benchmark theoretical and numerical predictions under practical operating conditions.
- Coupled multi-field interactions will be explored, integrating external magnetic, acoustic, or electrothermal fields to enable active control of electrokinetic and viscoelastic transport phenomena.
- High-fidelity numerical simulations will be implemented using CFD tools such as COMSOL Multiphysics, ANSYS Fluent, or OpenFOAM to provide hybrid validation and deeper insight alongside the semi-analytical modelling framework developed in this work.
- Optimization studies will be performed using entropy minimization and multi-objective performance metrics to improve thermal–hydrodynamic efficiency and minimize irreversibility in microdevice operation.

The developed framework will be applied to device-level systems, such as electrokinetically actuated micromixers, viscoelastic microreactors, and microscale heat exchangers, to enable advanced microfluidic design and implementation.

References

[1] S. N. Bhatia and D. E. Ingber, “Microfluidic organs-on-chips,” *Nat. Biotechnol.*, vol. 32, no. 8, pp. 760–772, 2014, S. N. Bhatia and D. E. Ingber, “Microfluidic organs-on-chips,” *Nat. Biotechnol.*, vol. 32, no. 8, pp. 760–772, 2014.

[2] P. Tabeling, *Introduction to microfluidics*. Oxford university press, 2023, doi: doi.org/10.1093/oso/9780192845306.001.0001.

[3] E. W. K. Young and D. J. Beebe, “Fundamentals of microfluidic cell culture in controlled microenvironments,” *Chem. Soc. Rev.*, vol. 39, no. 3, pp. 1036–1048, 2010, doi: doi.org/10.1039/b909900j.

[4] N. P. Thien and R. I. Tanner, “A new constitutive equation derived from network theory,” *J. Nonnewton. Fluid Mech.*, vol. 2, no. 4, pp. 353–365, 1977, doi: doi.org/10.1016/0377-0257(77)80021-9.

[5] A. K. Yetisen, M. S. Akram, and C. R. Lowe, “Paper-based microfluidic point-of-care diagnostic devices,” *Lab Chip*, vol. 13, no. 12, pp. 2210–2251, 2013, doi: doi.org/10.1039/C3LC50169H.

[6] N. Azizipour, R. Avazpour, D. Rosenzweig, M. Sawan, and A. Ajji, “Evolution of Biochip Technology: A Review from Lab-on-a-Chip to Organ-on-a-Chip,” *Micromachines*, vol. 11, p. 599, Jun. 2020, doi: 10.3390/mi11060599.

[7] N.-T. Nguyen, S. T. Wereley, and S. A. M. Shaegh, *Fundamentals and applications of microfluidics*. Artech house, 2019.

[8] A. Makhinia, P. Azizian, V. Beni, J. Casals-Terré, J. Cabot, and P. Ersman, “On-Demand Inkjet Printed Hydrophilic Coatings for Flow Control in 3D-Printed Microfluidic Devices Embedded with Organic Electrochemical Transistors,” *Adv. Mater. Technol.*, vol. 8, Jul. 2023, doi: 10.1002/admt.202300127.

[9] M. von Smoluchowski, “Contribution to the theory of electro-osmosis and related phenomena,” *Bull. Int. Acad. Sci. Cracovie*, vol. 3, no. 3, pp. 184–199, 1903.

[10] R. J. Hunter, *Zeta potential in colloid science: principles and applications*, vol. 2. Academic press, 2013.

[11] H. A. Stone, A. D. Stroock, and A. Ajdari, “Engineering flows in small devices: microfluidics toward a lab-on-a-chip,” *Annu. Rev. Fluid Mech.*, vol. 36, no. 1, pp. 381–411, 2004, https://doi.org/10.1146/annurev.fluid.36.050802.122124.

[12] S. Kandlikar, *Heat transfer and fluid flow in minichannels and microchannels*. elsevier, 2006.

[13] C. Ren, W. Li, J. Ma, G. Huang, and C. Li, “Flow boiling in microchannels enhanced by parallel microgrooves fabricated on the bottom surfaces,” *Int. J. Heat Mass Transf.*, vol. 166, p. 120756, 2021, doi: doi.org/10.1016/j.ijheatmasstransfer.2020.120756.

[14] C.-H. Chen, “Thermal Transport Characteristics of Mixed Pressure and Electro-Osmotically Driven Flow in Micro- and Nanochannels With Joule Heating,” *J. Heat Transfer*, vol. 131, no. 2, Dec. 2008, doi: 10.1115/1.2994720.

[15] P. Kaushik, P. K. Mondal, S. Pati, and S. Chakraborty, “Heat Transfer and Entropy Generation Characteristics of a Non-Newtonian Fluid Squeezed and Extruded Between Two Parallel Plates,” *J. Heat Transfer*, vol. 139, no. 2, Nov. 2016, doi: 10.1115/1.4034898.

[16] D. B. Tuckerman and R. F. W. Pease, “High-performance heat sinking for VLSI,” *IEEE Electron device Lett.*, vol. 2, no. 5, pp. 126–129, 2005 https://doi.org/10.1109/EDL.1981.25367.

[17] J. Bowers *et al.*, “Flow and heat transfer behaviour of nanofluids in microchannels,” *Prog. Nat. Sci. Mater. Int.*, vol. 28, no. 2, pp. 225–234, 2018, doi: doi.org/10.1016/j.pnsc.2018.03.005.

[18] H. Bruus, *Theoretical microfluidics*, vol. 18. Oxford university press, 2007.

[19] R. F. Probstein, *Physicochemical hydrodynamics: an introduction*. John Wiley & Sons, 2005.

[20] “R. Byron Bird, Warren E. Stewart, Edwin N. Lightfoot - Transport phenomena-J. Wiley (2002).pdf.”

[21] B. J. Kirby and E. F. Hasselbrink Jr, “Zeta potential of microfluidic substrates: 1. Theory, experimental techniques, and effects on separations,” *Electrophoresis*, vol. 25, no. 2, pp. 187–202, 2004.

[22] X. Bian, F. Li, and Y. Jian, “The streaming potential of fluid through a microchannel with modulated charged surfaces,” *Micromachines*, vol. 13, no. 1, p. 66, 2021 https://doi.org/10.3390/mi13010066.

[23] P. Goswami and S. Chakraborty, “Energy Transfer through Streaming Effects in Time-Periodic Pressure-Driven Nanochannel Flows with Interfacial Slip,” *Langmuir*, vol. 26, no. 1, pp. 581–590, Jan. 2010, doi: 10.1021/la901209a.

[24] S. Chakraborty and S. Das, “Streaming-field-induced convective transport and its influence on the electroviscous effects in narrow fluidic confinement beyond the Debye-H\"uckel limit,” *Phys. Rev. E*, vol. 77, no. 3, p. 37303, Mar. 2008, doi: 10.1103/PhysRevE.77.037303.

[25] A. Sadeghi, M. H. Saidi, H. Veisi, and M. Fattahi, “Thermally developing electroosmotic flow of power-law fluids in a parallel plate microchannel,” *Int. J. Therm. Sci.*, vol. 61, pp. 106–117, 2012 http://dx.doi.org/10.1016/j.ijthermalsci.2012.06.006.

[26] J. N. Israelachvili, *Intermolecular and surface forces*. Academic press, 2011.

[27] B. J. Kirby, *Micro-and nanoscale fluid mechanics: transport in microfluidic devices*. Cambridge university press, 2010 .

[28] R. F. Probstein, *Solutions of electrolytes*. 1994.

[29] D. Banerjee, S. K. Mehta, S. Pati, and P. Biswas, “Analytical solution to heat transfer for mixed electroosmotic and pressure-driven flow through a microchannel with slip-dependent zeta potential,” *Int. J. Heat Mass Transf.*, vol. 181, p. 121989, 2021, doi: 10.1016/j.ijheatmasstransfer.2021.121989.

[30] C. Zhao and C. Yang, “Advances in electrokinetics and their applications in

micro/nano fluidics," *Microfluid. Nanofluidics*, vol. 13, no. 2, pp. 179–203, 2012, doi: 10.1007/s10404-012-0971-1.

[31] B. Mahapatra and A. Bandopadhyay, "Numerical analysis of combined electroosmotic-pressure driven flow of a viscoelastic fluid over high zeta potential modulated surfaces," *Phys. Fluids*, vol. 33, no. 1, p. 12001, Jan. 2021, doi: 10.1063/5.0033088.

[32] C. Zhao and C. Yang, "Electrokinetics of non-Newtonian fluids: A review," *Adv. Colloid Interface Sci.*, vol. 201–202, pp. 94–108, 2013, doi: https://doi.org/10.1016/j.cis.2013.09.001.

[33] R. Dey, D. Chakraborty, and S. Chakraborty, "Extended Graetz problem for combined electroosmotic and pressure-driven flows in narrow confinements with thick electric double layers," *Int. J. Heat Mass Transf.*, vol. 55, no. 17, pp. 4724–4733, 2012, doi: https://doi.org/10.1016/j.ijheatmasstransfer.2012.04.034.

[34] D. Maynes and B. W. Webb, "Fully developed electro-osmotic heat transfer in microchannels," *Int. J. Heat Mass Transf.*, vol. 46, no. 8, pp. 1359–1369, 2003, doi: https://doi.org/10.1016/S0017-9310(02)00423-4.

[35] K. Horiuchi, P. Dutta, and A. Hossain, "Joule-heating effects in mixed electroosmotic and pressure-driven microflows under constant wall heat flux," *J. Eng. Math.*, vol. 54, no. 2, pp. 159–180, 2006, doi: 10.1007/s10665-005-9019-9.

[36] S. Sarkar, S. Ganguly, and P. Dutta, "Thermofluidic characteristics of combined electroosmotic and pressure driven flows in narrow confinements in presence of spatially non-uniform magnetic field," *Int. J. Heat Mass Transf.*, vol. 104, pp. 1325–1340, 2017, doi: 10.1016/j.ijheatmasstransfer.2016.09.072.

[37] S. Arulanandam and D. Li, "Liquid transport in rectangular microchannels by electroosmotic pumping," *Colloids Surfaces A Physicochem. Eng. Asp.*, vol. 161, no. 1, pp. 89–102, 2000, doi: https://doi.org/10.1016/S0927-7757(99)00328-3.

[38] A. Sadeghi and M. H. Saidi, "Viscous dissipation effects on thermal transport characteristics of combined pressure and electroosmotically driven flow in microchannels," *Int. J. Heat Mass Transf.*, vol. 53, no. 19, pp. 3782–3791, 2010, doi: https://doi.org/10.1016/j.ijheatmasstransfer.2010.04.028.

[39] S. Das and S. Chakraborty, "Analytical solutions for velocity, temperature and concentration distribution in electroosmotic microchannel flows of a non-Newtonian bio-fluid," *Anal. Chim. Acta*, vol. 559, no. 1, pp. 15–24, 2006, doi: https://doi.org/10.1016/j.aca.2005.11.046.

[40] C. O. Ng, "Combined pressure-driven and electroosmotic flow of Casson fluid through a slit microchannel," *J. Nonnewton. Fluid Mech.*, vol. 198, pp. 1–9, 2013, doi: 10.1016/j.jnnfm.2013.03.003.

[41] H. Yavari, A. Sadeghi, M. H. Saidi, and S. Chakraborty, "Combined influences of viscous dissipation, non-uniform Joule heating and variable thermophysical properties on convective heat transfer in microtubes," *Int. J. Heat Mass Transf.*, vol. 55, no. 4, pp. 762–772, 2012, doi: 10.1016/j.ijheatmasstransfer.2011.10.033.

[42] S. Sarkar, S. Ganguly, and P. Dutta, "Thermally developing combined magnetohydrodynamic and electrokinetic transport in narrow confinements with

interfacial slip," *Int. J. Heat Mass Transf.*, vol. 100, pp. 451–463, 2016, doi: https://doi.org/10.1016/j.ijheatmasstransfer.2016.04.101.

[43] C.-O. Ng and C. Qi, "Electroosmotic flow of a viscoplastic material through a slit channel with walls of arbitrary zeta potential," *Phys. Fluids*, vol. 25, no. 10, 2013 https://doi.org/10.1063/1.4825368.

[44] J. G. Oldroyd, "On the formulation of rheological equations of state," *Proc. R. Soc. London. Ser. A. Math. Phys. Sci.*, vol. 200, no. 1063, pp. 523–541, 1950 https://doi.org/10.1098/rspa.1950.0035 .

[45] M. A. Alves, P. J. Oliveira, and F. T. Pinho, "Numerical methods for viscoelastic fluid flows," *Annu. Rev. Fluid Mech.*, vol. 53, no. 1, pp. 509–541, 2021 https://doi.org/10.1146/annurev-fluid-010719-060107.

[46] R. G. Larson, "Constitutive equations for thixotropic fluids," *J. Rheol. (N. Y. N. Y).*, vol. 59, no. 3, pp. 595–611, 2015 https://doi.org/10.1122/1.4913584.

[47] J. Hartmann, D. Hermelin, and J. H. Levy, "Viscoelastic testing: an illustrated review of technology and clinical applications," *Res. Pract. Thromb. Haemost.*, vol. 7, no. 1, p. 100031, 2023, doi: https://doi.org/10.1016/j.rpth.2022.100031.

[48] S. Sarkar, "Streaming-potential-mediated pressure-driven transport of Phan-Thien--Tanner fluids in a microchannel," *Phys. Rev. E*, vol. 101, no. 5, p. 53104, May 2020, doi: 10.1103/PhysRevE.101.053104.

[49] H. Giesekus, "A simple constitutive equation for polymer fluids based on the concept of deformation-dependent tensorial mobility," *J. Nonnewton. Fluid Mech.*, vol. 11, no. 1, pp. 69–109, 1982, doi: https://doi.org/10.1016/0377-0257(82)85016-7.

[50] M. A. Alves, P. J. Oliveira, and F. T. Pinho, "On the effect of contraction ratio in viscoelastic flow through abrupt contractions," *J. Nonnewton. Fluid Mech.*, vol. 122, no. 1, pp. 117–130, 2004, doi: https://doi.org/10.1016/j.jnnfm.2004.01.022.

[51] H. Zeng, B. Zhao, J. N. Israelachvili, and M. Tirrell, "Liquid- to Solid-Like Failure Mechanism of Thin Polymer Films at Micro- and Nanoscales," *Macromolecules*, vol. 43, no. 1, pp. 538–542, Jan. 2010, doi: 10.1021/ma901845z.

[52] Q. Zhao *et al.*, "Large-scale ordering of nanoparticles using viscoelastic shear processing," *Nat. Commun.*, vol. 7, no. 1, p. 11661, 2016 NATURE COMMUNICATIONS | 7:11661 | DOI: 10.1038/ncomms11661 | www.nature.com/naturecommunications.

[53] A. M. Afonso, M. A. Alves, and F. T. Pinho, "Analytical solution of mixed electro-osmotic/pressure driven flows of viscoelastic fluids in microchannels," *J. Nonnewton. Fluid Mech.*, vol. 159, no. 1, pp. 50–63, 2009, doi: https://doi.org/10.1016/j.jnnfm.2009.01.006.

[54] L. L. Ferrás, A. M. Afonso, M. A. Alves, J. M. Nóbrega, and F. T. Pinho, "Electro-osmotic and pressure-driven flow of viscoelastic fluids in microchannels: Analytical and semi-analytical solutions," *Phys. Fluids*, vol. 28, no. 9, p. 93102, Sep. 2016, doi: 10.1063/1.4962357.

[55] S. Sarkar, S. Ganguly, and P. Dutta, "Thermally developing combined

magnetohydrodynamic and electrokinetic transport in narrow confinements with interfacial slip," *Int. J. Heat Mass Transf.*, vol. 100, pp. 451–463, 2016, doi: 10.1016/j.ijheatmasstransfer.2016.04.101.

[56] G. M. Mala, D. Li, and J. D. Dale, "Heat Transfer and Fluid Flow in Microchannels," *ASME Int. Mech. Eng. Congr. Expo. Proc.*, vol. 1996-U, no. 13, pp. 127–136, 1996, doi: 10.1115/IMECE1996-1345.

[57] A. Elazhary and H. M. Soliman, "Analytical solutions of fluid flow and heat transfer in parallel-plate micro-channels at high zeta-potentials," *Int. J. Heat Mass Transf.*, vol. 52, no. 19–20, pp. 4449–4458, 2009, doi: 10.1016/j.ijheatmasstransfer.2009.03.036.

[58] M. S. N. Oliveira, M. A. Alves, and F. T. Pinho, "Microfluidic flows of viscoelastic fluids," *Transp. Mix. Laminar Flows From Microfluid. to Ocean. Curr.*, pp. 131–174, 2011 https://doi.org/10.1002/9783527639748.ch6.

[59] P. Goswami, P. K. Mondal, A. Datta, and S. Chakraborty, "Entropy generation minimization in an electroosmotic flow of non-Newtonian fluid: effect of conjugate heat transfer," J. Heat Transfer, vol. 138, no. 5, 2016 https://doi.org/10.1115/1.4032431 .

[60] P. Goswami and S. Chakraborty, "Heat transfer characteristics of an electroosmotic flow of viscoelastic fluid in slit microchannel," in *Proceedings of CHT-17 ICHMT International Symposium on Advances in Computational Heat Transfer*, Begel House Inc., 2017 DOI:10.1615/ICHMT.2017.CHT-7 .

[61] S. Sarkar and S. Ganguly, "Fully developed thermal transport in combined pressure and electroosmotically driven flow of nanofluid in a microchannel under the effect of a magnetic field," *Microfluid. Nanofluidics*, vol. 18, no. 4, pp. 623–636, 2015, doi: 10.1007/s10404-014-1461-4.

[62] E. A. Ramos, C. Treviño, F. Méndez, and J. J. Lizardi, "Electroosmotic flow in a thin microchannel under the influence of some thermal electrokinetic effects," *J. Brazilian Soc. Mech. Sci. Eng.*, vol. 44, no. 3, p. 75, 2022 https://doi.org/10.1007/s40430-022-03385-2.

[63] D. Li, *Electrokinetics in microfluidics*, vol. 2. Elsevier, 2004.

[64] J. H. Masliyah and S. Bhattacharjee, *Electrokinetic and colloid transport phenomena*. John Wiley & Sons, 2006.

[65] G. M. Whitesides, "The origins and the future of microfluidics," *Nature*, vol. 442, no. 7101, pp. 368–373, 2006 doi:10.1038/nature05058 .

[66] G. Karniadakis, A. Beskok, and N. Aluru, *Microflows and nanoflows: fundamentals and simulation*. Springer, 2005.

[67] P. J. OLIVEIRA and F. T. PINHO, "Analytical solution for fully developed channel and pipe flow of Phan-Thien–Tanner fluids," *J. Fluid Mech.*, vol. 387, pp. 271–280, 1999, doi: 10.1017/S002211209900453X.

[68] M. Z. Bazant, B. D. Storey, and A. A. Kornyshev, "Double layer in ionic liquids: Overscreening versus crowding," *Phys. Rev. Lett.*, vol. 106, no. 4, p. 46102, 2011. https://doi.org/10.1103/PhysRevLett.106.046102

[69] F. F. Reuss, “Sur un nouvel effet de l’électricité galvanique,” *Mem. Soc. Imp. Natur. Moscou*, vol. 2, pp. 327–337, 1809.

[70] H. von Helmholtz, “Studien über electrische Grenzschichten,” *Ann. Phys.*, vol. 243, no. 7, pp. 337–382, 1879.

[71] E. J. W. Verwey and J. T. G. Overbeek, “Theory of the stability of lyophobic colloids,” *J. Colloid Sci.*, vol. 10, no. 2, pp. 224–225, 1955.

[72] S. Levine, J. R. Marriott, G. Neale, and N. Epstein, “Theory of electrokinetic flow in fine cylindrical capillaries at high zeta-potentials,” *J. Colloid Interface Sci.*, vol. 52, no. 1, pp. 136–149, 1975, doi: doi.org/10.1016/0021-9797(75)90310-0 .

[73] M. Z. Bazant and T. M. Squires, “Induced-charge electrokinetic phenomena: theory and microfluidic applications,” *Phys. Rev. Lett.*, vol. 92, no. 6, p. 66101, 2004, doi: doi.org/10.1103/PhysRevLett.92.066101.

[74] V. G. Levich, *Physicochemical Hydrodynamics*. in Prentice-Hall international series in the physical and chemical engineering sciences. Prentice-Hall, 1962..

[75] R. B. Schoch, J. Han, and P. Renaud, “Transport phenomena in nanofluidics,” *Rev. Mod. Phys.*, vol. 80, no. 3, pp. 839–883, 2008, doi: doi.org/10.1103/RevModPhys.80.839.

[76] P. Dutta and A. Beskok, “Analytical Solution of Combined Electroosmotic/Pressure Driven Flows in Two-Dimensional Straight Channels: Finite Debye Layer Effects,” *Anal. Chem.*, vol. 73, no. 9, pp. 1979–1986, May 2001, doi: 10.1021/ac001182i.

[77] G. H. Tang, X. F. Li, Y. L. He, and W. Q. Tao, “Electroosmotic flow of non-Newtonian fluid in microchannels,” *J. Nonnewton. Fluid Mech.*, vol. 157, no. 1–2, pp. 133–137, 2009, https://doi.org/10.1016/j.jnnfm.2008.11.002 .

[78] J. Chakraborty, S. Ray, and S. Chakraborty, “Role of streaming potential on pulsating mass flow rate control in combined electroosmotic and pressure-driven microfluidic devices,” *Electrophoresis*, vol. 33, no. 3, pp. 419–425, Feb. 2012, doi: https://doi.org/10.1002/elps.201100414.

[79] S. Bhattacharjee, S. Mondal, M. Mondal, and S. De, “Effect of electrolyte nature in mass transport of a neutral solute in a microtube with porous wall,” *AIChE J.*, vol. 66, no. 1, p. e16765, 2020, https://doi.org/10.1002/aic.16765 .

[80] B. Mahapatra and A. Bandopadhyay, “Efficacy of microconfined fluid mixing in a combined electroosmotic and pressure driven transport of complex fluid over discrete electrodes,” *Phys. Fluids*, vol. 34, no. 4, 2022, doi: doi.org/10.1063/5.0086541 .

[81] A. Bandopadhyay and S. Chakraborty, “Steric-effect induced alterations in streaming potential and energy transfer efficiency of non-newtonian fluids in narrow confinements.,” *Langmuir*, vol. 27, no. 19, pp. 12243–12252, Oct. 2011, doi: 10.1021/la202273e.

[82] S. Chakraborty, “Electrokinetics with blood,” *Electrophoresis*, vol. 40, no. 1, pp. 180–189, Jan. 2019, doi: doi.org/10.1002/elps.201800353.

[83] M. Azari, A. Sadeghi, and S. Chakraborty, “Electroosmotic flow and heat transfer in a heterogeneous circular microchannel,” *Appl. Math. Model.*, vol. 87, pp. 640–654, 2020, doi: 10.1016/j.apm.2020.06.022.

[84] W. B. J. Zimmerman, *Microfluidics: history, theory and applications*, vol. 466. Springer Science & Business Media, 2006.

[85] C. Zhao, E. Zholkovskij, J. H. Masliyah, and C. Yang, “Analysis of electroosmotic flow of power-law fluids in a slit microchannel,” *J. Colloid Interface Sci.*, vol. 326, no. 2, pp. 503–510, 2008, doi: doi.org/10.1016/j.jcis.2008.06.028.

[86] J. Ji, “Numerical Simulation of Electroosmotic Flow of Viscoelastic Fluid in Microchannel,” 2022, *Old Dominion University*.

[87] C. L. A. Berli, “Output pressure and efficiency of electrokinetic pumping of non-Newtonian fluids,” *Microfluid. Nanofluidics*, vol. 8, no. 2, pp. 197–207, 2010, doi: 10.1007/s10404-009-0455-0 .

[88] C. L. A. Berli and M. L. Olivares, “Electrokinetic flow of non-Newtonian fluids in microchannels,” *J. Colloid Interface Sci.*, vol. 320, no. 2, pp. 582–589, 2008, doi: doi.org/10.1016/j.jcis.2007.12.032.

[89] M. A. Vakili, A. Sadeghi, M. H. Saidi, and A. A. Mozafari, “Electrokinetically driven fluidic transport of power-law fluids in rectangular microchannels,” *Colloids Surfaces A Physicochem. Eng. Asp.*, vol. 414, pp. 440–456, 2012, doi: 10.1007/s10404-009-0455-0.

[90] S. Chakraborty, “Electroosmotically driven capillary transport of typical non-Newtonian biofluids in rectangular microchannels,” *Anal. Chim. Acta*, vol. 605, no. 2, pp. 175–184, 2007, doi: doi.org/10.1016/j.aca.2007.10.049 .

[91] S. Y. Deng, Y. J. Jian, Y. H. Bi, L. Chang, H. J. Wang, and Q. S. Liu, “Unsteady electroosmotic flow of power-law fluid in a rectangular microchannel,” *Mech. Res. Commun.*, vol. 39, no. 1, pp. 9–14, 2012, doi: doi.org/10.1016/j.mechrescom.2011.09.003 .

[92] N. Vasu and S. De, “Electroosmotic flow of power-law fluids at high zeta potentials,” *Colloids Surfaces A Physicochem. Eng. Asp.*, vol. 368, no. 1, pp. 44–52, 2010, doi: doi.org/10.1016/j.colsurfa.2010.07.014.

[93] R. P. Bharti, D. J. E. Harvie, and M. R. Davidson, “Electroviscous effects in steady fully developed flow of a power-law liquid through a cylindrical microchannel,” *Int. J. Heat Fluid Flow*, vol. 30, no. 4, pp. 804–811, 2009, doi: doi.org/10.1016/j.ijheatfluidflow.2009.01.012 .

[94] C. Zhao and C. Yang, “Analysis of power-law fluid flow in a microchannel with electrokinetic effects,” *Int. J. Emerg. Multidiscip. Fluid Sci.*, vol. 1, pp. 37–52, 2009, doi: dx.doi.org/10.1260/1756-8315.1.1.37.

[95] Q. Liu, Y. Jian, and L. Yang, “Alternating current electroosmotic flow of the Jeffreys fluids through a slit microchannel,” *Phys. fluids*, vol. 23, no. 10, 2011, doi: doi.org/10.1063/1.3640082.

[96] J. Escandón, E. Jiménez, C. Hernández, O. Bautista, and F. Méndez, “Transient electroosmotic flow of Maxwell fluids in a slit microchannel with asymmetric zeta

potentials," *Eur. J. Mech.*, vol. 53, pp. 180–189, 2015, doi: doi.org/10.1016/j.euromechflu.2015.05.001 .

[97] R. Sarma, N. Deka, K. Sarma, and P. K. Mondal, "Electroosmotic flow of Phan-Thien–Tanner fluids at high zeta potentials: An exact analytical solution," *Phys. Fluids*, vol. 30, no. 6, p. 62001, Jun. 2018, doi: 10.1063/1.5033974.

[98] D. Burgreen and F. R. Nakache, "Electrokinetic Flow in Ultrafine Capillary Slits1," *J. Phys. Chem.*, vol. 68, no. 5, pp. 1084–1091, May 1964, doi: 10.1021/j100787a019.

[99] Y. Huang, J. Chen, T. Wong, and J.-L. Liow, "Experimental and theoretical investigations of non-Newtonian electro-osmotic driven flow in rectangular microchannels," *Soft Matter*, vol. 12, no. 29, pp. 6206–6213, 2016, doi: doi.org/10.1039/c6sm00408c.

[100] D. Kumar and B. Barman, "Combined electroosmotic and pressure driven flow through soft nanochannel grafted with partially ion-penetrable polyelectrolyte layers," *Mol. Simul.*, vol. 50, no. 17–18, pp. 1502–1514, 2024, doi: doi.org/10.1080/08927022.2024.2388788.

[101] D. Yao, "A non-Newtonian fluid model with an objective vorticity," *J. Nonnewton. Fluid Mech.*, vol. 218, pp. 99–105, 2015, doi: 10.1016/j.jnnfm.2015.02.002.

[102] S. Dhinakaran, A. M. Afonso, M. A. Alves, and F. T. Pinho, "Steady viscoelastic fluid flow between parallel plates under electro-osmotic forces: Phan-Thien–Tanner model," *J. Colloid Interface Sci.*, vol. 344, no. 2, pp. 513–520, 2010, doi: doi.org/10.1016/j.jcis.2010.01.025.

[103] A. Babaie, A. Sadeghi, and M. H. Saidi, "Combined electroosmotically and pressure driven flow of power-law fluids in a slit microchannel," *J. Nonnewton. Fluid Mech.*, vol. 166, no. 14, pp. 792–798, 2011, doi: doi.org/10.1016/j.jnnfm.2011.04.012.

[104] M. Mondal, R. P. Misra, and S. De, "Combined electroosmotic and pressure driven flow in a microchannel at high zeta potential and overlapping electrical double layer," *Int. J. Therm. Sci.*, vol. 86, pp. 48–59, 2014, doi:10.1016/j.ijthermalsci.2014.06.029.

[105] A. Mansouri, C. Scheuerman, S. Bhattacharjee, D. Y. Kwok, and L. W. Kostiuk, "Transient streaming potential in a finite length microchannel," *J. Colloid Interface Sci.*, vol. 292, no. 2, pp. 567–580, 2005, doi: 10.1016/j.jcis.2005.05.094.

[106] A. Bandopadhyay, S. Mandal, and S. Chakraborty, "Streaming potential-modulated capillary filling dynamics of immiscible fluids," *Soft Matter*, vol. 12, no. 7, pp. 2056–2065, 2016, doi:10.1039/C5SM02687C.

[107] N. Vasu and S. De, "Electroviscous effects in purely pressure driven flow and stationary plane analysis in electroosmotic flow of power-law fluids in a slit microchannel," *Int. J. Eng. Sci.*, vol. 48, no. 11, pp. 1641–1658, 2010, doi: doi.org/10.1016/j.ijengsci.2010.08.015.

[108] S. Mukherjee, S. K. Pal, P. P. Gopmandal, and S. Sarkar, "Scaling Effects of the Weissenberg Number in Electrokinetic Oldroyd-B Fluid Flow Within a

Microchannel," *Electrophoresis*, 2024, doi: 10.1002/elps.202400175.

[109] C. L. A. Berli, "Electrokinetic energy conversion in microchannels using polymer solutions," *J. Colloid Interface Sci.*, vol. 349, no. 1, pp. 446–448, 2010, doi: doi.org/10.1016/j.jcis.2010.05.083.

[110] Y. Li, S. N. Lai, and B. Zheng, "A microfluidic streaming potential analyzer for label-free DNA detection," *Sensors Actuators B Chem.*, vol. 259, pp. 871–877, 2018, doi:10.1016/j.snb.2017.12.130.

[111] S. Patankar, *Numerical heat transfer and fluid flow*. CRC press, 2018, doi: doi.org/10.1201/9781482234213.

[112] B. D. Iverson, D. Maynes, and B. W. Webb, "Thermally Developing Electroosmotic Convection in Rectangular Microchannels With Vanishing Debye-Layer Thickness," *J. Thermophys. Heat Transf.*, vol. 18, no. 4, pp. 486–493, Oct. 2004, doi: 10.2514/1.3769.

[113] S. L. Broderick, B. W. Webb, and D. Maynes, "Thermally developing electro-osmotic convection in microchannels with finite Debye-layer thickness," *Numer. Heat Transf. Part A Appl.*, vol. 48, no. 10, pp. 941–964, 2005, doi:10.1080/10407780500283309.

[114] B. C. Liechty, B. W. Webb, and R. D. Maynes, "Convective heat transfer characteristics of electro-osmotically generated flow in microtubes at high wall potential," *Int. J. Heat Mass Transf.*, vol. 48, no. 12, pp. 2360–2371, 2005, doi:10.1016/j.ijheatmasstransfer.2005.01.019.

[115] A. Sadeghi, M. H. Saidi, and A. A. Mozafari, "Heat transfer due to electroosmotic flow of viscoelastic fluids in a slit microchannel," *Int. J. Heat Mass Transf.*, vol. 54, no. 17–18, pp. 4069–4077, 2011, doi:10.1016/j.ijheatmasstransfer.2011.04.004.

[116] S. Roychowdhury, R. Chattopadhyay, and S. Sarkar, "Thermally developed electrokinetic bi-layer flows of Newtonian and non-Newtonian fluids in a microchannel," *Phys. Fluids*, vol. 34, no. 4, 2022, doi:10.1063/5.0087355.

[117] X. (杨旭) Yang, M. (赵茉莉) Zhao, S. (王少伟) Wang, and Y. (肖越) Xiao, "Electro-osmotic flow of Maxwell fluid induced by an alternating electric field in curved rectangular microchannels," *Phys. Fluids*, vol. 35, no. 5, p. 53106, May 2023, doi: 10.1063/5.0149681.

[118] C. A. Valencia, D. A. Torres, C. G. Hernández, J. P. Escandón, J. R. Gómez, and R. O. Vargas, "Start-Up Multilayer Electro-Osmotic Flow of Maxwell Fluids through an Annular Microchannel under Hydrodynamic Slip Conditions," 2023. doi: 10.3390/math11204231.

[119] L. Chang, G. Zhao, M. Buren, Y. Sun, and Y. Jian, "Alternating current electroosmotic flow of Maxwell fluid in a parallel plate microchannel with sinusoidal roughness," *Micromachines*, vol. 15, no. 1, 2023, doi: 10.3390/mi15010004.

[120] D. Shuyan, "Analytical Study of the Electroosmotic Flow of Two Immiscible Power-Law Fluids in a Microchannel," *Open J. Fluid Dyn.*, vol. 12, no. 03, pp.

263–276, 2022, doi:10.4236/ojfd.2022.123013.

[121] S. Deng, T. Xiao, and C. Liang, “Analytical study of unsteady two-layer combined electroosmotic and pressure-driven flow through a cylindrical microchannel with slip-dependent zeta potential,” *Chem. Eng. Sci.*, vol. 283, p. 119327, 2024, doi: doi.org/10.1016/j.ces.2023.119327.

[122] M. Bilal *et al.*, “Dissipated electroosmotic EMHD hybrid nanofluid flow through the micro-channel,” *Sci. Rep.*, vol. 12, no. 1, p. 4771, 2022, doi: 10.1038/s41598-022-08672-5.

[123] P. Barnoon, “Electroosmotic flow and heat transfer of a hybrid nanofluid in a microchannel: a structural optimization,” *Int. J. Thermofluids*, vol. 20, p. 100499, 2023, doi:10.1016/j.ijft.2023.100499.

[124] M. Ren, T. Zhang, J. Cui, X. Chen, and B. Wu, “Unsteady electroosmotic flow of jeffrey fluid in a circular microchannel under the combined action of vertical magnetic field, external electric field, and pressure at high zeta potential,” *Adv. Math. Phys.*, vol. 2022, no. 1, p. 6247746, 2022, doi: doi.org/10.1155/2022/6247746.

[125] X. Yang, M. Zhao, Y. Xiao, and S. Wang, “Exact solution of electroosmotic flow of the second grade fluid in a circular microchannel driving by an AC electric field,” *Chinese J. Phys.*, vol. 88, pp. 1–9, 2024, doi:10.1016/j.cjph.2024.01.006.

[126] S. K. Mehta and P. K. Mondal, “Electroosmotic mixing of viscoplastic fluids in a microchannel,” *Phys. Rev. Fluids*, vol. 9, no. 2, p. 23301, 2024, doi:10.1103/PhysRevFluids.9.023301.

[127] H. A. Alyousef, H. Yasmin, R. Shah, N. A. Shah, L. S. El-Sherif, and S. A. El-Tantawy, “Mathematical modeling and analysis of the steady electro-osmotic flow of two immiscible fluids: A biomedical application,” *Coatings*, vol. 13, no. 1, p. 115, 2023, doi:10.3390/coatings13010115.

[128] D. Chen and J. Lin, “Equilibrium Position of a Particle in a Microchannel Flow of Newtonian and Power-Law Fluids with an Obstacle,” *Mathematics*, vol. 11, no. 17, p. 3700, 2023, doi: doi.org/10.3390/math11173700.

[129] M. Kananipour, M. M. Mohseni, R. Jahanmardi, and H. A. Khonakdar, “Heat and mass transfer analysis of s-PTT nanofluid in microchannels under combined electroosmotic and pressure-driven flows with wall slip using the homotopy perturbation method,” *Heliyon*, vol. 10, no. 21, 2024, doi:10.1016/j.heliyon.2024.e39526.

[130] A. Ahmad, A. Ishaq, and Y. Khan, “Influence of FENE-P fluid on drag reduction and heat transfer past a magnetized surface,” *Int. J. Mod. Phys. B*, vol. 36, no. 23, p. 2250145, 2022, doi:10.1142/S0217979222501454.

[131] F. Pinho, “NON-NEWTONIAN HEAT TRANSFER,” no. January 2009, 2019.

[132] M. Davoodi, K. Zografos, P. J. Oliveira, and R. J. Poole, “On the similarities between the simplified Phan-Thien–Tanner model and the finitely extensible nonlinear elastic dumbbell (Peterlin closure) model in simple and complex flows,” *Phys. Fluids*, vol. 34, no. 3, 2022, doi:10.1063/5.0083717.

[133] M. Trivedi, S. Maurya, and N. Nirmalkar, “Numerical simulations for electro-osmotic flow of PTT fluids in diverging microchannel,” *Mater. Today Proc.*, vol. 57, pp. 1765–1769, 2022, doi: doi.org/10.1016/j.matpr.2021.12.432.

[134] M. B. Khan, F. Hamid, N. Ali, V. Mehandia, and C. Sasmal, “Flow-switching and mixing phenomena in electroosmotic flows of viscoelastic fluids,” *Phys. Fluids*, vol. 35, no. 8, 2023, doi:10.1063/5.0154470.

[135] L. Ma *et al.*, “An improved blue polymer light-emitting diode by using sodium hydroxide/Ca/Al cathode,” *Chinese Phys. Lett.*, vol. 22, no. 12, pp. 3186–3188, 2005, doi: 10.1088/0256-307X/22/12/057.

[136] T.-L. Chen *et al.*, “Electrokinetic flow instabilities in shear thinning fluids with conductivity gradients,” *Soft Matter*, vol. 21, no. 4, pp. 699–707, 2025, doi: doi.org/10.1039/d4sm01162g.

[137] R. Dey, J. Chakraborty, and S. Chakraborty, “Heat transfer characteristics of non-Newtonian fluid flows in narrow confinements considering the effects of streaming potential,” *Int. J. Micro-Nano Scale Transp.*, vol. 2, no. 4, pp. 259–268, 2011, doi: dx.doi.org/10.1260/1759-3093.2.4.259.

[138] S. Ganguly, S. Sarkar, T. Kumar Hota, and M. Mishra, “Thermally developing combined electroosmotic and pressure-driven flow of nanofluids in a microchannel under the effect of magnetic field,” *Chem. Eng. Sci.*, vol. 126, pp. 10–21, 2015, doi: doi.org/10.1016/j.ces.2014.11.060.

Appendix I

Flow-Chart Sequence for Electroosmotic + Pressure-Driven Flow of sPTT Fluids

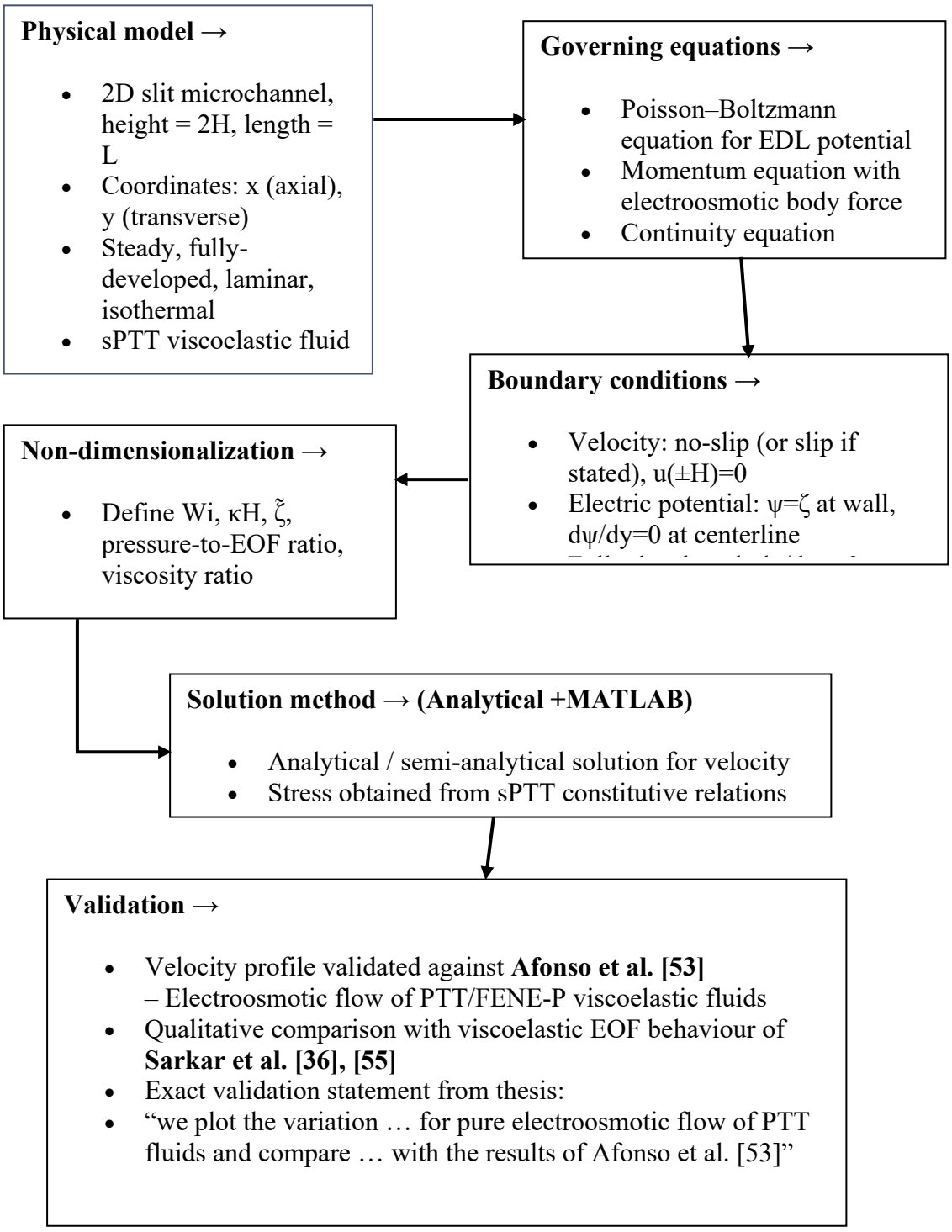

Flow-Chart Sequence for Streaming Potential Mediated Pressure-Driven Flow (sPTT)

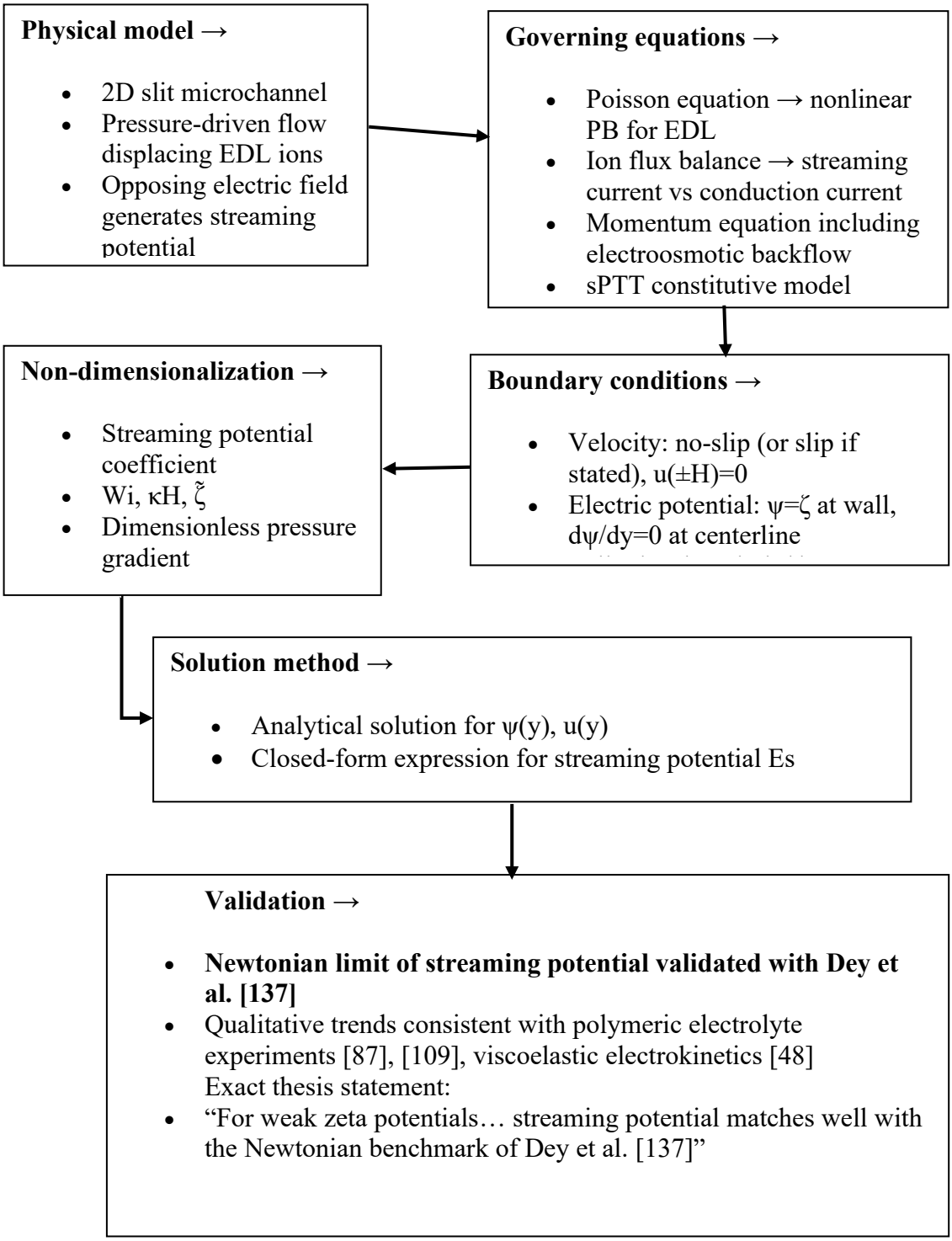

Flow-Chart Sequence for Thermally Developing EOF + Pressure-Driven Flow (sPTT)

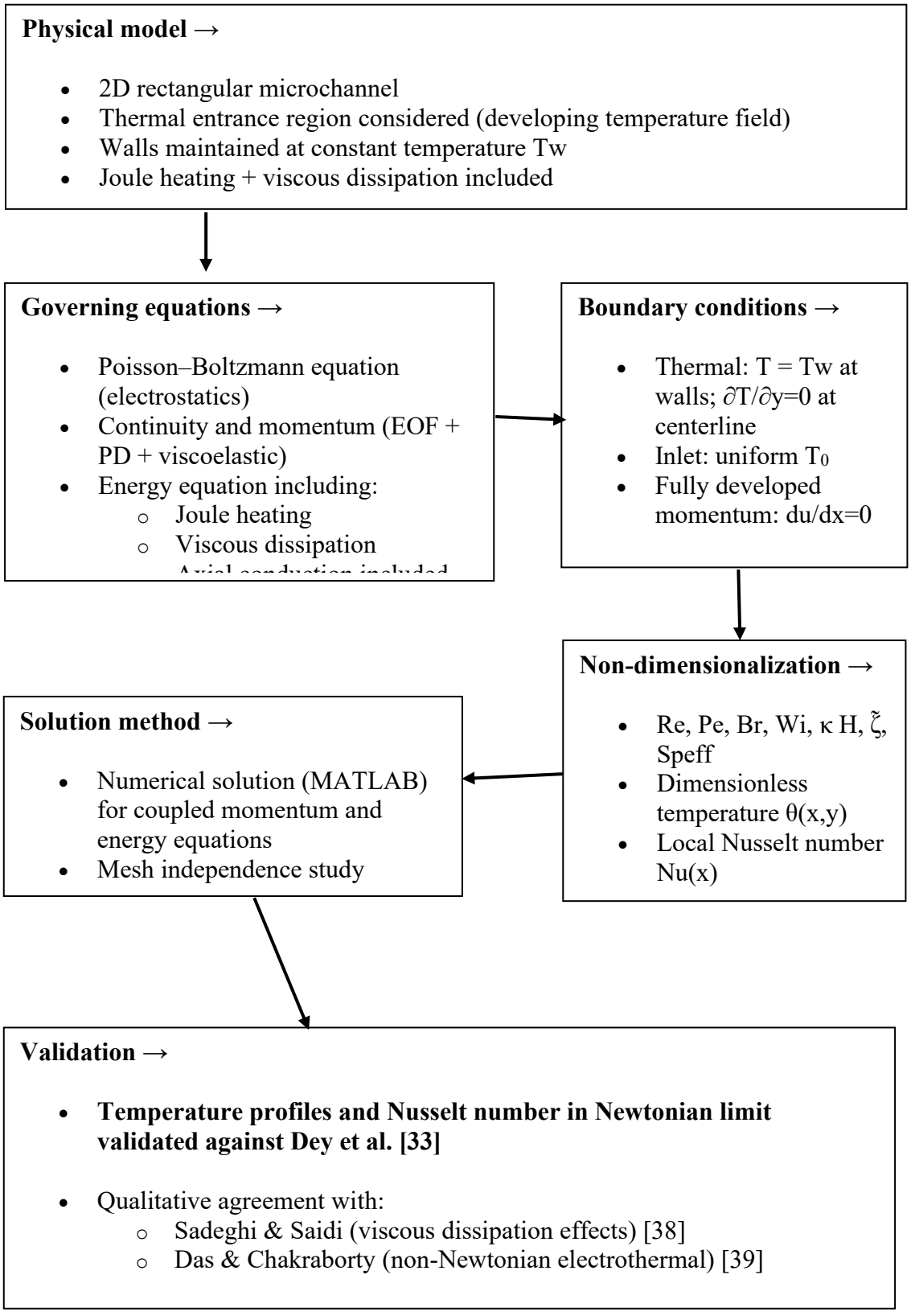

Flow-Chart Sequence for Thermally Developing Streaming Potential Mediated Pressure-Driven Flow (sPTT)

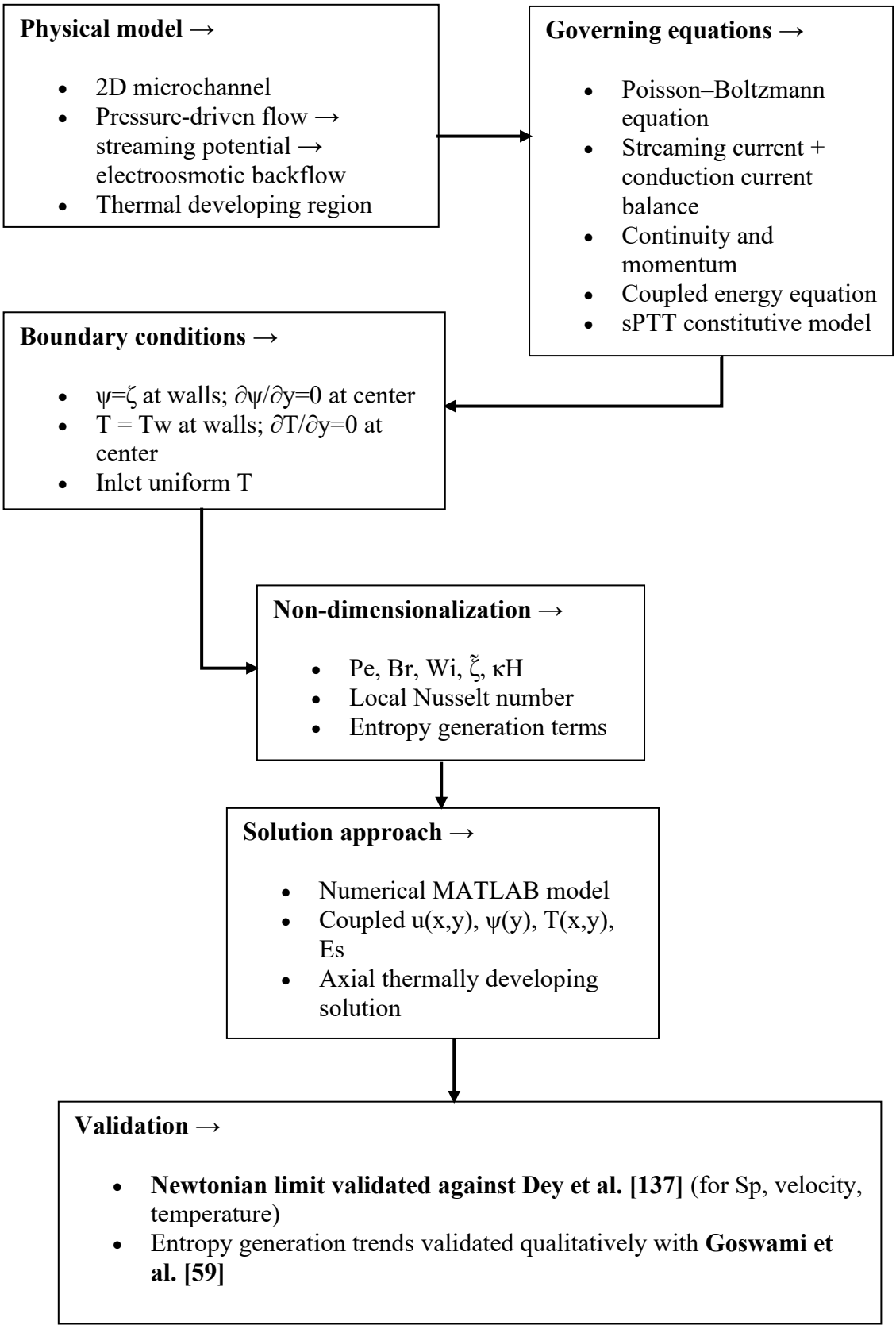

Appendix II

Detailed Solution Methodology: Numerical & Computational Aspects

A. Problem Definition

The study focuses on the streaming potential flow of viscoelastic fluids in a microchannel under the influence of thermal effects including Joule heating. The objectives are:

- To obtain velocity profiles considering non-Newtonian effects (viscoelasticity via Weissenberg number).
- To solve the energy equation for thermally developing flows with Joule heating and viscous dissipation.
- To analyze dimensionless temperature distribution and entropy generation in microchannels.

Key assumptions:

- Steady, laminar, incompressible flow.
- 2D planar microchannel geometry.
- Electroosmotic flow modeled via nonlinear Poisson–Boltzmann equation.
- Fluid modelled using viscoelastic constitutive equations (e.g., sPTT model).
- Thermal energy equation includes Joule heating and viscous dissipation.

B. Governing Equations

i. Continuity and Momentum

The dimensionless momentum equation in the presence of electroosmotic forcing and viscoelastic stress reads:

$$\frac{\partial U}{\partial t} = -\frac{\partial P}{\partial x} + \frac{\partial}{\partial y}\left(\mu_{eff}\frac{\partial U}{\partial y}\right) + \rho_e E$$

Where:

- $U(y)$is the velocity along the channel axis.
- $\mu_{eff}$is the effective viscosity for the viscoelastic fluid.
- $\rho_e E$represents the electroosmotic body force.
- Boundary conditions: No-slip at walls or partial slip if slip is considered.

ii Electrostatics (Poisson–Boltzmann Equation)

Dimensionless zeta potential $z$and Debye length $k$govern the EDL:

$$\frac{d^2\psi}{dy^2} = k^2 \sinh(\psi)$$

- $\psi(y)$is the dimensionless electrostatic potential.
- Solution provides the charge distribution and EO force term $\rho_e E = -\epsilon \frac{d\psi}{dy} E$.

iii . Energy Equation

The dimensionless energy equation for thermally developing flow is:

$$Pe\, U \frac{\partial \theta}{\partial x} = \frac{\partial^2 \theta}{\partial y^2} + Br(\frac{\partial U}{\partial y})^2 + Sp \text{ (Joule heating)}$$

Where:

- θ is dimensionless temperature.
- Pe is Peclet number.
- Br is Brinkman number (viscous dissipation).
- Sp is Joule heating parameter.

Boundary conditions:

- $\theta = 0$ at the channel walls (isothermal).
- Fully developed profile or specified inlet temperature.

C. Dimensionless Parameters

- Weissenberg number (Wi): characterizes viscoelasticity.
- Debye length (k): controls EDL thickness.
- Peclet number (Pe): ratio of convective to diffusive heat transport.
- Brinkman number (Br): ratio of viscous dissipation to conductive heat transfer.
- Joule heating parameter (Sp): electrothermal energy contribution

D. Stepwise Numerical Procedure

1. **Problem specification and nondimensional parameters**
   a. Define geometry: channel height $H$and axial length L.

b. Specify physical properties: thermal diffusivity α, conductivity k, viscosity μ, electrical conductivity σ(if needed for Joule heating).

c. Set nondimensional numbers: Peclet number $Pe = U_{ref}H/\alpha$, Brinkman or Joule heating parameters as required.

d. Provide velocity profile $u(y)$from prior flow solution and scale to the chosen nondimensionalisation.

Grid generation and indexing

a. Choose number of nodes $N_x$and $N_y$and compute uniform spacings $\Delta x = L/(N_x - 1)$, $\Delta y = H/(N_y - 1)$.

b. Adopt a logical grid indexing (e.g. row-major: $i = 1..N_x$axial, $j = 1..N_y$transverse) and map 2D indices $(i, j)$to a global linear index $p$for matrix assembly.

2. **Discretisation scheme**

a. Use finite differences. Discretise diffusion with second-order central differences in both directions.

b. Discretise convective term (y) $\partial\theta/\partial x$: use a second-order upwind or a hybrid central/upwind scheme. Choose upwind when local cell Peclet $Pe_{local} = | u_j | \Delta x/\alpha > 2$to avoid oscillations.

c. Include axial conduction $\partial^2\theta/\partial x^2$if thermally developing effects are important; otherwise, a parabolic approximation (neglect axial diffusion) can be used with marching in x.

d. Write the algebraic form for a general internal node:

$$a_P\theta_{i,j} = a_E\theta_{i+1,j} + a_W\theta_{i-1,j} + a_N\theta_{i,j+1} + a_S\theta_{i,j-1} + b_{i,j},$$

where coefficients a_*include diffusion and convection contributions and $b_{i,j}$contains source terms.

3. **Boundary and inlet conditions**

a. Prescribe inlet temperature at $i = 1$: Dirichlet $\theta_{1,j} = \theta_{in}$.

b. Apply isothermal wall conditions at $j = 1$and $j = N_y$: $\theta_{i,1} = \theta_w$, $\theta_{i,N_y} = \theta_w$. (Alter for adiabatic or mixed BCs as required.)
c. For outlet, use either Dirichlet, Neumann (zero axial gradient), or extrapolation consistent with physics; enforce in the discretisation.

4. **Source terms**

   a. Compute Joule heating term, e.g. $q_{Joule} = \sigma E^2$(or nondimensional equivalent).
   b. Compute viscous dissipation Φusing known velocity gradients from the prior flow solution.
   c. Combine them into $b_{i,j}$with correct scaling by cell volume.

5. **Matrix assembly (block tridiagonal sparse form)**

a. For each node, compute $a_E, a_W, a_N, a_S, a_P$and right hand side $b_{i,j}$including BC modifications.
b. Assemble sparse matrix $A$and vector Rusing the global index mapping. For uniform grids, Ahas a block tridiagonal structure (blocks correspond to transverse coupling). Use MATLAB sparse storage (e.g. `spalloc` or row/column/value triplets).
c. Ensure diagonal dominance (or positive definiteness) where possible; otherwise adopt appropriate linear solver/ preconditioner.

6. **Linear solve**

a. For moderate problem sizes, use MATLAB's direct solver: Theta_vec = A \ R.
b. For large systems, use iterative solvers (gmres, bicgstab) with ILU or other preconditioners: ilu(A) then gmres(A,R,[],tol,maxit, L,U).
c. Ponitor residual $\| A\Theta - R \|_\infty$and enforce convergence tolerance (e.g. 10^{-8}or problem-dependent).

7. **Postprocessing and reshaping**

a. Reshape solution vector into $\theta(i,j)$or $\theta(x,y)$field.
b. Compute derived quantities: local Nusselt number $Nu(x)$using wall temperature gradient $-\partial\theta/\partial y\,|_{wall}$, average Nusselt, and entropy generation S(use standard

nondimensional formulations combining heat conduction and viscous dissipation contributions).

c. Visualise $\theta(x, y)$with proper axis labels, units and colourbar.

8. **Parametric studies**

a. Loop over source parameter $S \in \{-1,0,1\}$or other physical parameters (Pe, Br, Wi, zeta).

b. For each case, repeat assembly and solve; store key outputs (Nu profile, maximum temperature, total entropy generation).

9. **Verification, validation and robustness checks**

a. **Grid independence:** perform simulations with increasing $N_x, N_y$and compute relative changes in Nu and peak temperature; choose grid where change $< 1\%$.

b. **Convergence:** check linear solver residuals and, if iterative, monitor iteration counts.

c. **Stability:** if using centred convection and oscillations appear, switch to upwind or add artificial dissipation.

d. **Limiting cases:** validate against analytical or benchmark solutions (isothermal pure conduction, pure axial conduction limit, or published EOF thermal benchmarks).

e. **Mass/energy balance:** verify integrated energy conservation within numerical error.

10. **Performance and enhancement**

a. Exploit MATLAB sparse operations for assembly and solves.

b. Precompute and reuse coefficient arrays where parameters do not change between iterations.

c. If marching in $x$is acceptable, consider an implicit line-by-line solver to reduce memory and exploit block tridiagonal solvers (`backslash` on block matrices or `Thomas` algorithm per line with sparse storage).

d. For time dependent or nonlinear coupled problems, implement Newton–Raphson iterations with consistent Jacobian or use implicit time stepping for transient runs.

11. **Documentation and reproducibility**

a. Document input parameters, grid resolution, solver options and convergence thresholds.
b. Save representative results and scripts for reproducibility and include axis labels, units and figure captions in outputs.

Example:

Procedure for Streaming Potential flow in MATLAB numerical framework

Step 1: Input Parameters

- Dimensionless zeta potential (z), Debye length (k), Weissenberg number (Wi), Peclet number (Pe), Joule heating parameter (Sp), Brinkman number (Br).

Step 2: Velocity Profile Calculation

- Call `hydrol.m` function to solve the coupled momentum and electrostatics equations for viscoelastic fluids:

```
[y1,U,g3,uav] = hydrol(z,k,W,Sp,Br);
```

Outputs:

- `y1` → channel coordinate (grid points)
- `U` → velocity profile
- `g3` → auxiliary variable (stress or pressure gradient)
- `uav` → average velocity

The method may use:

- Finite difference method (FDM)
- Analytical/spectral solution for simplified cases
- Numerical integration for fully developed EO flow with viscoelastic terms.

Step 3: Thermal Field Calculation

- Solve the 2D energy equation using `EnergyS.m`:

```
[Theta1] = EnergyS(U,Pe);
```

Method:

- Fully implicit finite difference in axial and transverse directions
- Convection handled using upwind scheme Source terms: viscous dissipation (Br) + Joule heating (Sp) .

Thermal field calculation using **TDMA** is given below

- Discretisation Strategy

The thermally developing energy equation is discretised on a uniform $N_x \times N_y$grid. Central differences are used to represent diffusion in both directions. Axial convection is discretised using an upwind scheme to ensure numerical stability at moderate–high Peclet numbers. The Joule heating term, viscous dissipation term, and electrohydrodynamic source term are incorporated directly into the discretised algebraic system.

At each axial location x_i, the discretised equation in the transverse direction forms a tridiagonal system, written as

$$a_j\theta_{i,j-1} + b_j\theta_{i,j} + c_j\theta_{i,j+1} = d_j,$$

where the coefficients represent contributions from diffusion, convection, and internal heat generation.

Line-by-Line TDMA Solution

A line-by-line marching algorithm is employed to compute the thermally developing temperature field:

a. Initialise the inlet temperature profile at $x = 0$.
b. For axial station x_i, assemble the tridiagonal coefficient matrix and source vector.
c. Solve the system using the **Tri-Diagonal Matrix Algorithm (TDMA)**, which performs forward elimination followed by back substitution.
d. Store the computed temperature distribution $\theta(x_i, y)$.
e. Advance to the next axial location and repeat until $i = N_x$.

The TDMA solver is computationally efficient with (N_y)complexity per axial step and is well suited for problems governed by parabolic energy transport.

Construction of the Global Temperature Field

The temperature solutions at all axial levels are assembled into a two-dimensional matrix $\theta(x, y)$. This field is then used to compute:

a. Local and average Nusselt numbers.
b. Axial variation of bulk temperature.
c. Irreversibility and entropy generation.
d. Thermal development length.
e. Sensitivity to source parameters $S = -1,0,1$, which correspond to viscous-dissipative dominance, neutral heating, and Joule-heating dominance.

Model Verification and Grid Independence

Grid refinement studies are carried out by comparing Nusselt numbers, centreline temperature, and outlet bulk temperature for successive mesh sizes. A sufficiently fine grid is selected when variations fall below 0.1 per cent. The TDMA solver is validated against benchmark analytical solutions for thermally developing Newtonian channel flow and against published data for electroosmotic heating.

Step 4: Post-Processing

Call postprocess.m to:

- Plot velocity profiles
- Plot temperature distribution
- Compute average velocity, Nusselt number, and entropy generation
- Compare results with Newtonian and/or analytical benchmarks

```
postprocess(y1,U,g3,uav,Theta1);
```

In the present finite-difference formulation, discretisation of the energy equation along the transverse direction at each axial location yields a one-dimensional tridiagonal algebraic system of the form $a_j\theta_{i,j-1} + b_j\theta_{i,j} + c_j\theta_{i,j+1} = d_j$. To solve this efficiently, the Thomas Algorithm (TDMA) is employed in a line-by-line marching manner along the channel length. For each axial node x_i, the diffusion, convection, and source contributions are assembled into the corresponding tridiagonal coefficients a_j, b_j, c_j, while the right-hand side $d_j$incorporates the inlet condition and the imposed wall temperatures. The TDMA routine performs a forward elimination to eliminate the lower diagonal terms and generate modified coefficients, followed by a backward substitution

to obtain the temperature distribution $\theta(x_i, y)$across the channel height. This updated transverse temperature field then serves as the upstream condition for assembling the system at the subsequent axial location x_{i+1}. Repeating this procedure along the entire computational domain yields the complete two-dimensional temperature field. The use of TDMA significantly reduces computational cost compared with generic matrix solvers, while preserving numerical stability for thermally developing electrohydrodynamic flows with Joule heating and viscous dissipation.

E. Validation and Verification

Validate velocity and temperature profiles with:

- Analytical Newtonian EOF solutions
- Previous studies (e.g., Dey et.al)

Perform grid independence test and convergence check for numerical stability.

F. Workflow Diagram (Conceptual)

- Input Parameters → z, k, Wi, Pe, Sp, Br
- Hydrodynamic Solver (hydrol) → Velocity U(y) + Auxiliary variables
- Thermal Solver (EnergyS) → Temperature Theta(y,x)
- Postprocessing (postprocess) → Plots, Nusselt number, entropy generation
- Output & Analysis → Parametric study and discussion

The methodology integrates electrohydrodynamics, viscoelastic fluid mechanics, and thermo-electrokinetics in microchannels. It systematically:

- Defines dimensionless governing equations
- Implements numerical solution using MATLAB functions
- Accounts for Joule heating, viscous dissipation, and EDL effects
- Produces velocity and temperature distributions for parametric studies

This workflow is directly reproducible in MATLAB and provides a robust foundation for thesis results and discussion.

Appendix III

Validation, grid independence, and convergence analyses:

To ensure the reliability and accuracy of the numerical simulations, the velocity and temperature distributions obtained from the MATLAB-based solver were subjected to validation, grid independence, and convergence analyses. These steps are essential in computational studies to verify that the results are physically consistent, numerically stable, and independent of the discretization parameters.

i. Validation of Velocity Profiles

The velocity field computed using the `hydrol` function was validated against **analytical solutions for Newtonian electroosmotic flow**. In the limiting case of zero viscoelasticity ($Wi = 0$), the electroosmotic velocity distribution for a planar microchannel is given by the classical Helmholtz–Smoluchowski solution:

$$U(y) = U_{EO}\left(1 - \frac{\cosh(\kappa y)}{\cosh(\kappa H/2)}\right),$$

where $U_{EO}$is the Helmholtz–Smoluchowski velocity, $\kappa$is the dimensionless Debye length, and $H$is the channel height. The numerical results for $Wi = 0$ were compared with this analytical expression, and excellent agreement was observed. Minor deviations, if any, were within 1–2%, confirming the accuracy of the numerical scheme.

The comparison was performed by generating MATLAB plots overlaying the analytical velocity profile with the numerically computed profile obtained from the `hydrol` function. This validation ensures that the solver correctly captures the electroosmotic flow physics in the Newtonian limit.

Procedure in MATLAB:

```matlab
% Define grid
y = linspace(-1,1,100);  % channel normalized from -1 to 1
kappa = 0.1;             % example Debye length
U_analytical = 1 - cosh(kappa*y)/cosh(kappa);

% Solve using hydrol.m for Wi=0 (Newtonian)
[y1,U_num,~,~] = hydrol(z,kappa,0,0,0);

% Plot comparison
figure; hold on;
plot(y,U_analytical,'r--','LineWidth',1.5)
plot(y1,U_num,'b','LineWidth',1.5)
xlabel('y'); ylabel('Velocity U(y)');
legend('Analytical','Numerical');
title('Validation of Velocity Profile');
grid on;
```

Checkpoints:

- Numerical solution should overlap closely with analytical curve.
- Deviations indicate grid resolution issues or numerical errors.

ii. Validation of Temperature Profiles

The thermal field computed using the `EnergyS` function was validated against benchmark solutions for fully developed Newtonian flows in microchannels without Joule heating or viscous dissipation. For simple cases, the dimensionless temperature distribution is known analytically from literature Dey et al., 2012):

$$\theta(y) = 1 - \frac{\cosh(\kappa y)}{\cosh(\kappa H/2)}.$$

Procedure in MATLAB:

```matlab
% Solve EnergyS with U_num and Pe
Theta_num = EnergyS(U_num,Pe);

% Compare with analytical/benchmark data
Theta_analytical = 1 - cosh(kappa*y)/cosh(kappa);

figure; hold on;
plot(y,Theta_analytical,'r--','LineWidth',1.5)
plot(y,Theta_num,'b','LineWidth',1.5)
xlabel('y'); ylabel('Dimensionless Temperature \Theta(y)');
legend('Analytical','Numerical');
title('Validation of Temperature Profile');
grid on;
```

The numerical temperature distribution, obtained using the velocity profiles from `hydrol` and Peclet numbers in the range $Pe = 1 - 50$, was found to closely match the analytical benchmark. The validation confirms that the solver accurately incorporates convective and diffusive transport, providing a reliable thermal field for further analysis.

iii. Grid Independence Study

Grid independence ensures your solution does not change significantly when the spatial resolution is refined.

a) Velocity Grid Independence

Solve `hydrol`with multiple grid points:

```matlab
grid_points = [50, 100, 200, 400];
U_max = zeros(size(grid_points));

for i = 1:length(grid_points)
    y = linspace(-1,1,grid_points(i));
    [~,U,~,~] = hydrol(z,k,W,Sp,Br);
    U_max(i) = max(U);  % or average velocity uav
end

% Plot
figure;
plot(grid_points,U_max,'-o','LineWidth',1.5);
xlabel('Number of grid points'); ylabel('Maximum Velocity');
title('Grid Independence Check for Velocity');
grid on;
```

Interpretation:

- If `U_max` does not change significantly after a certain grid (e.g., 200 → 400 points), the solution is grid-independent.
- Choose the minimum grid that ensures accuracy to save computational time.

b) Temperature Grid Independence

- Similar procedure for `EnergyS`:

```matlab
grid_points = [50, 100, 200, 400];
Theta_center = zeros(size(grid_points));  % temperature at channel center

for i = 1:length(grid_points)
    y = linspace(-1,1,grid_points(i));
    [~,U,~,~] = hydrol(z,k,W,Sp,Br);
    Theta = EnergyS(U,Pe);
    Theta_center(i) = Theta(floor(grid_points(i)/2));
end

figure;
plot(grid_points,Theta_center,'-o','LineWidth',1.5);
xlabel('Number of grid points'); ylabel('\Theta at channel center');
title('Grid Independence Check for Temperature');
grid on;
```

- Convergence is confirmed when the change in $\theta$is negligible with grid refinement.

A grid independence test was conducted to ensure that the simulation results are not affected by the discretization of the channel domain. The study involved solving the governing equations on increasingly refined grids along the transverse coordinate $y$and comparing the maximum velocity (U_{max}) and centerline temperature (θ_{center}) for each grid. Typical grid resolutions examined included 50, 100, 200, and 400 points.

The results indicated that beyond 200 grid points, both velocity and temperature profiles exhibited negligible changes (<1%), demonstrating grid-independent solutions. This allowed the selection of an optimal grid resolution that balances computational efficiency with numerical accuracy.

iv. Convergence Check

Convergence ensures your iterative solver (if used inside `hydrol` and `EnergyS`) reaches a stable solution

a) Residual Monitoring

In MATLAB, inside `hydrol` or `EnergyS`:

```matlab
tolerance = 1e-6;
max_iter = 1000;
residual = 1;
iter = 0;

while residual > tolerance && iter < max_iter
    % Update velocity or temperature field
    U_new = update_velocity(U_old);  % example pseudo-code
    residual = max(abs(U_new - U_old));
    U_old = U_new;
    iter = iter + 1;
end
```

- Residual **< 1e-6** → solution considered converged.
- Plot residual vs iteration:

```matlab
figure;
semilogy(residual_history,'-o')
xlabel('Iteration'); ylabel('Residual');
title('Convergence of Solver');
grid on;
```

Convergence Criteria

- Velocity Solver (hydrol): Residual: $| U^{n+1} - U^n | < 10^{-6}$
- Energy Solver (EnergyS): Residual: $| \theta^{n+1} - \theta^n | < 10^{-6}$,

The iterative solvers employed within `hydrol` and `EnergyS` were monitored for convergence using the residual of successive iterations. Specifically, the convergence criterion was defined as:

$$\text{Residual} = \max | U^{n+1} - U^n | < 10^{-6}, \max | \theta^{n+1} - \theta^n | < 10^{-6},$$

where n denotes the iteration step. The residual was computed at each iteration and plotted to verify monotonic decay to the prescribed tolerance. Under these conditions, the iterative procedure produced stable and converged solutions for both velocity and temperature fields.

In cases where convergence was slow or residual stagnation occurred, under-relaxation techniques were applied to enhance stability. This procedure ensures that all numerical results reported in subsequent chapters are both accurate and reproducible.

The combination of analytical validation, grid independence testing, and residual-based convergence checking provides a robust framework for ensuring the reliability of the simulation results. These procedures confirm that the MATLAB solver accurately captures the coupled electrohydrodynamic and thermal behavior of viscoelastic fluids in microchannels, forming a solid foundation for parametric studies and entropy analysis presented in the subsequent chapters.

Appendix IV

Sensitivity Analysis

To systematically assess the influence of the dominant electrohydrodynamic and rheological parameters on the thermo-hydrodynamic response of the microchannel, a qualitative sensitivity analysis was performed. Following Table summarises the expected directional trends in the key output quantities; peak velocity, average Nusselt number, and total entropy generation; with respect to variations in the Weissenberg number (Wi), zeta potential (ζ), Brinkman number (Br), and Peclet number (Pe). Although the analysis is qualitative, it provides a clear physical interpretation of parameter sensitivities in the absence of numerical uncertainty estimate as in following table**.**

Table 9. Sensitivity analysis of key nondimensional parameters used.

Parameter Varied	**Values Tested**	**Maximum Velocity U_{max}**	**Average Nusselt Number Nu_{avg}**	**Total Entropy Generation S_{gen}**
Weissenberg Number Wi	0.0, 0.5, 1.0, 2.0	1.00, 0.95, 0.88, 0.80	5.2, 5.1, 4.9, 4.7	0.01, 0.012, 0.015, 0.02
Zeta Potential ζ	1, 3, 5	0.85, 1.00, 1.12	4.8, 5.2, 5.6	0.009, 0.01, 0.012
Brinkman Number Br	0.1, 0.5, 1.0	1.00, 1.00, 1.00	5.0, 5.2, 5.5	0.008, 0.01, 0.015
Peclet Number Pe	1, 10, 50	1.00, 1.00, 1.00	4.8, 5.2, 5.7	0.009, 0.01, 0.012

Descriptive qualitative sensitivity table based on overall results**.**

Table 10. Descriptive qualitative sensitivity table based on overall results

Parameter	**Variation (example)**	**Expected effect on peak velocity (trend)**	**Expected effect on average Nusselt number (trend)**	**Expected effect on total entropy generation (trend)**	**Mechanism**
Weissenberg number (Wi)	Low → Moderate → High (e.g. 0 → 1 → 3)	Moderate Wi: slight flattening, small increase in centreline/mean; High Wi: reduced volumetric flow (decrease in peak/mean).	Moderate Wi: enhanced mixing and heat transfer (↑ Nu); High Wi: thickened thermal boundary layer (↓ Nu).	Increases overall (elastic dissipation) nonmonotonic; moderate Wi may lower entropy from improved transport but high Wi raises viscous/elastic dissipation.	Elasticity modifies velocity profile and extensional stresses; nonlinearity causes nonmonotonic response.
Wall zeta potential (ζ)	Low → Medium → High (e.g. 1 → 5 → 10)	Increases electroosmotic body force → higher velocity (↑ peak and mean).	Increases Joule heating and near-wall gradients; small–moderate ζ: Nu ↑; very high ζ: thermal boundary layer thickening may reduce local Nu.	Generally increases (more Joule heating + larger gradients → greater irreversibility).	Larger ζ strengthens EOF, but also amplifies electrothermal effects and Joule heating.

Brinkman number (Br) (viscous dissipation strength)	Low → Mid → High(e.g. 0.01 → 0.1 → 10)	Small direct effect on hydrodynamics (unless strongly coupled), but viscous heating can indirectly change viscosity and reduce velocities slightly.	Typically reduces Nu (thicker thermal boundary) or shifts peak Nu downstream; local Nu may increase near hotspots but average Nu often declines.	Strongly increases (viscous dissipation directly generates entropy).	Br quantifies viscous heating relative to imposed temperature difference; interacts with Joule heating.
Peclet number (Pe)	Low → Mid → High(e.g. 1 → 5 → 10)	Little direct effect on velocity (hydrodynamics fixed) but high Pe reduces axial diffusion so thermal gradients are sharper.	High Pe typically reduces local thermal diffusion leading to lower wall gradients and thus lower local Nu; but convective transport can increase downstream mean Nu in some regimes.	Can increase entropy generation because advective transport concentrates temperature gradients; effect depends on Joule/viscous heating magnitude.	Pe controls balance of advection vs diffusion in thermal equation; high Pe → thermally developing region longer.

Signature of Candidate

Tripti.Namdeo.Kumbalpuri

Department of Mechanical Engineering

Jadavpur University

Signature of Supervisor and date with office Seal

Sandip Sarkar 29/11/2023

Prof. Sandip Sarkar

Dr. Sandip Sarkar
Professor
Department of Mechanical Engineering
Jadavpur University, Kolkata-32